Universidad de Concepción
Facultad de Ciencias Físicas y Matemáticas

Two-Photon Interference with a 4×4 Multicore Optical Fiber Beam Splitter

Interferencia de Dos Fotones con un Divisor de Haz 4×4 de Fibra Óptica Multinúcleo

Tesis para optar al grado de
Magíster en Ciencias con Mención en Física
por

Mariana Navarro Asan-Srain

Marzo 2023
Concepción, Chile

Director de Tesis: **Dr. Stephen Patrick Walborn**

Agradecimientos

En primer lugar quiero agradecer a mi profesor guía de tesis Stephen Walborn quien siempre me brindó apoyo en las decisiones que tomé durante el magíster, por su comprensión y por siempre estar ahí para mí. También quiero agradecer a los profesores Aldo Delgado, Esteban Sepúlveda y Pablo Solano, quienes mostraron su apoyo y preocupación.

Quiero agradecer a mis preciados amigos y amigas quienes me han acompañado a lo largo de estos años. A Camila Leal, Bárbara Meza y Grace Rivas, quienes siempre mostraban ánimos de entender lo que hago cada vez que nos veíamos. A Guillermo Zieballe, Ayleen Contreras, Aníbal Neira, Pablo Navarrete, Félix Palma y Scarlett Rebolledo, quienes fueron un pilar fundamental para sobrevivir estos seis años de universidad. A Jorge Gidi por la confianza depositada en mi persona. Al maestro Álvaro Alarcón por sus valiosos consejos.

Agradezco a mis compañeros y amigos del laboratorio Italo Machuca, Santiago Gómez y Daniel Martínez por las buenas risas y discusiones de física.

Agradezco a mi padres y toda mi familia por su apoyo. Agradezco en especial a mi abuelita Silvia Díaz por su amor y preocupación.

Agradezco a mi persona favorita Leonardo Zambrano, que desde el primer momento creyó en mis capacidades y quien me motivó a atraverme en cada paso de los últimos años. Sin duda, nada sería lo mismo sin ti.

Finalmente, agradezo a la Agencia Nacional de Investigación y Desarrollo (ANID) y al Millennium Institute for Research in Optics (MIRO) por el financiamiento.

Resumen

La motivación de esta tesis está impulsada por el reciente desarrollo de divisores de haces de fibra óptica de cuatro núcleos de alta calidad, lo cuales alcanzan una relación de división casi perfecta del 25% entre los cuatro núcleos que se encuentran en el mismo material de revestimiento. Una aplicación importante de estos divisores de haces ópticos en el contexto de información cuántica, es la realización de interferencia de dos fotones, ya que es un fenómeno fundamental para el procesamiento de información de tecnologías cuánticas fotónicas. Aun más, constituye la base para realizar medidas de estados máximamente entrelazados y puede utilizarse para producir correlaciones cuánticas. Como primera investigación, usando estados coherentes débiles de entrada para estudiar la interferencia de cuarto orden en un divisor de haz de fibra óptica de cuatro núcleos, mostramos experimentalmente que las correlaciones cuánticas, en forma de discordia geométrica, pueden ser controladas y máximizadas al manipular la intensidad de los estados de entrada. Como segunda investigación, diseñamos y estudiamos teóricamente un analizador de estados de Bell fotónico para estados de dimensión cuatro. Con interferencia de dos fotones en un par de divisores de haces de cuatro núcleos, logramos discriminar de manera óptima los 4×4 estados de Bell, lo que da lugar a siete salidas. Luego, mostramos que con un par de fotones ancilla entrelazados podemos identificar probabilíticamente (pero inequívocamente) un sólo estado de Bell. Esta tesis debería contribuir al uso de correlaciones cuánticas y la implementación de mediciones de Bell en protocolos de comunicación cuántica en las redes de telecomunicaciones futuras, en particular, aquellas que aprovechan las fibras estructuradas espacialmente.

Abstract

The motivation of this thesis is driven by the recent development of high-quality four-core optical fiber beamsplitters, which achieve a near-perfect 25% split ratio between the four cores placed within the same cladding material. An important application of these optical beamsplitters in the context of quantum information is the realization of two-photon interference, as it is a fundamental phenomenon for information processing of photonic quantum technologies. Moreover, it forms the basis for performing measurements of maximally entangled states and can be used to produce quantum correlations. As a first investigation, using weak coherent input states to study fourth-order interference in a four-core optical fiber beam splitter, we show experimentally that quantum correlations, in the form of geometric discord, can be controlled and maximized by manipulating the intensity of the input states. As a second investigation, we design and theoretically studied a photonic Bell state analyzer for four-dimensional states. With two-photon interference in a pair of four-core beam splitters, we achieve optimal discrimination of the 4×4 Bell states, resulting in seven outcomes. Then, we show that with a pair of entangled ancilla photons, we can probabilistically (yet unequivocally) identify a single Bell state. This thesis should contribute to the exploitation of quantum correlations and the implementation of Bell measurements in quantum communication protocols in future telecommunication networks, in particular, those that take advantage of spatially structured fibers.

Contents

List of Tables

List of Figures

Chapter 1

Introduction

Quantum information science promises to revolutionize how information is transmitted, processed, and stored, giving way to paradigms such as quantum teleportation [1], quantum cryptography [2], quantum computing [3, 4] and many others [5, 6, 7]. Different physical systems have been investigated to implement these quantum protocols [8]. However, photons stand out as an effective carrier for processing and encoding information since they are transportable, propagate rapidly, are easy to manipulate, and do not interact with the environment [9]. Another key element in this revolution is the transport of quantum states from one place to another. In this regard, to be viable, quantum communication will most likely need to employ the same technological infrastructure as classical telecommunications.

A main goal in telecommunications is to increase the transmission capacity of optical channels. Currently, data rates are nearing the physical limits that are possible in single-mode optical fibers [10, 11]. This problem has led to several interesting encoding schemes and technologies [12], one of them are multicore optical fibers, which promise to be a solution to the capacity problem. This type of fiber is composed of multiple cores embedded in the same cladding [12]. Each core is propagated a single mode of light, and it has been shown that the relative phase fluctuations between quantum states propagating in different cores are much more stable and less than for multiple single-mode fibers [13, 14, 15].

Multicore fibers are expected to have an even more significant impact on quantum information protocols [16] since they allow us to exploit higher dimensions. A d-level quantum system offers a higher information capacity and noise resilience in quantum communications [17], a larger violation of Bell inequalities [18] and more efficient quantum simulation [19] and computation [20]. In addition, high-dimensional entangled states enhance robustness against eavesdropping, and quantum cloning [21, 22]. Many experiments with multicore technology have been realized in this direction [23, 24, 25, 26, 27, 28].

However, a complete toolbox for the manipulation of photonic quantum information encoded in multicore fibers is still lacking. One crucial element, a fiber-embedded multicore beam splitter, has only been recently developed. These are multi-port interference devices that coherently combine light from input fiber cores and can be used to decrease the optical depth of linear circuits [28, 29], as well as to build multi-path interferometers with applications in optical metrology [30, 31], for example. Multicore beam splitters have been employed in a few

single-photon experiments [23, 25, 28].

An important application of optical beam splitters in the context of quantum information is the realization of two-photon interference [32]. It can be used to produce quantum correlations when the quantum state is post-selected in the number basis [33, 34], and it is essential to perform measurements of the maximally entangled states, the so-called Bell states [35, 36, 37]. The present thesis mainly focuses on these two topics to study two-photon interference at a four-core fiber beam splitter.

We begin in chapter 2 by introducing fundamental concepts that we will use in the following chapters to help us put our work into context. Then, in chapter 3, we motivate and introduce multicore fiber technology using photons encoded in the path degree of freedom. The following two chapters are concentrated the principal contribution of this thesis.

In chapter 4, we show how post-selected quantum correlations can be controlled and maximized by adjusting the intensity ratio of two independent weak coherent input pulses at telecom wavelengths. When considering the complete Poissonian photon statistics, the input and output states are each a tensor product of coherent states and thus present no correlations. However, in Ref. [38], it was shown that using post-selection in the photon number, the output state produced by the equal intensity of the input pulse could in fact, demonstrate non-classical correlation in the form of quantum discord [39]. Though discord does not always imply entanglement [39], recent studies have shown that it plays an important role in quantum tasks such as quantum computing [40], remote state preparation [41], quantum cryptography [42], quantum illumination and quantum metrology [43, 44].

In chapter 5, we design a photonic Bell state analyzer for four-dimensional states using only linear optical components, e.g., phase shifters, beam splitters, mirrors, etc. Ideally, this device allows us to discriminate all the d^2 Bell states, where d is the dimension of the states. Nevertheless, in Ref. [45], it has been shown that when $d = 4$, the optimal measurement separates the 16 Bell states into seven groups. In order to build an optimal fiber-based bell state analyzer, we translate to fiber devices the setup shown in Ref. [45], where they use hyperentangled photons in polarization and path propagating in free space to discriminate the 16 Bell states. To improve our high-dimensional Bell state measurement, we increase the dimension of the system by introducing ancillary photons. We show we can probabilistically and unequivocally identify two Bell states.

Finally, in chapter 6, we present the main results obtained in chapter 4 and 5, concluding the work done with possible extensions for the future.

Chapter 2

Quantum Mechanics

The motivation of this chapter is to review some basic topics in quantum mechanics and quantum information that will be necessary for a better understanding of this thesis. All this without pretending to show the complete deduction of certain fundamental aspects exhaustively. As a note, much of the content is based on the seminal book by Nielsen and Chuang [6].

We begin by describing mathematically the quantum properties of a physical system in section 2.1, where we also introduce the density matrix and extend the concept of state to dimension d. In section 2.2, we briefly see how quantum states evolve. Then, in section 2.3, we give the necessary formalism to describe a composite quantum system made up of two or more subsystems, where we also present the famous Bell-States. We continue in section 2.4 with the effects of measurements on quantum systems and show the importance of Bell state measurements. Next, as a measure of closeness between quantum states, we present the fidelity in section 2.5. Finally, in section 2.6, we introduce two measures of quantum correlations.

2.1 Quantum states

Every isolated physical system is described by a Hilbert space $\mathcal{H}$ with inner product, which has an associated unitary complex vector $|\psi\rangle$ called *quantum state*. This vector describes the system in its entirety. For $|\psi\rangle$ to be a unit vector, it must obey the *normalization condition* $|\langle\psi\,|\psi\rangle\,| = 1$.

An isolated system is also called a closed system since it does not interchange information with any other system. Another important fact about quantum states is that two states that only differ by a global phase are completely equivalent since measurements on them give the same outcome.

For quantum states that are not fully known, also known as open systems, it is convenient to use an alternative formulation: the *density operator* or *density matrix*. Suppose we have an observer that wants to make a measurement on $|\psi_i\rangle$ but does not know in which of all the states in a set $\{|\psi_i\rangle\}$ the system is prepared. The observer only has access to the probabilities $\{p_i\}$ of

each of the states. Then the observer can only write the density operator of the system, defined by the equation

$$\rho = \sum_i p_i |\psi_i\rangle\langle\psi_i|. \tag{2.1}$$

Density operators are physically meaningful if and only if it satisfies the following properties:

a) (Normalization) The trace of ρ is equal to one.

b) (Positivity) ρ is a positive semi-definite operator, i.e., their eigenvalues are greater or equal to zero.

If there exists a vector $|\psi\rangle$ such that the density matrix can be written as $|\psi\rangle\langle\psi|$, then we say that the state is *pure*. Otherwise, we say that the state is *mixed*. A state ρ can be determined as pure or mixed by calculating its *purity* $\mathsf{tr}(\rho^2) \leq 1$, where the equality holds if and only if the state is pure.

2.1.1 Qudits

Quantum states that belong to d-dimensional Hilbert space $\mathcal{H} = \mathbb{C}^d$ are called *qudit* states, in analogy with the name *qubit* for two-dimensional quantum systems. A qudit is an arbitrary superposition of some set of orthonormal basis states $\{|\psi_i\rangle\}_{i\in\{0,\ldots,d-1\}}$, such as

$$|\Psi\rangle \equiv \sum_{i=0}^{d-1} p_i \, |\psi_i\rangle \, , \tag{2.2}$$

where the complex numbers p_i obey the normalization condition $\sum_i |p_i|^2 = 1$. By increasing the dimension of the state, we can expand the amount of information (number of bits) encoded in the quantum system, being able to encode up to $\log_2(d)$ bits per qudit.

Of our special interest in this thesis will be qudits that live in a 4-dimensional Hilbert space, which we will write as

$$|\upsilon\rangle = \alpha \, |0\rangle + \beta \, |1\rangle + \gamma \, |2\rangle + \delta \, |3\rangle \, . \tag{2.3}$$

These states are often called *ququarts*.

2.2 Evolution

The time evolution of a closed quantum system is described by a unitary transformation. That is, the state $|\psi\rangle$ at time t_1 is related to the state $|\psi'\rangle$ at time t_2 by a unitary matrix[1] U, such as

$$|\psi'\rangle = U \, |\psi\rangle \, . \tag{2.4}$$

[1] A complex square matrix U is unitary if $U^\dagger U = UU^\dagger = 1$

In the case of density operators, their evolution is given by

$$\rho = U\rho U^{\dagger}. \tag{2.5}$$

2.3 Composite Systems

The Hilbert space $\mathcal{H}$ of a d-dimensional composite physical system is the tensor product of the Hilbert space $\mathcal{H}_i$ of each subsystem, that is,

$$\mathcal{H} = \mathcal{H}_0 \otimes \mathcal{H}_1 \otimes ... \otimes \mathcal{H}_{d-1}. \tag{2.6}$$

In particular, if all the subsystems are prepared in a pure state $\{|\psi_i\rangle\}$, the state of the system is

$$|\psi\rangle = |\psi\rangle_0 \otimes |\psi\rangle_1 \otimes ... \otimes |\psi\rangle_{d-1}. \tag{2.7}$$

Similarly, for a mixed state ρ we have

$$\rho = \sum_i p_i \rho_0^i \otimes \rho_1^i \otimes .... \otimes \rho_{d-1}^i, \tag{2.8}$$

for some probability distribution p_i such that $\sum_i p_i = 1$. If a state can be written in the form (2.7) or (2.8), we call it *separable*. Otherwise, we say it is *entangled*.

The state represented by each subsystem in (2.8) is known as the *reduced density matrix*. It allows us to precisely describe the subsystem of a larger system by tracing over the subspaces we are not interested in. To define it, let us consider the simplest case where the composite system is in a two-dimensional Hilbert space $\mathcal{H} = \mathcal{H}_A \otimes \mathcal{H}_B$, then the reduced density matrix of the A subsystem is

$$\begin{aligned}
\rho_A &= \mathrm{tr}_B\{\rho_{AB}\} && \text{(2.9a)}\\
&= \sum_i p_i \,\mathrm{tr}_B\{\rho_A^i \otimes \rho_B^i\} && \text{(2.9b)}\\
&= \sum_i p_i \rho_A^i \,\mathrm{tr}\{\rho_B^i\} && \text{(2.9c)}\\
&= \sum_i p_i \rho_A^i, && \text{(2.9d)}
\end{aligned}$$

where $\mathrm{tr}_B(\cdot)$ is the *partial trace* over $\mathcal{H}_B$.

2.3.1 Bell States

A special type of entangled states are Bell states. For two qubits, the basis of the maximally entangled Bell states can be written as

$$\left|\Psi^{\pm}\right\rangle_{AB} = \frac{1}{\sqrt{2}}(|0\rangle_A |1\rangle_B \pm |1\rangle_A |0\rangle_B), \tag{2.10a}$$

$$\left|\Phi^{\pm}\right\rangle_{AB} = \frac{1}{\sqrt{2}}(|0\rangle_A |0\rangle_B \pm |1\rangle_A |1\rangle_B). \tag{2.10b}$$

If we want to scale up in dimensionality (for powers of two), we can take two Bell states and combine them, such that we have a maximally entangled Bell state in a Hilbert space $\mathcal{H} = \mathbb{C}^4$

$$\left|\Phi^{+}\right\rangle \left|\Phi^{+}\right\rangle = \frac{1}{2}(|0\rangle_A |0\rangle_B + |1\rangle_A |1\rangle_B)(|0\rangle_A |0\rangle_B + |1\rangle_A |1\rangle_B) \tag{2.11}$$

$$= \frac{1}{2}(|0\rangle_A |0\rangle_B + |1\rangle_A |1\rangle_B + |2\rangle_A |2\rangle_B + |3\rangle_A |3\rangle_B), \tag{2.12}$$

where we have relabeled $|0\rangle = |00\rangle$, $|1\rangle = |01\rangle$, $|2\rangle = |10\rangle$, and $|3\rangle = |11\rangle$ for A and B bipartitions. By applying the local Pauli operators X, Z, or combinations of these, we can transform a Bell state into another. For example,

$$(I \otimes Z)\left|\Phi^{+}\right\rangle (ZX \otimes I)\left|\Phi^{+}\right\rangle \rightarrow \left|\Phi^{-}\right\rangle \left|\Psi^{-}\right\rangle. \tag{2.13}$$

Thus, we can find 16 different transformations that give us 16 orthogonal Bell states that form a basis for $d = 4$

$$\begin{aligned}
\left|\Psi^{\pm}\right\rangle \left|\Psi^{\pm}\right\rangle &= \frac{1}{2}(|0\rangle_A |1\rangle_B \pm |1\rangle_A |0\rangle_B)(|1\rangle_A |0\rangle_B + |0\rangle_A |1\rangle_B), \\
\left|\Phi^{\pm}\right\rangle \left|\Phi^{\pm}\right\rangle &= \frac{1}{2}(|1\rangle_A |1\rangle_B + |0\rangle_A |0\rangle_B)(|1\rangle_A |1\rangle_B + |0\rangle_A |0\rangle_B), \\
\left|\Psi^{\pm}\right\rangle \left|\Phi^{\pm}\right\rangle &= \frac{1}{2}(|0\rangle_A |1\rangle_B \pm |1\rangle_A |0\rangle_B)(|1\rangle_A |1\rangle_B + |0\rangle_A |0\rangle_B), \\
\left|\Phi^{\pm}\right\rangle \left|\Psi^{\pm}\right\rangle &= \frac{1}{2}(|1\rangle_A |1\rangle_B + |0\rangle_A |0\rangle_B)(|0\rangle_A |1\rangle_B \pm |1\rangle_A |0\rangle_B).
\end{aligned} \tag{2.14}$$

Nevertheless, this is not the only way to define Bell states for higher dimensions. We could apply the following local transformation over (2.12) also when $d = 4$

$$X^m |j\rangle_d \rightarrow |j \oplus m\rangle, \tag{2.15}$$

$$Z_d^n |j\rangle \rightarrow \omega_d^{jn} |j\rangle, \tag{2.16}$$

with $\omega_d^{jn} = e^{i\frac{2\pi}{d}jn}$ and $\oplus$ the sum modulo d. Using these transformations on state (2.12), we can have a set of maximally entangled Bell states of the form

$$|\mathcal{B}_{n,m}\rangle = \frac{1}{\sqrt{d}} \sum_{j=0}^{d-1} e^{i\frac{2\pi}{d}jn} |j\rangle_A |j \oplus m\rangle_B, \tag{2.17}$$

2.3.2 Mutually Unbiased Bases

Two orthonormal bases $\{|e_1\rangle, ..., |e_d\rangle\}$ and $\{|f_1\rangle, ..., |f_d\rangle\}$ in a Hilbert space $\mathcal{H} = \mathbb{C}^d$ are called mutually unbiased bases (MUBs) if they satisfy

$$|\langle e_i| f_j\rangle|^2 = \frac{1}{d}, \tag{2.18}$$

for all $i, j \in \{1, ..., d\}$. In general, for such d dimensional Hilbert space $\mathcal{H}$, we have $d + 1$ MUBs whenever d is a prime power [46]. Therefore, for $d = 4$, there are five mutually unbiased bases of the form

$$M_0 = \{(1,0,0,0), (0,1,0,0), (0,0,1,0), (0,0,0,1)\}, \tag{2.19a}$$

$$M_1 = \left\{\frac{1}{2}(1,1,1,1), \frac{1}{2}(1,1,-1,-1), \frac{1}{2}(1,-1,-1,1), \frac{1}{2}(1,-1,1,-1)\right\}, \tag{2.19b}$$

$$M_2 = \left\{\frac{1}{2}(1,-1,-i,-i), \frac{1}{2}(1,-1,i,i), \frac{1}{2}(1,1,i,-i), \frac{1}{2}(1,1,-i,i)\right\}, \tag{2.19c}$$

$$M_3 = \left\{\frac{1}{2}(1,-i,-i,-1), \frac{1}{2}(1,-i,i,1), \frac{1}{2}(1,i,i,-1), \frac{1}{2}(1,i,-i,1)\right\}, \tag{2.19d}$$

$$M_4 = \left\{\frac{1}{2}(1,-i,-1,-i), \frac{1}{2}(1,-i,1,i), \frac{1}{2}(1,i,-1,i), \frac{1}{2}(1,i,1,-i)\right\}, \tag{2.19e}$$

where the elements of M_i are the vectors of the basis.

2.4 Measurements

Quantum measurements are described by a collection $\{M_m\}$ of measurement operators acting on the Hilbert space of the system being measured. These operators satisfy the completeness relation

$$\sum_{m=1}^{n} M_m^\dagger M_m = \mathbb{I}, \tag{2.20}$$

where the index m refers to the measurement outcomes that may occur in the experiment. If the state of the quantum system is $|\psi\rangle$, the probability of obtaining the outcome labeled by m immediately before the measurement is

$$p(m) = \langle\psi| M_m^\dagger M_m |\psi\rangle, \tag{2.21}$$

and the state of the system immediately after the measurement is

$$|\psi_m\rangle = \frac{M_m |\psi\rangle}{\sqrt{\langle\psi| M_m^\dagger M_m |\psi\rangle}}. \tag{2.22}$$

Instead, if the state of the quantum system is a density matrix ρ, the probability of obtaining the outcome m is

$$p(m) = \mathsf{tr}(M_m^\dagger M_m \rho), \tag{2.23}$$

and the state immediately after the measurement is

$$\rho_m = \frac{M_m \rho M_m^\dagger}{\mathsf{tr}(M_m^\dagger M_m \rho)}. \tag{2.24}$$

From the previous results, we can notice that in quantum mechanics, we can only probabilistically predict the outcome of the measurement, and furthermore, by the act of measuring, we perturb the state of the system. This is one of the main differences with classical mechanics, where we can typically predict the measurement outcomes with certainty, and the physical properties of the system can, in principle, be left unperturbed by the measurement process.

2.4.1 Projective measurements

The simplest type of measurement is the *projective measurement*, which is defined by a Hermitian operator $\mathcal{O}$ called *observable*. This operator has a spectral decomposition

$$\mathcal{O} = \sum_m p_m \left|m\right\rangle \left\langle m\right|, \tag{2.25}$$

where $P_m = \left|m\right\rangle \left\langle m\right|$ is a projector, and $\left|m\right\rangle$ and p_m are the respective eigenvectors and eigenvalues of the operator $\mathcal{O}$. In addition to being Hermitian, projectors are idempotent ($P_m^2 = P_m$) since the eigenstates $\left|m\right\rangle$ are orthogonal. In this way and according to (2.23), the probability to obtain an outcome p_m upon measuring the state $\rho = \left|\psi\right\rangle \left\langle\psi\right|$ is

$$p(m) = \mathsf{tr}\{P_m^\dagger P_m \rho\} \tag{2.26a}$$

$$= \mathsf{tr}\{P_m \rho\} \tag{2.26b}$$

$$= \left\langle m\right| \rho \left|m\right\rangle, \tag{2.26c}$$

and recalling (2.24) the state after the measurement is $\rho_m = \left|m\right\rangle \left\langle m\right|$.

2.4.2 Bell-state Measurement

An important projective measurement is those performed on the Bell basis, the so-called Bell state measurement (BSM). This type of measurement is crucial for many quantum communication protocols and quantum information tasks such as quantum teleportation [1, 47, 48], super dense coding [35, 49], quantum repeaters [50, 51], quantum target detection [52], entanglement swapping [53], and quantum computing [54].

As a simple example to illustrate the importance of BSM, we can study their usefulness in the entanglement swapping protocol. Let's consider that Alice has the state $\left|\Phi^+\right\rangle_{AC}$, and Bob has $\left|\Phi^+\right\rangle_{BD}$. Each one sends one of their photons to a BSM that performs a projective measurement onto one of the entangled Bell states. For the sake of simplicity, consider that the result corresponds to the projection given by $\Pi_{CD} = \left|\Phi^+\right\rangle_{CD} \left\langle\Phi^+\right|_{CD}$, as is shown in Figure 2.1. The state of the unmeasured photons is equal to

$$\rho_{AB} = \mathrm{tr}_{CD}\{\Pi_{CD} \left|\Phi^+\right\rangle_{AC} \left|\Phi^+\right\rangle_{BD} \left\langle\Phi^+\right|_{AC} \left\langle\Phi^+\right|_{BD}\} = \left|\Phi^+\right\rangle_{AB} \left\langle\Phi^+\right|_{AB}. \tag{2.27}$$

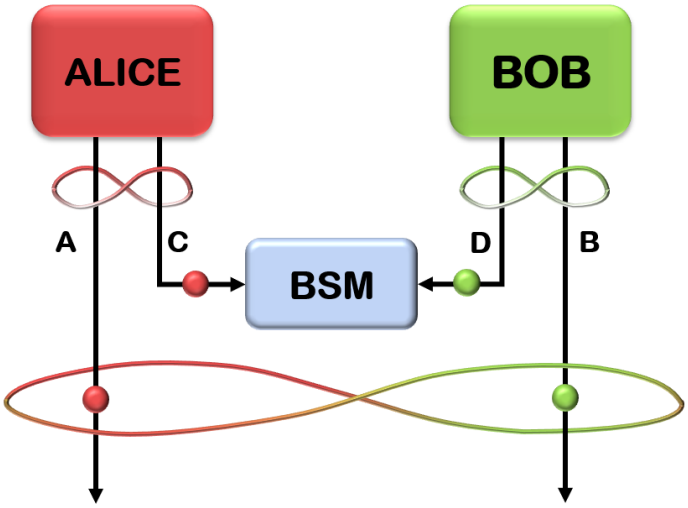

Figure 2.1: Illustration of the entanglement swapping protocol. Alice and Bob have a pair of entangled photons in the partitions $\{A, C\}$ and $\{B, D\}$, respectively. Each one sends one of its photons to a BSM. As a result, the two unmeasured photons, that were produced independently and have never interacted before, are now entangled. Source: made by the author.

As we can see, the resulting unmeasured photons produced independently and never previously interacted are now entangled thanks to the BSM.

A device that contains all the BSM for a given dimension is called a Bell-state analyzer (BSA), and ideally, it can distinguish any arbitrary Bell state as input. Further on in chapter 5 of this thesis, we will study a BSA in dimensions 2 and 4.

2.5 Fidelity

A common measure of closeness between quantum states is fidelity. In general, for two density operators acting on the same Hilbert space, the fidelity is given by

$$F(\rho, \sigma) = \left(\mathrm{tr} \sqrt{\sqrt{\rho}\sigma\sqrt{\rho}} \right)^2 . \tag{2.28}$$

Some of the important properties of quantum state fidelity are:

a) (Bounded values) $F(\rho, \sigma) \in [0, 1]$. Note that $F(\rho, \sigma) = 1$ if and only if $\rho = \sigma$.

b) (Simplified expression) If σ represent a pure state, $\sigma = |\psi_\sigma\rangle \langle\psi_\sigma|$, then the fidelity can be calculated as

$$F(\rho, \sigma) = \langle\psi_\sigma|\rho|\psi_\sigma\rangle. \tag{2.29}$$

c) (Symmetry) $F(\rho, \sigma) = F(\sigma, \rho)$.

2.6 Measure of Quantum Correlations

Quantification of quantum correlations present in a quantum state is important to understand and efficiently use the state for quantum information protocols. Here we introduce three measures for correlations, the first two for entanglement and the third one for non-classical correlations in general.

2.6.1 Negativity and Logarithmic Negativity

In particular, negativity is a measure of bipartite quantum entanglement. It was derived from the positive partial transpose (PPT) criterion for separability [55]. Negativity for a subsystem A is defined as

$$\mathcal{N}(\rho) \equiv \frac{\left\|\rho^{\Gamma_A}\right\|_1 - 1}{2}, \tag{2.30}$$

and vanishes for unentangled states [56]. Here ρ^{Γ_A} is the partial transpose with respect to the part A of the bipartite quantum state, and $\|X\|_1 = \mathrm{tr}\{\sqrt{X^\dagger X}\}$ is the trace norm. For a separable state ρ acting on $\mathcal{H}_A \otimes \mathcal{H}_B$ the partial transpose of ρ with respect the subsystem A is

$$\rho^{\Gamma_A} := (I \otimes T)(\rho) = \sum_{ijkl} p_{kl}^{ij} (|i\rangle\langle j|)^T \otimes |k\rangle\langle l| = \sum_{ijkl} p_{kl}^{ij} |j\rangle\langle i| \otimes |k\rangle\langle l|. \tag{2.31}$$

According to Ref. [57], a more easily interpreted and useful quantity is given by the logarithmic negativity, defined as follows

$$LN(\rho) = \log_2 ||\rho^{\Gamma_A}||_1. \tag{2.32}$$

2.6.2 Quantum Discord

Two systems are correlated if together they contain more information than when we treat them separately. This intuitive definition is formally captured by mutual information. For two classical systems with random variables A and B, the mutual information is

$$I(A:B) = H(A) + H(B) - H(A,B), \tag{2.33}$$

where the Shannon entropy is denoted by $H(A) = -\sum_a p(a) \log p(a)$ which describes the ignorance about the random variable A with values a occurring with probability $p(a)$, while $H(A,B)$ is the Shannon entropy of the joint probability distribution $p(a,b)$. According to Fig. 2.2, mutual information can be also written as

$$J(A:B) = H(A) - H(A|B), \tag{2.34}$$

with $H(A|B) = \sum_b p(b) H(A|B = b)$ being the Shannon entropy of A conditioned on the measurement of B, i.e, the random variable A depends upon the measurement B and the resulting outcome b. Note that both descriptions for the mutual information, (2.34) and (2.33),

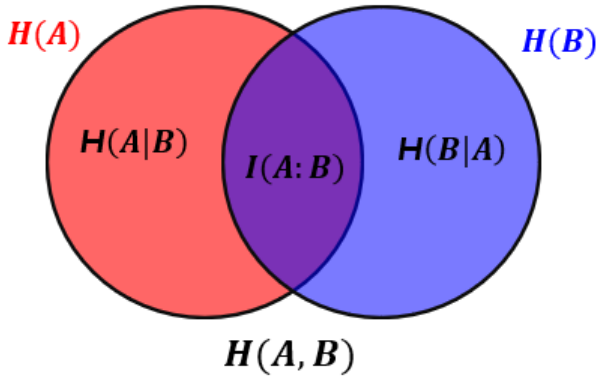

Figure 2.2: Venn diagram to show how different measures of information associated with the correlated variables A and B are related. The circle on the left (red and violet) is the Shannon entropy $H(A)$, with the red being the Shannon conditional entropy $H(A|B)$. The circle on the right (blue and violet) is the Shannon entropy $H(B)$, with the blue being $H(B|A)$. The area contained by both circles is the Shannon joint entropy $H(A, B)$, and the intersection (violet area) is the mutual information $I(A : B)$. Source: made by the author.

are equivalent.

For quantum systems, we replace the classical probability distributions by the density matrices of two parties ρ_A, ρ_B and ρ_{AB}, the Shannon entropy by the Von Neumann entropy $S(\rho) = -\mathsf{tr}\{\rho \log(\rho)\}$, and the conditional Shannon entropy by the conditional Von Neumann entropy $S(\rho_A|\rho_B)$. Thus, we can define the quantum mutual information and its alternative version, analogous to (2.33) and (2.34) as follows

$$I(\rho) = S\left(\rho_A\right) + S\left(\rho_B\right) - S(\rho_{\mathsf{AB}}), \tag{2.35}$$

$$J_A(\rho) = S\left(\rho_B\right) - S\left(\rho_A|\rho_B\right). \tag{2.36}$$

Contrary to the classical case, equations generally (2.35) and (2.36) differ when the systems involved share quantum correlations since measurements of B giving an outcome b can perturb the states of A. The difference between these two quantities defines quantum discord [58]

$$\mathcal{D}_A(\rho) = I(\rho) - J_A(\rho). \tag{2.37}$$

Note that J_A represents the part of the correlations that can be attributed to classical correlations, and these depend on the eigenbasis in which we are measuring. To ensures that J_A captures all classical correlations independently of the measurement, it is necessary to maximize over the set of all possible projective measurements $\{P_j^A\}$

$$\mathcal{D}_A(\rho) = I(\rho) - \max_{\{P_j^A\}} J(\rho)_{\{P_j^A\}}. \tag{2.38}$$

This definition of Quantum discord can be interpreted as the minimal loss of classical correlations due to the local projective measurements.

Quantum discord has the following properties [59]:

a) It is not symmetric, i.e., in general, $\mathcal{D}_A \neq \mathcal{D}_B$, which is expected since the conditional entropy is not symmetric.

b) For pure states, it is a measure of entanglement.

c) Is non-negative, $\mathcal{D}_A \geq 0$.

d) Is invariant under local unitary transformations, since $\rho_{AB} = (\mathsf{U}_A \otimes \mathsf{U}_B)\rho_{AB}(\mathsf{U}_A \otimes \mathsf{U}_B)^\dagger$.

e) Discord is bounded from above as $\mathcal{D}_A \leq S(\rho_A)$, while $J_A \leq \min\{S(\rho_A), S(\rho_B)\}$.

f) Discord vanishes, $\mathcal{D}_A = 0$, if and only if the state is classical-quantum (see below).

A bipartite state ρ_{AB} is classical-quantum (CQ) like (or quantum-classical when A exchanges roles with B) if it can be written as

$$\rho_{AB} = \sum_i p_i \left|\psi_i\right\rangle \left\langle\psi_i\right| \otimes \rho_i, \tag{2.39}$$

where $\{|\psi_i\rangle\}$ is an orthonormal basis, $\{p_i\}$ is a probability distribution, and ρ_i are the quantum states in B [60]. Then, the CQ states have zero discord because there always exists a von Neumann measurement $\{P_i = |\psi_i\rangle \langle\psi_i|\}$ such that

$$\sum_i (P_i \otimes \mathbb{I}_B)\rho_{AB}(P_i \otimes \mathbb{I}_B) = \rho_{AB}. \tag{2.40}$$

So the measurement on A does not perturb the state [59].

2.6.3 Geometric quantum discord

As one might guess, evaluation of the quantum discord in the form of eq. (2.38) in general requires considerable numerical minimization. An analytical expression of this correlation quantifier was derived by Dakic *et al.* [61] for a two-qubit case. They begin by proposing the following geometric measure of quantum discord

$$\mathcal{D}(\rho) = \min_{\chi \in \Omega_0} \|\rho - \chi\|^2, \tag{2.41}$$

where Ω_0 denotes the set of zero-discord states and $||\cdot||^2 = \mathrm{Tr}(\cdot)^2$ is the square norm in the Hilbert-Schmidt space. We can see that the last two definitions of quantum discord are similar in the sense that both seek to minimize the discord, whether over a set of states or measurements. Definition (2.38) does this by maximizing J_A over a set of measurements, and (2.41) does it by minimizing the distance between ρ and a set of zero-discord states Ω_0.

Hence, in the particular case where our state is composed of two qubits with Hilbert space $\mathcal{H}_A = \mathcal{H}_B = \mathbb{C}^2$, we can write the density matrix ρ in its Bloch representation [62]:

$$\rho = \frac{1}{4}\left(\mathbb{I}_2 \otimes \mathbb{I}_2 + \sum_{i=1}^{3} r_A^i \sigma_i \otimes \mathbb{I}_2 + \sum_{i=1}^{3} r_B^i \mathbb{I}_2 \otimes \sigma_i + \sum_{i,j=1}^{3} C_{ij}\sigma_i \otimes \sigma_j\right), \tag{2.42}$$

where $\mathbb{I}_2$ is the 2×2 identity matrix, the vectors $r_A^i = \mathrm{tr}\{\rho(\sigma_i \otimes \mathbb{I})\}$ and $r_B^i = \mathrm{tr}\{\rho(\mathbb{I} \otimes \sigma_i)\}$ are components of the local Bloch vectors, $C_{ij} = \mathrm{tr}\{\rho(\sigma_i \otimes \sigma_j)\}$ is the correlation tensor, and σ_i are the Pauli matrices. Then, taking into account a zero-discord state of the form

$$\chi = p_1|\psi_1\rangle\langle\psi_1| \otimes \rho_1 + p_2|\psi_2\rangle\langle\psi_2| \otimes \rho_2, \tag{2.43}$$

and further calculations detailed in [61], we will have that equation (2.41) can be also written as

$$\mathcal{D}(\rho) = \frac{1}{2}(\|\vec{r}_A\|^2 + \|C_{ij}\|^2 - k_{\max}), \tag{2.44}$$

with k_{max} the largest eigenvalue of the matrix $K = \vec{r}_A\vec{r}_A^T + CC^T$. So, this expression can be easily calculated analytically whenever we can write the state in its Bloch representation.

Chapter 3

Quantum Information with Fiber Devices

We can use different physical systems to encode quantum information [8]. Some of these are photons [9], atoms [63], nuclear spin [64], electron spin systems [65], Josephson junctions and superconducting devices [66]. However, photons stand out as an effective system to process and encode information since they are transportable and propagate fast, are easy to manipulate, and do not interact with the environment, which implies high coherence [9].

To work with photons, there are many degrees of freedom (dof) to encode the information. On the one hand, we could use polarization, but it is limited to dimension two, so it is commonly used to generate qubits [67]. On the other hand, for higher dimensions, we could use orbital angular momentum (OAM), which is used for experiments of high-dimensional entangled states with spontaneous parametric down-conversion (SPDC) [18, 68, 69]. For the generation and measure of OAMs, there are commercially available spatial light modulators. However, they cannot propagate in single-mode fibers (only multimode, which has high losses compared to SMF), so they are not yet so useful for quantum communications with the current fiber technology [16]. Another option is to encode photons in linear momentum dof, i.e., in the propagation direction of the photon. This "path-encoding" is more convenient if we want to work with optical fibers. As we increase the path modes, we also increase the dimension of our system, as we will see below.

In this chapter, we first show in section 3.1 how to transmit photonic quantum states in optical fiber, focusing on multicore fibers. Then in section 3.2 we present the central device of this thesis, the 4×4 multicore fiber beam splitter. Finally, in section 3.3, we show the second quantization formalism that will help us to work more efficiently with the states that will be input to the 4×4 beam splitter.

3.1 Transmission of Photonic Quantum States

One way to send photons encoded in path information from one place to another is through an optical fiber, which is a waveguide made of materials that have low-loss [70]. Nowadays, the most commonly used fibers are single-core fibers, like the one shown in Fig 3.1. The cladding covers the core, which has a slightly lower refractive index. This characteristic allows the light to be confined within the core due to the total internal reflection along the direction of the fiber axis. The number of modes M supported by a single-core fiber is restricted by the parameter

$$V = 2\pi \left(\frac{a}{\lambda}\right) \mathrm{NA}, \tag{3.1}$$

that depends on the radius of the core a, the numerical aperture of the fiber NA and the wavelength λ of the optical field guided by the fiber. When $V < 2.405$ [70], the number of allowed modes is reduced to one, and the fiber is then called *single-mode fiber* (SMF).

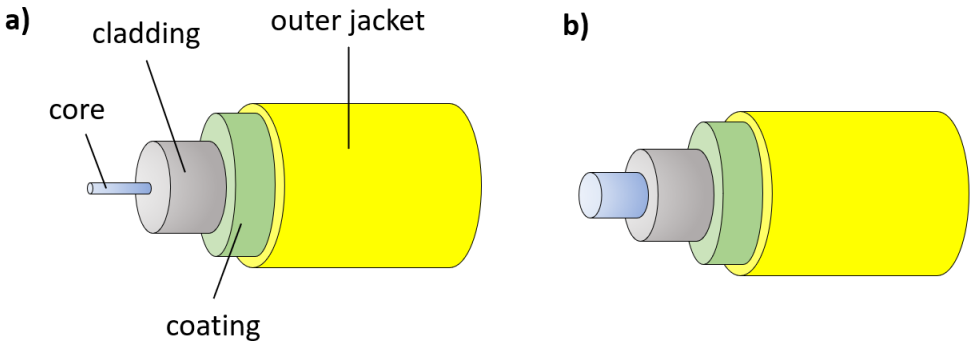

Figure 3.1: Structure of a typical a) single-mode and a b) multimode fiber. a) It is composed of a single-core, with a diameter between 8-10.5 μm, and a cladding generally made of high-quality silica glass. We have an outer coating and an outer jacket to protect these components. b) It has the same structure as an SMF, with the core diameter being greater than 50 μm. Source: made by the author.

However, the data rates in single-mode fibers are nearing their physical limits, known as the "capacity crunch" [10, 11]. For this reason, an important goal in telecommunications is to increase the transmission capacity of optical channels. One promising solution to this problem is the use of multicore optical fibers (MCF) [12]. It is a fiber with multiple cores embedded in a common cladding. Each core is propagated a single mode of light, and it has been shown that the relative phase fluctuations between quantum states propagating in different cores are much more stable and less than for multiple single-mode fibers [13, 14, 15].

An example of a four-core fiber (4CF) is shown in Fig. 3.2. Here, the distance between the closest cores is 50μm, a sufficient distance so that there is no coupling among them. This characteristic allows the spatial mode of each fiber to be treated independently. So, in general, a MCF can be used to propagate qudits states. If we send one photon through a MCF with d

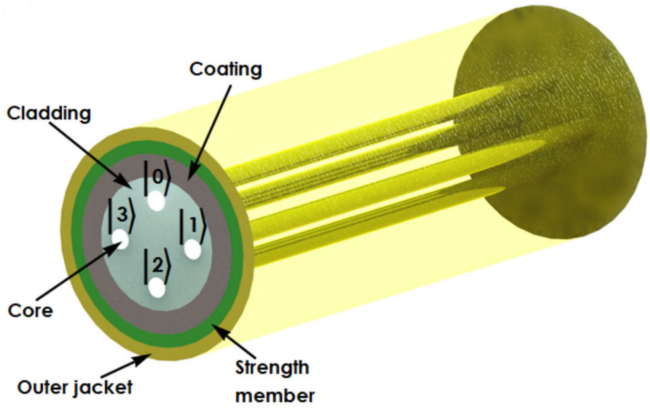

Figure 3.2: Illustration of a multicore optical fiber. The same cladding contains four independent cores, in which only the fundamental mode can be transmitted. Source: taken from [28].

cores, the resulting qudit will be

$$|\Psi\rangle = \sum_{i=0}^{d-1} p_i \, |i\rangle \, , \tag{3.2}$$

where the index indicates the ith core mode through which the photon is propagating. For two photons that are sent by two different cores of the MCF, the state will be

$$|\Psi\rangle = \sum_{\substack{i,j=0 \\ (i\neq j)}}^{d-1} p_{ij} \, |i\rangle \, |j\rangle \, , \tag{3.3}$$

and so on. In the case of sending a photon through a 4CF, the state produced is a ququart (see eq. (2.3)).

3.2 Multicore Devices

We already mentioned that MCFs could be a possible solution for the transmission capacity in telecommunications. However, these types of fibers promise to have an even more significant impact on photonic quantum information protocols [16], and optical devices compatible with MCFs are needed for its implementation.

The first device is the multiplexer (MUX), which involves a group of SMF, each connected to a single core of the MCF. In this way, the MUX makes it possible to send light from standard SMF into MCF and vice versa. Moreover, it allows the independent control of each of the MCF cores. An example of a MUX for a 4CF is shown in Fig. 3.3.

Another novel device is the multicore fiber beam splitter (MCF-BS). It is produced directly

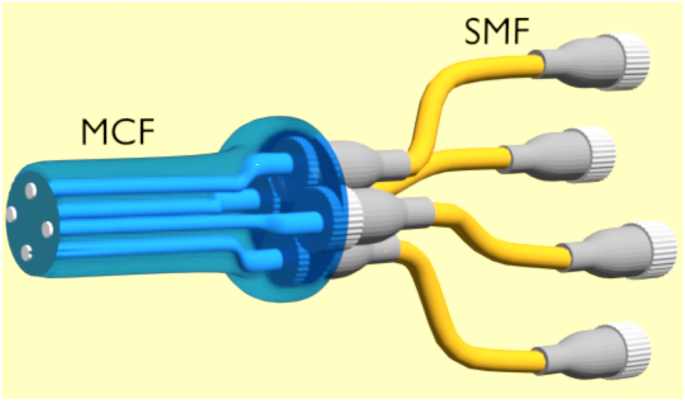

Figure 3.3: Multiplexer device. Single-mode to multicore fiber multiplexer device. Source: taken from [71].

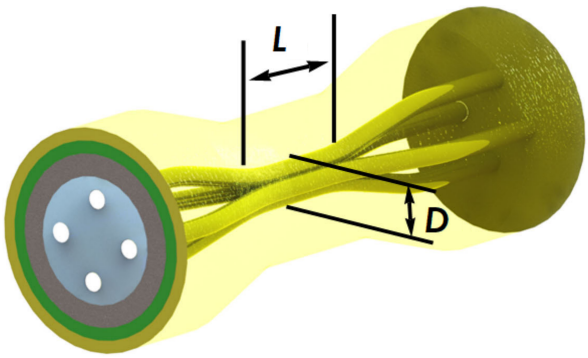

Figure 3.4: Illustration of a 4×4 multicore fiber beam splitter. Source: taken from [28].

from a MCF using a tapering technique [72], which consists of locally heating a small transverse area of the fiber with length L. At the same time, a symmetrical longitudinal tension is applied. Due to the stretching tension, the fiber will become thinner with a final diameter of D at the center of the heated zone. Consequently, the cores become closer together, and light leaks from one core to the others due to evanescent effects.

In particular, for this thesis, we will work with a 4x4 multicore fiber beam splitter (4CF-BS) shown in Fig. 3.4. This device was fully characterized in Ref. [28], where it was shown experimentally and with a quantum tomography process that the unitary matrix that describes the multiport device is

$$B_4 = \frac{1}{2}\begin{pmatrix} 1 & 1 & 1 & 1 \\ 1 & 1 & -1 & -1 \\ 1 & -1 & 1 & -1 \\ 1 & -1 & -1 & 1 \end{pmatrix}. \tag{3.4}$$

Furthermore, the split ratio between the cores is approximately 25%, allowing high-quality second-order [23, 25, 28] and fourth-order [71] interference.

3.3 Quantum States of Light in Fiber

As we presented at the beginning of this thesis, the main resource of this work is the two-photon interference in a 4CF-BS. However, the representation of the state in (3.3) is not the most convenient to use in this context since, for indistinguishable particles, this formalism is redundant, and symmetrization (or anti-symmetrization) must be introduced to eliminate this redundancy. A simpler and more precise description is that of second quantization. In this formalism, the states are represented by the Fock states or photon number state $|n\rangle$, which form a complete basis in a Hilbert space, known as Fock space.

In general, n photons in an arbitrary jth spatial mode of the fiber can be written as

$$(a_j^\dagger)^n |0\rangle = \sqrt{n!}\, |n\rangle_j \,, \tag{3.5}$$

where $a^\dagger$ is the bosonic creation operator acting on the jth mode, and $|0\rangle$ is the vacuum state. The Fock state is an eigenstate of the number operator $\hat{n} = a^\dagger \hat{a}$, with $\hat{a}$ being the annihilation operator, such that

$$\hat{n} |n\rangle = n |n\rangle \,, \quad n \in \mathbb{R}. \tag{3.6}$$

These states are mutually orthogonal $\langle m|n\rangle = \delta_{mn}$, and they form a complete set of orthonormal states, i.e., $\sum_{n=0}^{\infty} |n\rangle \langle n| = \mathbb{I}$.

For bosons, both creation and destruction operators obey the following canonical commutation relations

$$[a_i, a_j^\dagger] = \delta_{ij}, \tag{3.7}$$

$$[a_i, a_j] = [a_i^\dagger, a_j^\dagger] = 0, \tag{3.8}$$

and they act on the state $|n\rangle$ as

$$a^\dagger |n\rangle = \sqrt{n+1}\, |n+1\rangle \,, \tag{3.9}$$

$$a |n\rangle = \sqrt{n}\, |n-1\rangle \,. \tag{3.10}$$

Note that eq. (3.10) is the particular case when $n = 1$ in eq. (3.5). Another observation is that the state in eq. (3.3) can also be written with the second quantization formalism, such as

$$|\Psi\rangle = \sum_{\substack{i,j=0 \\ (i\neq j)}}^{d-1} p_{ij} |1\rangle_i |1\rangle_j = \sum_{\substack{i,j=0 \\ (i\neq j)}}^{d-1} p_{ij} a_i^\dagger |0\rangle a_j^\dagger |0\rangle \,. \tag{3.11}$$

Theoretically, we can describe any unitary transformation in Fock space with quantum mechanics. However, in this thesis, we are especially interested in working on quantum information with indistinguishable photons and linear optics. In this context, the evolution of

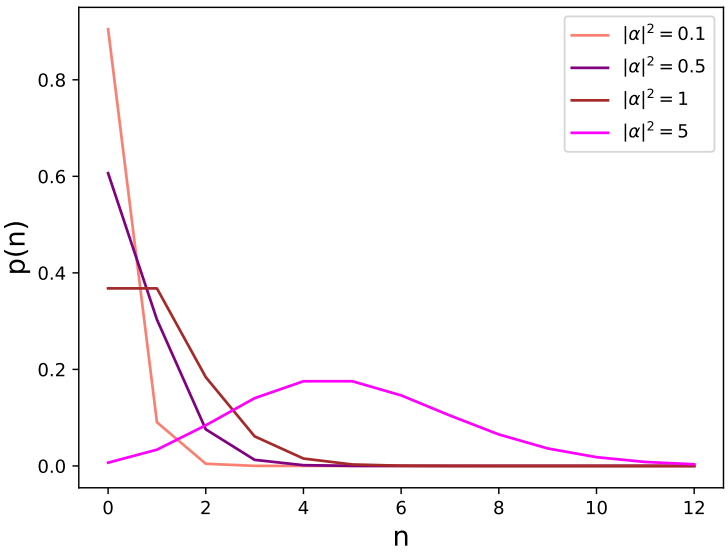

Figure 3.5: Distribution p(n) for a coherent state at different $|\alpha|^2$. Source: made by the author.

the creation operators will be given by a $m \times m$ unitary matrix U such as [73]

$$\vec{a}^{\dagger}_{\text{out}} = U\vec{a}^{\dagger}_{\text{in}}, \tag{3.12}$$

where $\vec{a}^{\dagger}_{in/out} = (a^{\dagger}_1, ..., a^{\dagger}_m)^T$. However, it is difficult to generate pure Fock states for practical purposes. Stable lasers are generally used for experiments using photons. The states that describe the light produced by a laser are coherent states $|\alpha\rangle$, which are eigenstates of the annihilation operator

$$\hat{a}\,|\alpha\rangle = \alpha\,|\alpha\rangle\,, \tag{3.13}$$

with α being a complex amplitude. Coherent states can also be written in the Fock basis as follows

$$|\alpha\rangle = e^{-|\alpha|^2/2} \sum_{n=0}^{\infty} \frac{\alpha^n}{\sqrt{n!}}\,|n\rangle\,. \tag{3.14}$$

Then the probability $p(n)$ that a coherent state contains n photons is

$$p(n) = e^{-|\alpha|^2}\,\frac{|\alpha|^{2n}}{n!}, \tag{3.15}$$

which is a Poissonian distribution, so we find that the mean photon number is $\langle n\rangle = |\alpha|^2$, and the uncertainty is equal to $\Delta n = |\alpha|$. So we can rewrite equation (3.16) as

$$p(n) = e^{-\langle n\rangle}\,\frac{\langle n\rangle^n}{n!}. \tag{3.16}$$

This distribution heavily depends on the value of $|\alpha|^2$, as shown in Fig. 3.5. When $|\alpha|^2 \geq 1$, the distribution is symmetric and resembles a normal distribution. In this limit, one can even make a Gaussian approximation for a distribution centered in $|\alpha|^2$ and with width $|\alpha|$. On the other hand, when $|\alpha|^2 \leq 1$, we have an asymmetric distribution weighted heavily towards the lower values of n. In the latter limit, the states are called *weak coherent states* and can be viewed as an approximation to a superposition of a few Fock states, say from zero to three photons, since the probability of having a larger number decays drastically.

Chapter 4

Maximazing Quantum Discord

Using classical weak coherent states as inputs as telecom wavelengths, we study fourth-order interference in a 4 × 4 multi-port beam splitter and show that quantum correlations, in the form of geometric quantum discord, can be controlled and maximized by adjusting the intensity ratio between the two inputs. Though discord does not imply entanglement [58], recent studies have shown that it plays an important role in quantum tasks such as quantum computing [40], remote state preparation [41], quantum cryptography [42], quantum illumination and metrology [43, 44]. A more comprehensive review of discord and its relation to quantum phenomena and protocols can be found in Refs. [59, 74, 75].

The novelty of this work is two-fold. The first aspect is based on the use of the 4CF-BS. To our knowledge, there have been very few single-photon experiments using this device [23, 25, 28]. Moreover, experiments using more than one photon have only been reported once before [26]. Thus, our study of two-photon interference with weak coherent states is novel in this regard, as it used this new device completely compatible with multi-core fiber infrastructure and that has not been widely considered for quantum information technology.

Secondly, while there are already experiments producing quantum discord from the interference of coherent states at a 2 × 2 beam splitter (Ref. [38]), as far as it is known this experimental scheme has not been investigated any further. For example, how can one control the amount of discord, or the type of states produced? Here we provide some answers to these questions by showing how one can manipulate the input state to the beam splitter to maximize the discord. To the best known, this is the only way to increase discord without altering the Poissonian statistics of the input states.

The results of this work have been reported in *npj Quantum Inf* **7**, 172 (2021) [71].

4.1 Experimental Setup

We constructed an experimental setup shown in Fig. 4.1. We start with a continuous wave laser of wavelength $\lambda = 1546$nm, that is coupled through a SMF to a lithium niobate (LiNbO3) intensity modulator (IM), producing a train of 5 ns width quasi-Gaussian pulses at a repetition rate of 2.78 MHz. The pulses are attenuated and sent into a SMF 50/50 fiber beam splitter (BS0), obtaining two weak coherent states (WCS) (see Section 3.3). These pulses were attenuated in order to have an average photon number of $|\alpha|^2 = 0.46$ at the detectors. This implies that 36.9% of the pulses will have one or more photons. Of these non-vacuum events, 78.8% correspond to pulses containing only a single photon, 18.1% to two photons, and only 3% to more than two photons (see eq. (3.16)).

One of the outputs of the BS0 is connected to a polarizer controller (PC), which is used to set the polarization between the pulses. In the other output of the BS0 we have a 72 m fiber roll which adds a delay to one of the pulses with respect to the other[1]. Since the relative delay is much greater than the coherence length of the laser, the WCSs are mutually incoherent when they overlap at the 4CF-BS. In this way, single photons do not interfere with themselves, so we ensure that there is no second-order interference. However, fourth-order (two-photon) interference can occur when photons reach the inputs $i1$ and $i3$ of the 4CF-BS through MUX1. The 4CF-BS and MUX were well described in Section 3.2.

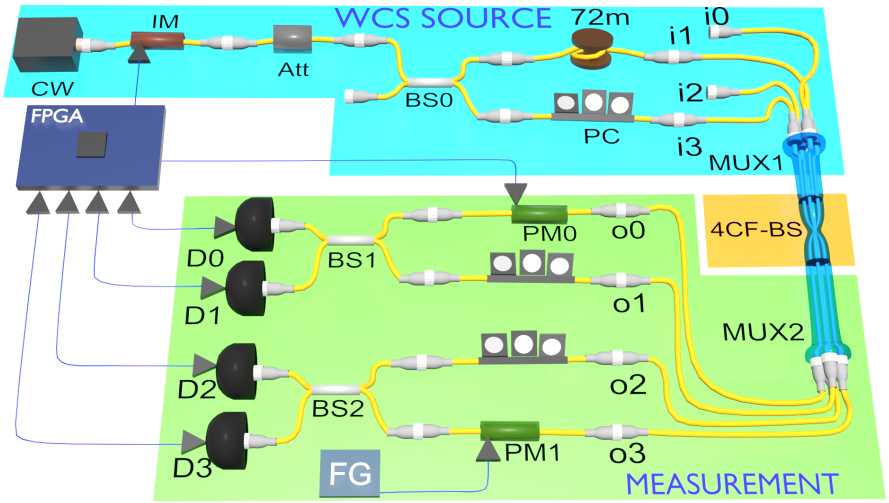

Figure 4.1: Illustration of the experimental setup. Weak coherent pulses interfere incoherently on a four-core fiber beamsplitter. CW: continuous wave laser, IM: intensity modulator, Att: attenuator, BS: single-mode fiber 2×2 beamsplitter, PC: polarizer controller, MUX: fiber multiplexer for single-core SMF fiber to multi-core fiber and vice versa, 4CF-BS: four-core fiber beamsplitter, PM: phase modulation, FG: function generation, D_j: triggered single photon detector (j=0,1,2,3), FPGA: field programmable gate array device.

The four cores of the 4CF-BS are separated into four outputs through a MUX2, which are connected to two independent SMF-based two-arm interferometers. Polarization-noise in the

[1]Photons are delayed 5 ns every 1 m of fiber, so 72 m are equivalent to a delay of 360 ns.

SMF decreases the quality of overlap in each output BS and therefore reduces the visibility of fourth-order interference. To delete polarization information [76, 77], two additional PCs are used in outputs o1 and o2. The interferometers are also phase-controlled with fiber-coupled LiNbO3 phase modulators (PM0 and PM1), which are used to make measurements on differents basis. The PM0 is driven by a field programmable gate array (FPGA), while the PM1 is independently controlled by a simple electrical signal generator, a function generator.

With four triggered single-photon detectors (SPD) we registered coincidence detections for two-photon events. The SPD were configured with 5 ns detection windows and 10% detection efficiency. The pulse generation via IM in the WCS source and the triggered measurements at the SPDs are synchronized by a field programmable gate array (FPGA). Given the pulse generation rate mentioned at the beginning (for $|\alpha|^2 = 0,46$), and the detection efficiency of about 25.000 single counts $\cdot$ s^{-1} are recorded from each SPD. Furthermore, the FPGA is configured to record all possible two-photon coincidence counts in a 1 ns wide coincidence window, achieving a rate of $\approx$ 400 total coincidence counts $\cdot$ s^{-1}.

4.2 Input and Output with Post-Selection

Since we are working with WCS, the mutually incoherent amplitudes obey $|\alpha| \ll 1$ and $|\alpha'| \ll 1$ (see eq. (3.14)). Ignoring terms containing more than two photons, the input state entering the 4CF-BS can be written as

$$\rho_{in} = N[p_2 p_0' \left|2,0\right\rangle \left\langle 2,0\right| + p_0 p_2' \left|0,2\right\rangle \left\langle 0,2\right| + p_1 p_1' \left|1,1\right\rangle\left\langle 1,1\right|] \tag{4.1}$$

where p_n is the Poisson probability distribution given by the equation (3.16), N is a normalization constant, and the bras and kets notation refers to input modes $i1$ and $i3$. Using the fact that $p_2 p_0' = p_1^2/2$, we can rewrite (4.1) as

$$\rho_{in} = N' \left(\left|2,0\right\rangle \left\langle 2,0\right| + \gamma^2 \left|0,2\right\rangle \left\langle 0,2\right| + 2\gamma \left|1,1\right\rangle\left\langle 1,1\right|\right). \tag{4.2}$$

Here the parameter $\gamma = |\alpha|^2/|\alpha'|^2$ is the ratio between mean photon numbers of the input pulses. Without loss of generality, we consider the range $0 \leq \gamma \leq 1$, as $\gamma > 1$ can be handled by simply interchanging α and α'. Be aware that the parameter γ will take an important role during this chapter.

To calculate the output modes of the 4CF-BS we use a PYTHON script (see Appendix A1) where we transform each component using

$$\vec{a}_{\text{out}} = \mathbf{B}_4 \vec{a}_{\text{in}} \tag{4.3}$$

with B_4 given by equation (3.4) and $\vec{a}_{in/out} = (\hat{a}_0^\dagger, \hat{a}_1^\dagger, \hat{a}_2^\dagger, \hat{a}_3^\dagger)^T$. For the two-photon state $\left|2,0\right\rangle = \hat{a}_1^\dagger \left|0,0\right\rangle / \sqrt{2}$ the field operators transform as

$$(\hat{a}_1^\dagger)^2 \rightarrow \frac{1}{4}(\hat{a}_0^\dagger + \hat{a}_1^\dagger - \hat{a}_2^\dagger - \hat{a}_3^\dagger)^2. \tag{4.4}$$

Here and below we omit the subscripts "in", to the left, and "out", to the right. For the state $|0,2\rangle = (a_3^\dagger)^2 |0,0\rangle / \sqrt{2}$ we have

$$(a_3^\dagger)^2 \rightarrow \frac{1}{4}(\hat{a}_0^\dagger - \hat{a}_1^\dagger - \hat{a}_2^\dagger + \hat{a}_3^\dagger)^2. \tag{4.5}$$

Finally, for the state $|1,1\rangle = a_1^\dagger a_3^\dagger |0,0\rangle$ we have the following expression

$$a_1^\dagger a_3^\dagger \rightarrow \frac{1}{4}(\hat{a}_0^{\dagger 2} - \hat{a}_1^{\dagger 2} + \hat{a}_2^{\dagger 2} - \hat{a}_3^{\dagger 2} - 2a_0^\dagger a_2^\dagger + 2a_1^\dagger a_3^\dagger). \tag{4.6}$$

Since photons are indistinguishable[2], when they enter by different modes, it is not possible to identify which of the two followed a certain path. Then the two photons interfere at the 4CF-BS, which explains the absence of the terms $a_0^\dagger a_1^\dagger$, $a_0^\dagger a_3^\dagger$, $a_1^\dagger a_2^\dagger$ and $a_2^\dagger a_3^\dagger$ in eq. (4.6), as they vanish due to destructive interference. This does not occur in terms (4.4) and (4.5), since it is possible to determine which direction the photons followed. We also study two-photon interference experimentally in Section 4.3.

Using the above transformations on the input state (4.2), the output state will be given by a 10×10 density matrix. The elements of the output matrix are given by all possible combinations of two-photon states coming out from the four output cores of the 4CF-BS. For example, state $|2000\rangle$ corresponds to two photons in output mode 0, state $|1010\rangle$ to one photon in mode 0 and one photon in mode 2, state $|0020\rangle$ to two photons in output mode 2 and so on. The complete density matrix was calculated with a PYTHON program (see Appendix A2), such as

$$\rho_{out} = \frac{1}{8}\begin{pmatrix}
\frac{t}{2} & \frac{v}{2} & \frac{t}{2} & \frac{v}{2} & \frac{u}{\sqrt{2}} & -\frac{t}{\sqrt{2}} & -\frac{u}{\sqrt{2}} & -\frac{u}{\sqrt{2}} & -\frac{v}{\sqrt{2}} & \frac{u}{\sqrt{2}} \\
\frac{v}{2} & \frac{t}{2} & \frac{v}{2} & \frac{t}{2} & \frac{u}{\sqrt{2}} & -\frac{v}{\sqrt{2}} & -\frac{u}{\sqrt{2}} & -\frac{u}{\sqrt{2}} & -\frac{t}{\sqrt{2}} & \frac{u}{\sqrt{2}} \\
\frac{t}{2} & \frac{v}{2} & \frac{t}{2} & \frac{v}{2} & \frac{u}{\sqrt{2}} & -\frac{t}{\sqrt{2}} & -\frac{u}{\sqrt{2}} & -\frac{u}{\sqrt{2}} & -\frac{v}{\sqrt{2}} & \frac{u}{\sqrt{2}} \\
\frac{v}{2} & \frac{t}{2} & \frac{v}{2} & \frac{t}{2} & \frac{u}{\sqrt{2}} & -\frac{v}{\sqrt{2}} & -\frac{u}{\sqrt{2}} & -\frac{u}{\sqrt{2}} & -\frac{t}{\sqrt{2}} & \frac{u}{\sqrt{2}} \\
\frac{u}{\sqrt{2}} & \frac{u}{\sqrt{2}} & \frac{u}{\sqrt{2}} & \frac{u}{\sqrt{2}} & w & -u & -w & -w & -u & w \\
-\frac{w}{\sqrt{2}} & -\frac{v}{\sqrt{2}} & -\frac{t}{\sqrt{2}} & -\frac{v}{\sqrt{2}} & -u & t & u & u & v & -u \\
-\frac{u}{\sqrt{2}} & -\frac{u}{\sqrt{2}} & -\frac{u}{\sqrt{2}} & -\frac{u}{\sqrt{2}} & -w & u & w & w & u & -w \\
-\frac{u}{\sqrt{2}} & -\frac{u}{\sqrt{2}} & -\frac{u}{\sqrt{2}} & -\frac{u}{\sqrt{2}} & -w & u & w & w & u & -w \\
-\frac{v}{\sqrt{2}} & -\frac{t}{\sqrt{2}} & -\frac{v}{\sqrt{2}} & -\frac{t}{\sqrt{2}} & -u & v & u & u & t & -u \\
\frac{u}{\sqrt{2}} & \frac{u}{\sqrt{2}} & \frac{u}{\sqrt{2}} & \frac{u}{\sqrt{2}} & w & -u & -w & -w & -u & w
\end{pmatrix}. \tag{4.7}$$

The output state depends explicitly upon the ratio γ between mean photon numbers in the input WCSs such as $t = (1 + 4\gamma + \gamma^2)/(1 + \gamma)^2$, $u = (1 - \gamma)/(1 + \gamma)$, $v = (1 - 4\gamma + \gamma^2)/(1 + \gamma)^2$ and $w = (1 + \gamma^2)/(1 + \gamma)^2$.

[2]For two photons to be indistinguishable, they must have the same characteristics, such as polarization, wavelength, and temporal and spatial length

4.3 Fourth-Order Interference

An analytical way to study fourth-order interference is by considering equal intensity WCSs so that $\gamma = 1$. Thus, the output state will look like

$$\frac{1}{16}\begin{pmatrix}
\frac{3}{2} & -\frac{1}{2} & \frac{3}{2} & -\frac{1}{2} & 0 & -\frac{3}{\sqrt{2}} & 0 & 0 & \frac{1}{\sqrt{2}} & 0 \\
-\frac{1}{2} & \frac{3}{2} & -\frac{1}{2} & \frac{3}{2} & 0 & \frac{1}{\sqrt{2}} & 0 & 0 & -\frac{3}{\sqrt{2}} & 0 \\
\frac{3}{2} & -\frac{1}{2} & \frac{3}{2} & -\frac{1}{2} & 0 & -\frac{3}{\sqrt{2}} & 0 & 0 & \frac{1}{\sqrt{2}} & 0 \\
-\frac{1}{2} & \frac{3}{2} & -\frac{1}{2} & \frac{3}{2} & 0 & \frac{1}{\sqrt{2}} & 0 & 0 & -\frac{3}{\sqrt{2}} & 0 \\
0 & 0 & 0 & 0 & 1 & 0 & -1 & -1 & 0 & 1 \\
-\frac{3}{\sqrt{2}} & \frac{1}{\sqrt{2}} & -\frac{3}{\sqrt{2}} & \frac{1}{\sqrt{2}} & 0 & 3 & 0 & 0 & -1 & 0 \\
0 & 0 & 0 & 0 & -1 & 0 & 1 & 1 & 0 & -1 \\
0 & 0 & 0 & 0 & -1 & 0 & 1 & 1 & 0 & -1 \\
\frac{1}{\sqrt{2}} & -\frac{3}{\sqrt{2}} & \frac{1}{\sqrt{2}} & -\frac{3}{\sqrt{2}} & 0 & -1 & 0 & 0 & 3 & 0 \\
0 & 0 & 0 & 0 & 1 & 0 & -1 & -1 & 0 & 1
\end{pmatrix} \tag{4.8}$$

Then, the probabilities P_{jk} to detect one photon in an output core j and the other in an output mode k, with $j < k$, are $P_{01} = P_{03} = P_{12} = P_{23} = 1/16$ and $P_{02} = P_{13} = 3/16$. Note that these probabilities correspond to the diagonal elements of the 6×6 block in the lower right of the density matrix in eq. (4.8). To verify that these values correspond to two-photon interference, we can study the case of distinguishable photons. So instead of having 10 events with different probabilities, we will have 16 events equally likely. Then, the case in which one photon outputs mode j and the other outputs mode k, and the event in which the opposite occurs, add up to a probability of 1/8. Comparing the indistinguishable and distinguishable cases, we can state that events with $P_{jk} = 1/16 < 1/8$ correspond to interference minima (destructive interference), and those with $P_{jk} = 3/16 > 1/8$ to interference maxima (constructive interference).

In the following, we study two-photon interference experimentally. For this, we review the visibility $\mathcal{V}$, which is a measure that helps us to quantify the quality of the interference. In the case of WCS, the predicted visibility is

$$\mathcal{V} = \frac{\max - \min}{\max + \min} \leq \frac{1}{2}, \tag{4.9}$$

which gives a classical limit for fourth-order interference. In the case of quantum mechanics, unit visibility is achievable in principle with a pair of input Fock states. Therefore, an observation of larger than 50% visibility corresponds to nonclassical behavior [78, 79].

So in our setup, fourth-order interference was explored by rotating the polarization of the input mode $i3$ with the first fiber PC in the WCS source (see Fig. 4.1). Thus, we can change continuously between distinguishable and indistinguishable photons. We can define the output probability as a function of a distinguishability parameter θ related to the overlap between

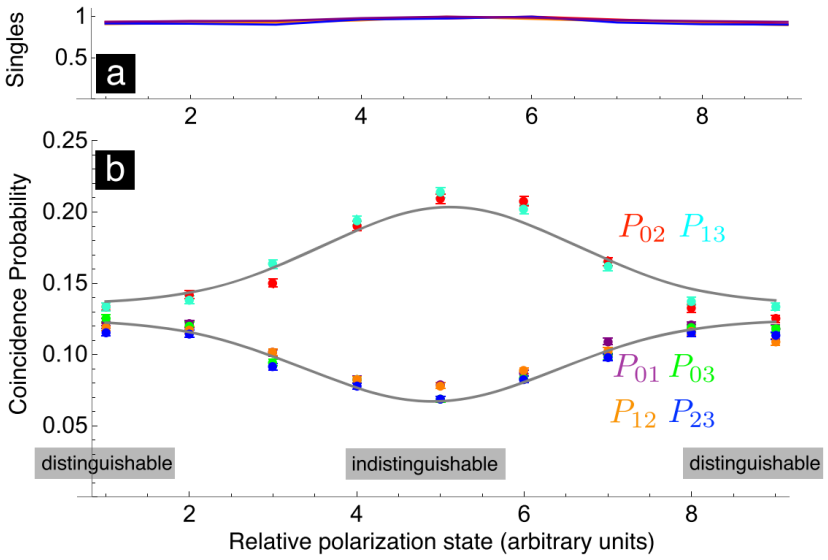

Figure 4.2: Experimental results showing interference of mutually incoherent WCSs at a 4CF-BS. a) Single count probabilities remain unchanged under variation of polarization states. b) Coincidence count probabilities P_{jk} between detectors D_k and D_j showing interference of mutually incoherent WCSs at a 4CF-BS. Constructive and destructive fourth-order interference can be observed in the coincidence probabilities between pairs of detectors as a function of the orthogonality of the polarization states, while the single count probabilities (top) remain unchanged. Error bars (smaller than symbols) correspond to Poissonian count statistics. The solid gray curves represent the gaussian curve that fits experimental data.

polarization states. Then we have

$$P_{jk} = \frac{1}{8}(1 \pm \mathcal{V} f(\theta)), \tag{4.10}$$

where the plus (minus) sigh refers to constructive (destructive) interference and $f(\theta)$ describes the overlap between the polarization states of the two input WCSs. In these measurements, the four SMFs of the MUX2 were directly connected to the SPDs. In Fig. 4.2b are shown the Coincidences counts C_{jk} between detectors D_j and D_k were recorded as a function of θ. When the polarization states are orthogonal, photons are distinguishable, and all combinations of coincidence counts have the same count rates. However, when the polarization is parallel, two-photon interference occurs, resulting in an increase in coincidence counts C_{02} and C_{13}, and suppression of the coincidences at other detector pairs. In Fig. 4.2a the single counts at each detector are shown, which remain constant as the polarization is varied. This confirms that the behavior of the coincidence counts is due to fourth-order interference and not due to an increase or decrease of single counts. For time integrations of 10s, and using the average values at the interference maximum and minimum, we obtain visibility of $\mathcal{V} = 0.48 \pm 0.02$. In this way, the near-perfect visibility shows that we have high-quality fourth-order interference and serves as a benchmark for the quality of the 4CF-BS.

4.4 Post-Selected Bipartite State

As an application of two-photon interference at the 4CF-BS device, we now study the bipartite quantum correlations that can be produced. To do so, we divide the output modes into two partitions; $A \in \{\text{o0,o1}\}$ and $B \in \{\text{o2,o3}\}$. Hence we only consider events where one photon is detected in portion A and the other in partition B.

Following the results from section 4.2, and the total density operator given in (4.7), the post-selected bipartite density operator is

$$\rho(\gamma)_{AB} = \frac{1}{4}\begin{pmatrix} t & u & u & v \\ u & w & w & u \\ u & w & w & u \\ v & u & u & t \end{pmatrix}, \tag{4.11}$$

which corresponds to the ρ^{ij}_{out} elements with $i,j = 6,7,8,9$. Note that normalization requires $t + w = 2$ (see section 2.1). Therefore, the output state depends explicitly upon the ratio γ between mean photon numbers in the input WCSs.

The purity is given by $\text{tr}\{\rho(\gamma)^2_{AB}\} = (1 + 4\gamma^2 + \gamma^4)/(1+\gamma)^4$, and reaches a minimum value of 3/8 when $\gamma = 1$, i.e, when the WCSs have equal intensity. For this specific value of γ, the post-selected matrix results in

$$\rho(1)_{AB} = \frac{1}{8}\begin{pmatrix} 3 & 0 & 0 & -1 \\ 0 & 1 & 1 & 0 \\ 0 & 1 & 1 & 0 \\ -1 & 0 & 0 & 3 \end{pmatrix}. \tag{4.12}$$

This state is diagonal in the Bell-state basis

$$\rho(1)_{AB} = \frac{1}{4}\left(\left|\Phi^+\right\rangle\left\langle\Phi^+\right| + 2\left|\Phi^-\right\rangle\left\langle\Phi^-\right| + \left|\Psi^+\right\rangle\left\langle\Psi^+\right|\right), \tag{4.13}$$

and it is an example of the so-called "X" state, which has been widely studied in the literature [80, 81, 82]. The reduced density matrices for the state in (4.13) are maximally mixed, $\rho_A = \rho_B = \mathbb{I}/2$.

Returning to the general case, the post-selected output state $\rho(\gamma)_{AB}$, despite being separable, displays quantum correlations. To evaluate these correlations, we use the geometric discord $\mathcal{D}$ [61], since it can be calculated without numerical optimization, and can be directly related to figures of merit of quantum tasks [41]. As we saw in section 2.6.3, it is useful to write the state (4.11) in its Bloch representation, such as

$$\rho(\gamma)_{AB} = \frac{1}{4}\left(\mathbb{I}_2 \otimes \mathbb{I}_2 + u\sigma_x \otimes \mathbb{I}_2 + u\mathbb{I}_2 \otimes \sigma_x + \sum_j C_{jj}\sigma_j \otimes \sigma_j\right). \tag{4.14}$$

Here the local Bloch vectors are $\vec{r}_A = \vec{r}_B = (u,0,0)$ and the nonzero elements of the correlation

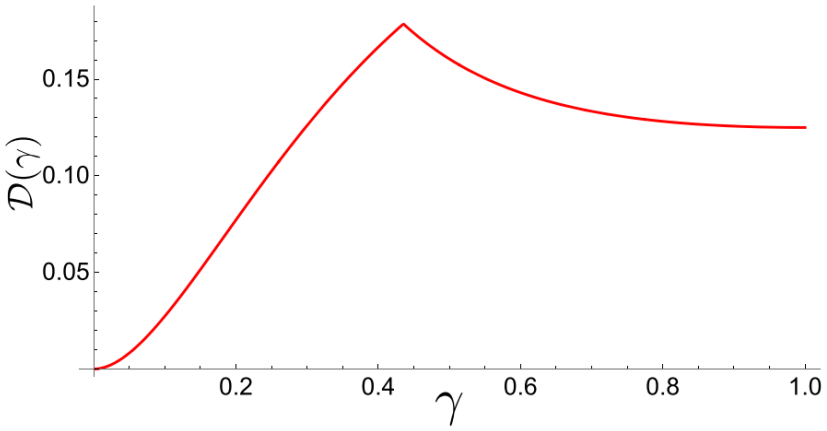

Figure 4.3: Theoretical geometric quantum discord. It reaches a maximum for $\gamma \approx 0.435$ when the two input WCSs have unequal intensities.

matrix between the qubits are

$$C_{xx} = \frac{1}{2}(w + v), \tag{4.15a}$$

$$C_{yy} = \frac{1}{2}(w - v), \tag{4.15b}$$

$$C_{zz} = \frac{1}{2}(t - w). \tag{4.15c}$$

Recalling the definitions of w, v and t, it is easy to see that $C_{xx} = u^2$ and $C_{yy} = C_{zz}$. As a last step, we need to find the maximum eigenvalue of the matrix $K = \vec{r}_A \vec{r}_A^T + CC^T$, which is

$$K = \frac{1}{4}\begin{pmatrix} 4u^2 + (w+v)^2 & 0 & 0 \\ 0 & (w-v)^2 & 0 \\ 0 & 0 & (t-w)^2 \end{pmatrix}, \tag{4.16}$$

with eigenvalues $k_1 = C_{xx} + C_{xx}^2$ and $k_2 = k_3 = C_{yy}^2$, therefore $k_{max} = \max[C_{xx} + C_{xx}^2, C_{yy}^2]$. Following (2.44), the general expression for the geometric quantum discord is

$$\mathcal{D}(\gamma) = \frac{1}{2}\left(C_{xx} + C_{xx}^2 + C_{yy}^2 + C_{zz}^2 - \max\left[C_{xx} + C_{xx}^2, C_{yy}^2\right]\right). \tag{4.17}$$

By plotting this quantity (see figure 4.3), we observe that discord has a maximum value in $\mathcal{D}(\gamma \approx 0.435) = 0.178$, versus $\mathcal{D}(1) = 0.125$ when the intensities of the pulses are equal. As a reference, for a two-qubit separable state the maximum attainable value is $\mathcal{D}_{\text{sep}}^{\max} = 1/4$ [83]. From figure 4.3, we can also notice that discord adopts two behaviors before and after the "kink" in $\gamma \approx 0.435$. It is at this point that there is a change in which argument is maximum for $k_{\max}$. This is more clear to see in Fig. 4.4, where for values of $\gamma \leq 0.435$ we have $k_1 \leq k_2$, then

$$\mathcal{D}(\gamma \leq 0.435) = C_{yy}^2, \tag{4.18}$$

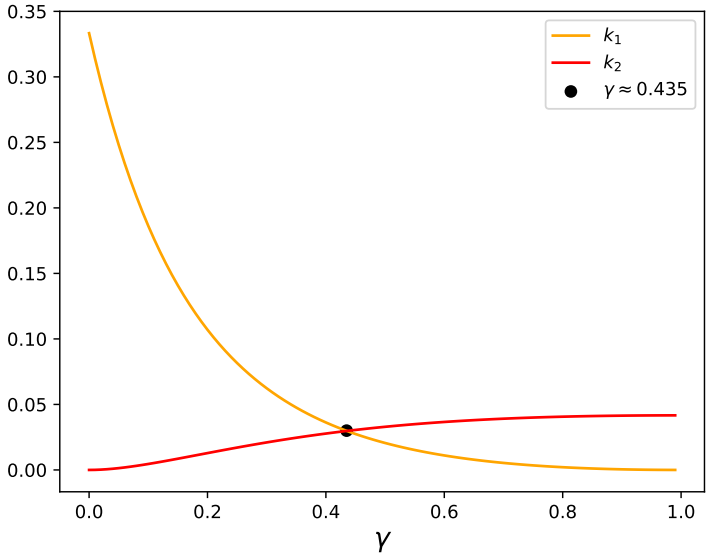

Figure 4.4: Plot to compare the eigenvalues of the matrix K. For values of $\gamma \leq 0.435$ we have $k_2 \geq k_1$ and for the opposite case of γ we have $k_1 \geq k_2$. Note that we have changed the scales for a better visualization. Made by the author (see Appendix A3).

and for greater values of γ we have $k_2 \geq k_1$, so the geometric discord adopts the form of

$$\mathcal{D}(\gamma \geq 0.435) = \frac{1}{2}(C_{xx}^2 + C_{xx} + C_{yy}^2). \tag{4.19}$$

Recall that geometric discord is a minimum distance from the state to the entire set of zero-discord states, i.e, the distance to the closest classical states. Thus, for different values of γ, the state $\rho(\gamma)_{AB}$ can be closer to two different classical states. Therefore, the inflection point is where the state is equidistant to two different states of zero discord. Similar non-analytical points, corresponding to sudden changes of discord have been studied in the context of quantum dynamics quantum [84, 85, 86, 87], phase transitions [88, 89], and quantum-classical transitions [90, 91]. Nevertheless, in our case, the kink appears as a function of the initial conditions γ, and not by any of these transitions. Implying that we can control the type of state produced using the intensity ratio γ.

As a final remark, let's consider the definition of the coherence of a density matrix

$$\mathcal{C}_s = 2|\langle\sigma_+\rangle| = 2|\langle\sigma_x\rangle + i\langle\sigma_y\rangle|. \tag{4.20}$$

This can be shown by taking a generic density matrix $\rho = |\alpha|^2 |0\rangle\langle 0| + \lambda^* |0\rangle\langle 1| + \lambda |1\rangle\langle 0| + |\beta|^2 |1\rangle\langle 1|$, with $\lambda = \alpha^*\beta$. Then, calculating the expectation value of the ladder operator σ_+

with the state ρ, we have

$$\langle\sigma_+\rangle = \mathsf{tr}\{\rho\sigma_+\} = \mathsf{tr}\left\{\begin{pmatrix} |\alpha|^2 & \lambda^* \\ \lambda & 1-|\alpha|^2 \end{pmatrix}\begin{pmatrix} 0 & 1 \\ 0 & 0 \end{pmatrix}\right\} = \lambda. \tag{4.21}$$

Note that factor two in (4.20) appears only by normalization since using the Cauchy-Schwarz inequality we have $|\alpha^*\beta|^2 \leq |\alpha|^2|\beta|^2 = |\alpha|^2(1-|\alpha|^2) \leq 1/4 \Rightarrow \lambda \leq 1/2$. So when the parameter λ reaches its maximum value, the coherence will be equal to one

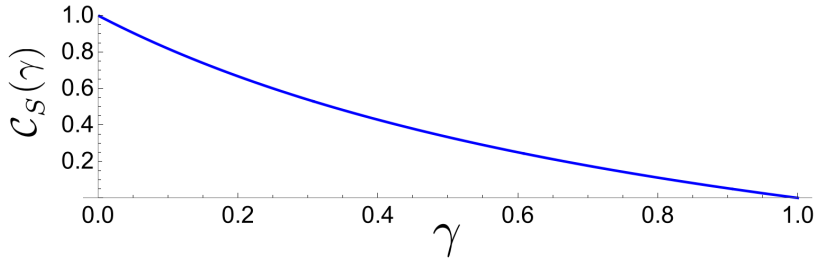

Figure 4.5: Theoretical local coherence for S = A, B. The single-qubit coherence decrease as the intensity mismatch γ goes from 0 to 1.

On the other hand, the reduced density matrices of the output state (4.11) is equal to

$$\rho_S = \frac{1}{2}(\mathbb{I}_2 + u\sigma_x) = \frac{1}{2}\begin{pmatrix} 1 & u \\ u & 1 \end{pmatrix} \quad \text{with } S \in \{A, B\}. \tag{4.22}$$

Then, recalling (4.20), the coherence for ρ_S is $\mathcal{C}_S(\gamma) = |u|$ for each single-qubit. The plot for the marginals coherences is shown in the Fig. 4.5, where it can be seen that it is a linearly decreasing function.

4.4.1 Application: Remote State Preparation

In quantum teleportation [1], the goal is to transmit an unknown state from a sender (Alice) to a receiver (Bob) quantum state. The remote state preparation protocol (RSP) has the same goal, with the difference that Alice sends a known state, in which it has been shown that the classical communication costs are less than those of teleportation [92].

A direct application to the states we produce is for the RSP protocol. Looking in the literature, we notice that the set of states for $\gamma \leq 0.435$ are of the class described by Dakić *et. al* [41]. In this paper, they first show that non-zero quantum discord is the necessary resource for RSP implementation. Secondly, they demonstrate that geometric quantum discord equals fidelity for this protocol. Finally, they prove that states with quantum discord can outperform entangled states in this scenario. According to these results, we note that our separable state in eq. (4.11) achieved a higher discord than the values presented in Ref. [41], so we could achieved even higher fidelities for RSP.

4.5 Experimental Evaluation of Quantum Correlations

Our measurement setup allows us to easily estimate local coherences simultaneously with joint projective measurements. Moreover, following the theoretical model (4.11), the local coherences are monotonic functions of γ. Thus, for convenience, we experimentally estimated the geometric discord $\mathcal{D}$ as a function of the local coherence $\mathcal{C}_S$.

For the measurements, two-arm interferometers were used, where due to the post-selection, each one corresponds to a subsystem, A and B, with an associated spatial qubit. These interferometers can perform projective measurements on the local bases composed of eigenstates of the form

$$|\phi\rangle = \frac{1}{\sqrt{2}}(|0\rangle \pm e^{i\phi}|1\rangle), \tag{4.23}$$

where the state $|0\rangle$ corresponds to the state in the modes $\{o1, o2\}$, and $|1\rangle$ corresponds to the states in the modes $\{o0, o3\}$. The measurements are configured by controlling the phase in each interferometer through PM0 in mode $o0$, and PM1 in mode $o3$. In this case, for $\phi = 0$ we project onto the σ_x eigenstates, while for $\phi = \pi/2$ we project onto the σ_y eigenstates. So the two-path interferometers and phase modulators can be used to directly measure $\langle\sigma_i\rangle_S$, giving the single photon coherence $\mathcal{C}_S$ shown in (4.20), the elements of the correlation matrix C_{ij} for $i, j = x, y$, and the first two elements of the Bloch vector $\vec{r}_S = (\langle\sigma_x\rangle, \langle\sigma_y\rangle, \langle\sigma_z\rangle)$. With this, we are almost able to estimate the discord experimentally, but the elements that depend on σ_z are still missing. On the one hand, considering the near-perfect 25% split ratio of the 4CF-BS and according to our theoretical model, we can approximate $\langle\sigma_z\rangle_S = 0$. Finally, to obtain the full correlation matrix, we need to include the errors in our setup.

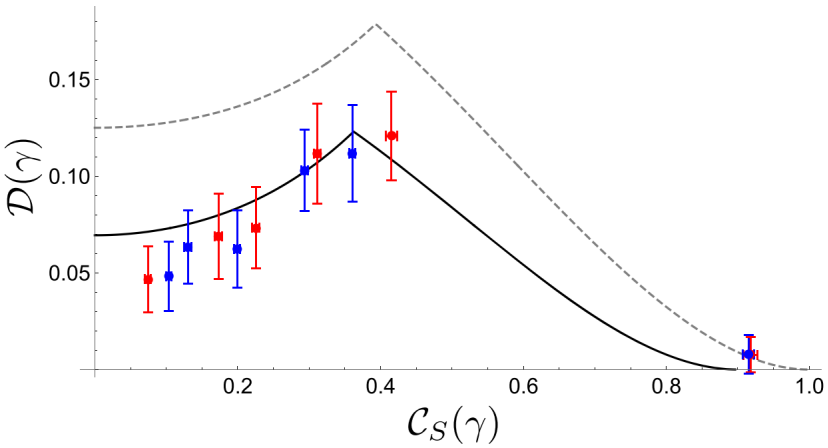

Figure 4.6: Geometric discord $\mathcal{D}$ for the post-selected bipartite output state as a function of the local coherence $\mathcal{C}_\mathbf{S}$ ($\mathbf{S} = \mathbf{A}, \mathbf{B}$). The dashed gray upper curve is the theoretical prediction from (4.17). The red and blue points correspond to experimental points obtained by considering the local marginals coherences of A and B, respectively. The black curve is a theoretical model taking into account dephasing and polarization mode mismatch. The experimental error bars were obtained by Monte Carlo simulation of 500 runs obeying the same Poissonian count statistics.

The main source of errors in our setup corresponds to changes in the polarization state and phase fluctuations within the output fibers in the two-arm interferometers used for measurement. Both of these errors lead to phase damping (dephasing), which does not affect the diagonal elements of the single photon and two-photon density matrices, and can be modeled by considering phase damping channels characterized by a parameter δ [93]. The secondary source of error is the mode mismatch at the 4CF-BS. We modeled mode mismatch by considering an auxiliary dof of each input mode and then traced them out to obtain the relevant quantum state. With this, the two-photon density matrix becomes

$$\rho(\gamma)_{AB} = \frac{1}{4}\begin{pmatrix} t' & u\delta & u\delta & v'\delta^2 \\ u\delta & w' & w''\delta^2 & u\delta \\ u\delta & w''\delta^2 & w' & u\delta^2 \\ v'\delta^2 & u\delta & u\delta & t' \end{pmatrix} \tag{4.24}$$

where $t' = \left(1 + g_+\gamma + \gamma^2\right)/(1+\gamma)^2, u = (1-\gamma)/(1+\gamma)$, $v' = \left(1 - g_+\gamma + \gamma^2\right)/(1+\gamma)^2, w' = \left(1 + g_-\gamma + y^2\right)/(1+\gamma)^2, w'' = \left(1 - g_-\gamma + \gamma^2\right)/(1+\gamma)^2$, and $g_\pm = 2(1 \pm \mathcal{V})$ is due primarily to imperfect polarization mode matching characterized by fourth-order interference visibility ($\mathcal{V} = 0.48 \pm 0.02$) obtained in section 4.3. Here δ is a real parameter that describes the phase damping ($0 \leq \delta \leq 1$) due to fluctuations in the two-arm interferometers.

Measurements with the interferometers are made with respect to zero relative local phases. That is, we use the local interference maxima at detector $D0$ for A, and $D2$ for B to define the phase origin. We characterized the phase damping due to rapid phase fluctuations and changes in the polarization state by analyzing the single-photon interference visibility with only a single WCS input into the setup. We obtained visibilities $\sim 0.9 \pm 0.03$ in this case (averaged over roughly one hour), thus giving $\delta \sim 0.9$. We assume that any additional loss in single photon coherence is due to bipartite correlations. With this, and using the state (4.11) we find that $C_{zz} \approx (1 - \bar{\mathcal{C}})/2$, where $\bar{\mathcal{C}}$ is the local coherence averaged over system A and B. In addition, we take $C_{jz} = C_{zj} \approx 0$ for $j = x, y$, as predicted by the density operator (4.11).

Our experimental results are shown in Figure 4.6. The gray dashed line corresponds to our theoretical model. Red and blue points correspond to discord calculated using the local marginals for system A and B respectively. These do not overlap with the ideal theoretical model due to the experimental imperfections that we already mentioned. The black solid line corresponds to the model considering phase damping, which is compatible with the experimental points. This experimental data show that the quantum correlations can be increased by manipulating the intensity mismatch of the input WCSs.

4.6 Conclusion

We presented results demonstrating fourth-order interference of mutually incoherent classical laser pulses in a 4×4 multi-core fiber beamsplitter device. We observed photon/photon interference with visibility compatible with the ideal theoretical value. As an implication of fourth-order interference in this type of multi-port device, we studied post-selected quantum

discord. We showed that the geometric discord can be maximized by controlling the intensity mismatch ratio between the input weak coherent pulses.

It has been shown that discord can be an interesting source for quantum information even when the bipartite state is separable [40, 41]. A particular Werner state is often cited as the separable Bell-diagonal state with the largest geometric discord of $\mathcal{D}_{\text{Werner}} = 1/9$ [59, 61, 75]. Curiously, we note the state produced by two-photon interference with equal intensity WCS described by our model is also separable, Bell-diagonal, and gives a larger value for geometric discord $\mathcal{D}(\gamma = 1) = 1/8$. We note that this state has been previously produced in Ref. [38] in a similar setup using fourth-order interference. As shown in this chapter, using WCS with different intensities leads to states that are no longer Bell-diagonal, resulting in an even greater geometric discord that the two examples mentioned above, achieving a maximum of $\mathcal{D}(0.435) = 0.178$. Moreover, the set of states $\rho_{AB}(\gamma \leq 0.435)$ (where incidentally the majority of our experimental data resides) are of the class described in Ref. [41], for which the geometric discord coincides with the fidelity gain in RSP protocols. Therefore, our separable state in eq. (4.11) can achieve even higher fidelities than in [41] for RSP.

Chapter 5

Four-Dimensional Bell State Measurement Device

As was mentioned in subsection 2.4.2, measurements in the maximally-entangled basis, the Bell basis, are fundamental in quantum communication protocols and quantum information processing. For photonic qubits, these Bell-state measurements (BSM) can be achieved using two-photon interference [94]. However, a complete Bell state analyzer (BSA), one that identifies all of the d^2 Bell states with 100% efficiency is impossible with linear optical devices alone, even in theory [95]. Although only a probabilistic BSM is possible, this approach is much more attractive due to the high efficiency of linear optical components, in contrast to non-linear optical processes, which have much lower success probabilities [96]. In the two-dimensional case, achieving a success probability higher than 50% [95] is impossible without auxiliary photons.

Nevertheless, ways to increase the performance of linear optical BSA have been proposed by increasing the size of the Hilbert space. One approach to discriminate all four 2×2 photonic Bell states is to use additional entanglement in an auxiliary degree of freedom of the photon pair [36, 97], which is known as hyperentanglement. Another way to increase the size of the Hilbert space is by introducing ancillary photons. It was shown that with two ancillae photons it is already possible to overcome the 1/2 limit [37, 98, 99] and was recently experimentally proven in Ref. [100].

Many quantum communication protocols can be improved by employing d-dimensional quantum systems with $d > 2$ [17]. However, performing a high-dimensional BSA (HDBSA) in a $d \times d$ Hilbert space is even more challenging than the 2×2 case. Some proposals have been presented for the realization of a HDBSA only based on linear optics components [45, 101, 102, 103], but all of them use hyperentanglement as a resource. This form of photon entanglement limits quantum teleportation since a third party cannot independently supply the input state, so it can only be generated locally.

Here we study a BSA of photonic ququarts ($d = 4$) using our high-quality 4CF-BS. We show first that two-photon interference at a pair of 4CF-BS achieves optimal discrimination of

the $d^2 = 16$ Bell states, corresponding to seven classes. We study its performance in quantum information protocols. Then, we show that a pair of entangled ancilla photons can be used to probabilistic (yet unequivocally) identify two Bell states.

5.1 Two-dimensional Standard Bell State Analyzer

For photonic BSA, the typical two-dimensional scheme is shown in Fig. 5.1. It consists of a beamsplitter (BS), two polarized beamsplitters (PBS), and detectors. The 2×2 Bell-states are commonly encoded in polarization ($|0\rangle \equiv |H\rangle$ and $|1\rangle \equiv |V\rangle$), although it can be in any other dof. Then, the inputs are

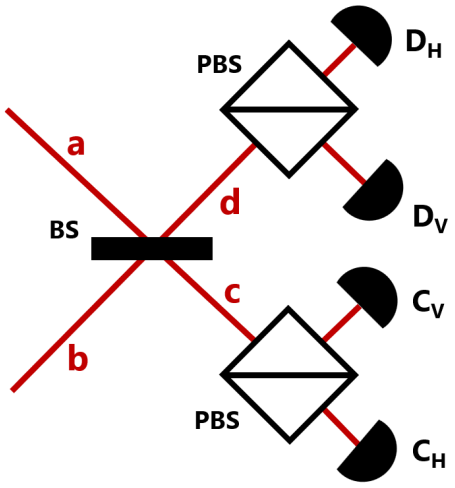

Figure 5.1: Standard Bell-State analyzer. Source: made by the author.

$$\left|\Phi^{\pm}\right\rangle = \frac{1}{\sqrt{2}}(|H\rangle_a |H\rangle_b \pm |V\rangle_a |V\rangle_b), \tag{5.1}$$

$$\left|\Psi^{\pm}\right\rangle = \frac{1}{\sqrt{2}}(|H\rangle_a |V\rangle_b \pm |V\rangle_a |H\rangle_b), \tag{5.2}$$

where a and b are the spatial modes with which they enter the BSA. Since the state $|\Psi^-\rangle$ is antisymmetric, the two photons follow different outputs of the BS, while photons in $|\Psi^+\rangle$ and $|\Phi^{\pm}\rangle$ end up in the same output [35, 36]. Then, with the PBS we separate H and V polarizations. The resulting two-photon detection events are summarized in the table 5.1. As we can see, we can fully discriminate $|\Psi^{\pm}\rangle$ states. However, the states $|\Phi^{\pm}\rangle$ cannot be uniquely identified. The total success probability of this unambiguous BSA is 50%, being the maximum that can be achieved with linear optics [95].

Input	Detection Signatures
$\|\Psi^-\rangle$	$D_H C_V, D_V C_H$
$\|\Psi^+\rangle$	$D_H D_V, C_V C_H$
$\|\Phi^\pm\rangle$	$D_H D_H, D_V D_V, C_H C_H, C_V C_V$

Table 5.1: Two-photon detection events for a standard Bell-State analyzer.

5.2 Four-dimensional Optimal Bell State Analyzer

Our main motivation in this thesis are the possible applications we can develop with the 4CF-BS, so we would like to explore how we could use it to build a HDBSA and what is the best performance we can achieve considering that in the 2-dimensional case we are only able to distinguish three groups of the four Bell-states.

As a starting point, we consider Wei *et al.* [45] work, where it was shown that for a 4×4 Hilbert space, an unambiguous Bell state discrimination is impossible and that the best we can achieve is to group the 16 Bell states into seven classes. Moreover, with the scheme designed by Kwiat and Weinfurter (KW) [97] (see Fig. 5.2), Wei *et al.* proposed an experimental BSA using hyperentangled photons.

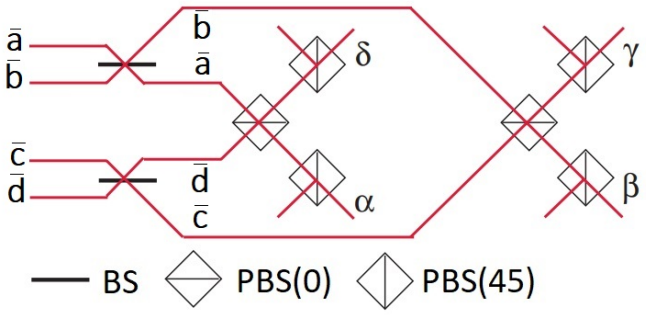

Figure 5.2: Kwiat-Weinfurter scheme for the embedded Bell-state analysis. BS: 2×2 beamsplitter, PBS(α): polarized beamsplitter rotated in α degrees. Source: taken from [45] with modifications by the author.

In Ref. [45], they start constructing the 16 Bell-like states from two photons with polarization and momentum mode degrees of freedom. The subsystem belonged to the photon A is $\{H, V\} \otimes \{\bar{a}, \bar{c}\}$ and for the photon B we have $\{H, V\} \otimes \{\bar{b}, \bar{d}\}$. The resulting states will be a combination of the four polarization, and momentum Bell states as in equation (2.10). Then,

$$\left|\Phi^\pm\right\rangle = \frac{1}{\sqrt{2}}(|H\rangle_A |H\rangle_B \pm |V\rangle_A |V\rangle_B), \qquad \left|\Psi^\pm\right\rangle = \frac{1}{\sqrt{2}}(|H\rangle_A |V\rangle_B \pm |V\rangle_A |H\rangle_B), \tag{5.3a}$$

$$\left|\phi^\pm\right\rangle = \frac{1}{\sqrt{2}}(|\bar{a}\rangle_A \left|\bar{b}\right\rangle_B \pm |\bar{c}\rangle_A \left|\bar{d}\right\rangle_B), \qquad \left|\psi^\pm\right\rangle = \frac{1}{\sqrt{2}}(|\bar{a}\rangle_A \left|\bar{d}\right\rangle_B \pm |\bar{c}\rangle_A \left|\bar{b}\right\rangle_B). \tag{5.3b}$$

Since our goal is to use the 4CF-BS to achieve this optimal HDBSA, we must only translate the polarization and momentum modes to momentum modes. To do this, we relabel the input modes to eliminate the polarization dof and use only path dof. We note that the polarization dof can be mapped to spatial mode dof using a polarizing beam splitter or similar devices, so

our approach has no loss of generality. Thus, each combination of path mode and polarization mode will represent a unique momentum mode in our system, such as

$$|0\rangle_A \equiv |H\rangle \otimes |\bar{\mathrm{a}}\rangle\,, \qquad |0\rangle_B \equiv |H\rangle \otimes |\bar{\mathrm{b}}\rangle\,, \tag{5.4a}$$

$$|1\rangle_A \equiv |V\rangle \otimes |\bar{\mathrm{a}}\rangle\,, \qquad |1\rangle_B \equiv |V\rangle \otimes |\bar{\mathrm{b}}\rangle\,, \tag{5.4b}$$

$$|2\rangle_A \equiv |H\rangle \otimes |\bar{\mathrm{c}}\rangle\,, \qquad |2\rangle_B \equiv |H\rangle \otimes |\bar{\mathrm{d}}\rangle\,, \tag{5.4c}$$

$$|3\rangle_A \equiv |V\rangle \otimes |\bar{\mathrm{c}}\rangle\,, \qquad |3\rangle_B \equiv |V\rangle \otimes |\bar{\mathrm{d}}\rangle\,. \tag{5.4d}$$

Here the kets $|j\rangle_C$ with $j = 0, 1, 2, 3$ and $C = A, B$ represents the photon C in the j-mode, implying that in the rest of the path modes we only have vacuum. For example, the state $|1\rangle_A$ represents the photon A in momentum mode 1. We can also express the states (5.4) with the creation operator $|j\rangle_A = a_j^\dagger |0\rangle$ for the photon in the subspace A and $|j\rangle_B = b_j^\dagger |0\rangle$ for the photon in the subspace B.

As an example, let us write the following state in momentum and polarization dof

$$\begin{aligned} |\Psi^+\rangle|\psi^+\rangle &= \frac{1}{\sqrt{2}}(|H\rangle_A |V\rangle_B + |V\rangle_A |H\rangle_B)\frac{1}{\sqrt{2}}(|\bar{\mathrm{a}}\rangle_A |\bar{\mathrm{d}}\rangle_B + |\bar{\mathrm{c}}\rangle_A |\bar{\mathrm{b}}\rangle_B) \\ &= \frac{1}{2}(|H\bar{\mathrm{a}}\rangle |V\bar{\mathrm{d}}\rangle + |V\bar{\mathrm{a}}\rangle |H\bar{\mathrm{d}}\rangle + |H\bar{\mathrm{c}}\rangle |V\bar{\mathrm{b}}\rangle + |V\bar{\mathrm{c}}\rangle |H\bar{\mathrm{b}}\rangle). \end{aligned} \tag{5.5}$$

Then, with our notation, the state becomes in

$$|\Psi^+\rangle|\psi^+\rangle = \frac{1}{2}(|0\rangle_A |3\rangle_B + |1\rangle_A |2\rangle_B + |2\rangle_A |1\rangle_B + |3\rangle_A |0\rangle_B) \tag{5.6}$$

$$= \frac{1}{2}(a_0^\dagger b_3^\dagger + a_1^\dagger b_2^\dagger + a_2^\dagger b_1^\dagger + a_3^\dagger b_0^\dagger)\,|vac\rangle\,. \tag{5.7}$$

where $|vac\rangle$ is the vacuum state.

The next step to build our optimal fiber-based BSA is to know the evolution of the KW scheme according to equation (3.12), and hence we must find the unitary matrix that describes it. Here the input and output creation operators are represented by the vector $\vec{v}$ that is equal to

$$(\vec{v})_{\text{in/out}} = \begin{pmatrix} a_0^\dagger \\ a_1^\dagger \\ b_0^\dagger \\ b_1^\dagger \\ a_2^\dagger \\ a_3^\dagger \\ b_2^\dagger \\ b_3^\dagger \end{pmatrix}. \tag{5.8}$$

The first elements in the KW scheme are two beamsplitters (see Fig. 5.2). Since BSs preserve polarization, we can write each one as two BSs in parallel acting on subspaces for each polarization state (H or V). Horizontal polarization passes through one BS and vertical polarization across

the other. The creation operators that represent this action transform as follows

$$a_j^\dagger \to \frac{1}{\sqrt{2}}(b_j^\dagger - \hat{b}_j^\dagger), \tag{5.9}$$

$$\hat{b}_j^\dagger \to \frac{1}{\sqrt{2}}(a_j^\dagger + \hat{b}_j^\dagger). \tag{5.10}$$

Then, the unitary matrix for the BS system acting on (5.8) looks like

$$\mathrm{BS} = \frac{1}{\sqrt{2}} \begin{bmatrix} 1 & 0 & 1 & 0 & 0 & 0 & 0 & 0 \\ 0 & 1 & 0 & 1 & 0 & 0 & 0 & 0 \\ -1 & 0 & 1 & 0 & 0 & 0 & 0 & 0 \\ 0 & -1 & 0 & 1 & 0 & 0 & 0 & 0 \\ 0 & 0 & 0 & 0 & 1 & 0 & 1 & 0 \\ 0 & 0 & 0 & 0 & 0 & 1 & 0 & 1 \\ 0 & 0 & 0 & 0 & -1 & 0 & 1 & 0 \\ 0 & 0 & 0 & 0 & 0 & -1 & 0 & 1 \end{bmatrix}, \tag{5.11}$$

The next element corresponds to a PBS(0), which transmits photons with horizontal polarization and reflects photons vertically oriented. As seen from equations (5.4), the even modes are horizontally polarized, so they remain unchanged. On the other hand, the odd modes are vertically polarized, so they transform as

$$b_j^\dagger \to a_{j\uplus 2}^\dagger \tag{5.12}$$

$$a_j^\dagger \to b_{j\uplus 2}^\dagger \tag{5.13}$$

where $\uplus$ indicates the sum modulo 4. Then, the unitary matrix that describes the PBS(0) is

$$\mathrm{PBS}(0) = \begin{bmatrix} 1 & 0 & 0 & 0 & 0 & 0 & 0 & 0 \\ 0 & 0 & 0 & 0 & 0 & 0 & 0 & 1 \\ 0 & 0 & 1 & 0 & 0 & 0 & 0 & 0 \\ 0 & 0 & 0 & 0 & 0 & 1 & 0 & 0 \\ 0 & 0 & 0 & 0 & 1 & 0 & 0 & 0 \\ 0 & 0 & 0 & 1 & 0 & 0 & 0 & 0 \\ 0 & 0 & 0 & 0 & 0 & 0 & 1 & 0 \\ 0 & 1 & 0 & 0 & 0 & 0 & 0 & 0 \end{bmatrix}. \tag{5.14}$$

The last component in the KW scheme is a PBS(45), which is equivalent to having a half-wave plate (HWP) rotated by 22.5° degrees, followed by a PBS(0). Note that the HWP(22.5) behaves (in the polarization dof) as a BS in path representation, so for even modes, the creation operators transform as

$$c_j^\dagger = \frac{1}{\sqrt{2}}(c_j^\dagger - c_{j+1}^\dagger), \tag{5.15}$$

and for odd modes as

$$c_j^\dagger = \frac{1}{\sqrt{2}}(c_j^\dagger + c_{j-1}^\dagger), \tag{5.16}$$

where $c = a, b$. In this way, the unitary matrix for the half-wave plate is the following

$$\mathrm{HWP}(22.5) = \frac{1}{\sqrt{2}} \begin{bmatrix} 1 & 1 & 0 & 0 & 0 & 0 & 0 & 0 \\ -1 & 1 & 0 & 0 & 0 & 0 & 0 & 0 \\ 0 & 0 & 1 & 1 & 0 & 0 & 0 & 0 \\ 0 & 0 & -1 & 1 & 0 & 0 & 0 & 0 \\ 0 & 0 & 0 & 0 & 1 & 1 & 0 & 0 \\ 0 & 0 & 0 & 0 & -1 & 1 & 0 & 0 \\ 0 & 0 & 0 & 0 & 0 & 0 & 1 & 1 \\ 0 & 0 & 0 & 0 & 0 & 0 & -1 & 1 \end{bmatrix}. \tag{5.17}$$

We ignore the last PBS(0) since it is used just for measurement. Thus, multiplying all this together, we can find the unitary of the system that will give us the evolution only in momentum dof

$$U_{KW} = \frac{1}{2} \begin{bmatrix} 1 & 0 & 1 & 0 & 0 & -1 & 0 & 1 \\ -1 & 0 & -1 & 0 & 0 & -1 & 0 & 1 \\ -1 & 0 & 1 & 0 & 0 & 1 & 0 & 1 \\ 1 & 0 & -1 & 0 & 0 & 1 & 0 & 1 \\ 0 & -1 & 0 & 1 & 1 & 0 & 1 & 0 \\ 0 & -1 & 0 & 1 & -1 & 0 & -1 & 0 \\ 0 & 1 & 0 & 1 & -1 & 0 & 1 & 0 \\ 0 & 1 & 0 & 1 & 1 & 0 & -1 & 0 \end{bmatrix}. \tag{5.18}$$

Now that we know the evolution of the KW scheme, the next challenge to obtain our optimal fiber-based BSA is to reconstruct the matrix (5.18) using fiber components exclusively. For this, we use the scheme shown in Fig. 5.3 which in principle is only composed of two 4CF-BS in parallel with the following unitary matrix

$$\mathrm{BS}_{\mathrm{MCF}} = \frac{1}{2} \begin{bmatrix} 1 & 1 & 0 & 0 & 1 & 1 & 0 & 0 \\ 1 & 1 & 0 & 0 & -1 & -1 & 0 & 0 \\ 0 & 0 & 1 & 1 & 0 & 0 & 1 & 1 \\ 0 & 0 & 1 & 1 & 0 & 0 & -1 & -1 \\ 1 & -1 & 0 & 0 & 1 & -1 & 0 & 0 \\ 1 & -1 & 0 & 0 & -1 & 1 & 0 & 0 \\ 0 & 0 & 1 & -1 & 0 & 0 & 1 & -1 \\ 0 & 0 & 1 & -1 & 0 & 0 & -1 & 1 \end{bmatrix}. \tag{5.19}$$

This matrix is obtained by calculating the tensor product $(B_4)_A \otimes (B_4)_B$ and then rearranging the modes to act on the vector (5.8).

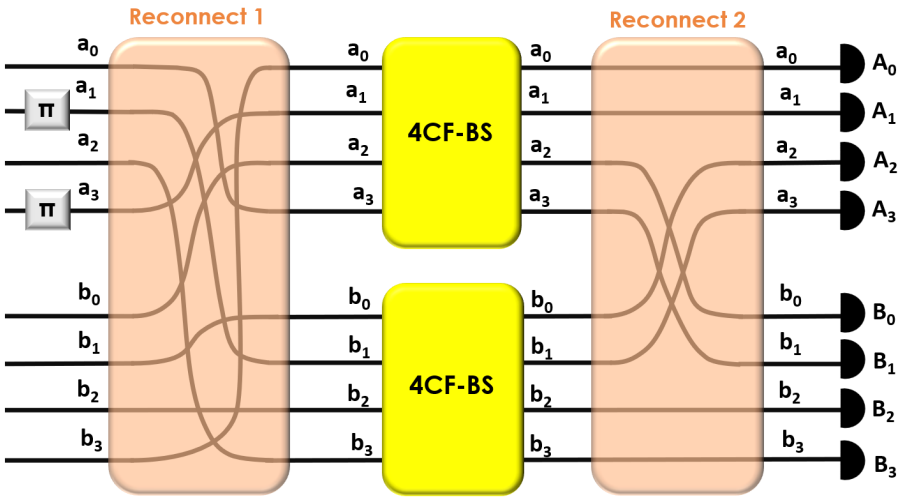

Figure 5.3: Scheme for Bell-state Measurement in dimension 4×4. On the left, we apply a π phase on the modes $|3\rangle_A$ and $|1\rangle_A$. Then, we reconnect the fibers, which we describe using the operation "reconnect 1". Next, we let act two 4MCF-BS, and finally, we swap the fibers again as shown on "reconnect 2". At the end of the setup the photons in the modes $a_j^\dagger$ will be collected by the detectors A_j and the photons in the modes $b_j^\dagger$ will reach the detectors B_j. Source: Made by the author.

In order to get (5.18) and not modify both 4CF-BS, we reconnect the fibers into different modes before and after the $\mathrm{BS}_{\mathrm{MCF}}$. In the laboratory, this is done by simply connecting the fibers correctly. While mathematically, we could relabel the modes according to the connections. However, a more transparent way of representing these connections is by writing the corresponding unitary matrices that describe them

$$R_1 = \begin{bmatrix} 0 & 0 & 0 & 0 & 0 & 0 & 0 & 1 \\ 0 & 0 & 0 & 0 & 0 & 1 & 0 & 0 \\ 0 & 0 & 0 & 1 & 0 & 0 & 0 & 0 \\ 0 & 1 & 0 & 0 & 0 & 0 & 0 & 0 \\ 0 & 0 & 1 & 0 & 0 & 0 & 0 & 0 \\ 1 & 0 & 0 & 0 & 0 & 0 & 0 & 0 \\ 0 & 0 & 0 & 0 & 0 & 0 & 1 & 0 \\ 0 & 0 & 0 & 0 & 1 & 0 & 0 & 0 \end{bmatrix}, \quad R_2 = \begin{bmatrix} 1 & 0 & 0 & 0 & 0 & 0 & 0 & 0 \\ 0 & 1 & 0 & 0 & 0 & 0 & 0 & 0 \\ 0 & 0 & 0 & 0 & 1 & 0 & 0 & 0 \\ 0 & 0 & 0 & 0 & 0 & 1 & 0 & 0 \\ 0 & 0 & 1 & 0 & 0 & 0 & 0 & 0 \\ 0 & 0 & 0 & 1 & 0 & 0 & 0 & 0 \\ 0 & 0 & 0 & 0 & 0 & 0 & 1 & 0 \\ 0 & 0 & 0 & 0 & 0 & 0 & 0 & 1 \end{bmatrix}. \tag{5.20}$$

Finally, a π-phase is also applied in the modes $|1\rangle_A$ and $|3\rangle_A$ at the beginning of the setup to exactly get (5.18). Even so, this element can be omitted since the phase of the output state does not really matter to us, we only care about where the photon was detected.

Thus, multiplying this array of matrices in the order shown in Figure 5.3, we will obtain our optimal fiber-based HDBSA.

5.2.1 Classifying the Bell States

For the classification of the 16 Bell states, the evolution of the system was needed, in order to write the output state as a function of the output creation operators

$$\vec{v}_{\text{out}} = U_{KW}\vec{v}_{\text{in}}. \tag{5.21}$$

where the vector $\vec{v}$ is described in eq. (5.8). As illustrated in Fig. 5.3, the states with modes $a_j^\dagger$ will "click" on the detectors A_j and the states in the modes $b_j^\dagger$ will "click" on the detectors B_j. Thus, by looking at the output two-photon states, we will see that some of the output states end up in the same group of detectors, and when this happens, we classify these states in the same class. We did the calculation for the 16 Bell states and then analyzed the output states with a PYTHON program (see Appendix A4), finding that indeed the states are grouped into seven distinct classes as is summarized in Table 5.2.

To be more illustrative, let's take as an example the state in (5.7) as input. For the first term in the superposition the creation operators transform as

$$a_0^\dagger \to \frac{1}{2}(a_0^\dagger - a_1^\dagger - b_0^\dagger + b_1^\dagger) \tag{5.22}$$

$$b_3^\dagger \to \frac{1}{2}(a_0^\dagger + a_1^\dagger + b_0^\dagger + b_1^\dagger) \tag{5.23}$$

If we calculate the evolution of the remaining terms and multiply them in the corresponding order, we obtain the output state

$$(\left|\Psi^+\right\rangle \left|\psi^+\right\rangle)_{\text{out}} = \frac{1}{4}(a_0^\dagger b_1^\dagger - a_1^\dagger b_0^\dagger + a_2^\dagger b_3^\dagger - a_3^\dagger b_2^\dagger)\left|vac\right\rangle. \tag{5.24}$$

Repeating the above procedure for the other states, we will find that there is another unique state that has the same contributions, but with different signs

$$(\left|\Psi^-\right\rangle \left|\psi^-\right\rangle)_{\text{out}} = \frac{1}{4}(a_0^\dagger b_1^\dagger - a_1^\dagger b_0^\dagger - a_2^\dagger b_3^\dagger + a_3^\dagger b_2^\dagger)\left|vac\right\rangle. \tag{5.25}$$

Therefore, both states will form a class that we will identify as 3. In addition and for the sake of completeness, we explicitly write down the input states classified according to the detection patterns (see Table 5.2)

Class 1

$$|\Psi^+\rangle|\psi^-\rangle = \frac{1}{2}(|0\rangle_A|3\rangle_B + |1\rangle_A|2\rangle_B - |2\rangle_A|1\rangle_B - |3\rangle_A|0\rangle_B), \tag{5.26a}$$

$$|\Psi^-\rangle|\psi^+\rangle = \frac{1}{2}(|0\rangle_A|3\rangle_B - |1\rangle_A|2\rangle_B + |2\rangle_A|1\rangle_B - |3\rangle_A|0\rangle_B), \tag{5.26b}$$

$$|\Phi^+\rangle|\phi^-\rangle = \frac{1}{2}(|0\rangle_A|0\rangle_A + |1\rangle_A|1\rangle_B - |2\rangle_A|2\rangle_B - |3\rangle_A|3\rangle_B), \tag{5.26c}$$

$$|\Phi^-\rangle|\phi^+\rangle = \frac{1}{2}(|0\rangle_A|0\rangle_B - |1\rangle_A|1\rangle_B + |2\rangle_A|2\rangle_B - |3\rangle_A|3\rangle_B). \tag{5.26d}$$

Class	Input	Detections Signatures
1	$\|\Psi^+\rangle\|\psi^-\rangle$, $\|\Psi^-\rangle\|\psi^+\rangle$	$A_0A_0, A_1A_1, A_2A_2, A_3A_3$
	$\|\Phi^+\rangle\|\phi^-\rangle$, $\|\Phi^-\rangle\|\phi^+\rangle$	$B_0B_0, B_1B_1, B_2B_2, B_3B_3$
2	$\|\Phi^+\rangle\|\phi^+\rangle$, $\|\Phi^-\rangle\|\phi^-\rangle$	$A_0A_1, A_2A_3, B_0B_1, B_2B_3$
3	$\|\Psi^+\rangle\|\psi^+\rangle$, $\|\Psi^-\rangle\|\psi^-\rangle$	$A_0B_1, A_1B_0, A_2B_3, A_3B_2$
4	$\|\Psi^+\rangle\|\phi^-\rangle$, $\|\Phi^+\rangle\|\psi^-\rangle$	$A_0B_2, A_1B_3, A_2B_0, A_3B_1$
5	$\|\Psi^-\rangle\|\phi^+\rangle$, $\|\Phi^-\rangle\|\psi^+\rangle$	$A_0A_2, A_1A_3, B_0B_2, B_1B_3$
6	$\|\Psi^+\rangle\|\phi^+\rangle$, $\|\Phi^-\rangle\|\psi^-\rangle$	$A_0B_3, A_1B_2, A_2B_1, A_3B_0$
7	$\|\Psi^-\rangle\|\phi^-\rangle$, $\|\Phi^+\rangle\|\psi^+\rangle$	$A_0A_3, A_1A_2, B_0B_3, B_1B_2$

Table 5.2: Two-photon detection pattern for high-dimension Bell state measurement.

Class 2

$$|\Phi^+\rangle|\phi^+\rangle = \frac{1}{2}(|0\rangle_A|0\rangle_B + |1\rangle_A|1\rangle_B + |2\rangle_A|2\rangle_B + |3\rangle_A|3\rangle_B), \tag{5.27a}$$

$$|\Phi^-\rangle|\phi^-\rangle = \frac{1}{2}(|0\rangle_A|0\rangle_B - |1\rangle_A|1\rangle_B - |2\rangle_A|2\rangle_B + |3\rangle_A|3\rangle_B). \tag{5.27b}$$

Class 3

$$|\Psi^+\rangle|\psi^+\rangle = \frac{1}{2}(|0\rangle_A|3\rangle_B + |1\rangle_A|2\rangle_B + |2\rangle_A|1\rangle_B + |3\rangle_A|0\rangle_B), \tag{5.28a}$$

$$|\Psi^-\rangle|\psi^-\rangle = \frac{1}{2}(|0\rangle_A|3\rangle_B - |1\rangle_A|2\rangle_B - |2\rangle_A|1\rangle_B + |3\rangle_A|0\rangle_B). \tag{5.28b}$$

Class 4

$$|\Psi^+\rangle|\phi^-\rangle = \frac{1}{2}(|0\rangle_A|1\rangle_B + |1\rangle_A|0\rangle_B - |2\rangle_A|3\rangle_B - |3\rangle_A|2\rangle_B), \tag{5.29a}$$

$$|\Phi^+\rangle|\psi^-\rangle = \frac{1}{2}(|0\rangle_A|2\rangle_B + |1\rangle_A|3\rangle_B - |2\rangle_A|0\rangle_B - |3\rangle_A|1\rangle_B). \tag{5.29b}$$

Class 5

$$|\Psi^-\rangle|\phi^+\rangle = \frac{1}{2}(|0\rangle_A|1\rangle_B - |1\rangle_A|0\rangle_B + |2\rangle_A|3\rangle_B - |3\rangle_A|2\rangle_B), \tag{5.30a}$$

$$|\Phi^-\rangle|\psi^+\rangle = \frac{1}{2}(|0\rangle_A|2\rangle_B - |1\rangle_A|3\rangle_B + |2\rangle_A|0\rangle_B - |3\rangle_A|1\rangle_B). \tag{5.30b}$$

Class 6

$$|\Psi^+\rangle|\phi^+\rangle = \frac{1}{2}(|0\rangle_A|1\rangle_A + |1\rangle_B|0\rangle_B + |2\rangle_A|3\rangle_B + |3\rangle_A|2\rangle_B) \tag{5.31a}$$

$$|\Phi^-\rangle|\psi^-\rangle = \frac{1}{2}(|0\rangle_A|2\rangle_B - |1\rangle_A|3\rangle_B - |2\rangle_A|0\rangle_B + |3\rangle_A|1\rangle_B) \tag{5.31b}$$

Class 7

$$|\Psi^-\rangle|\phi^-\rangle = \frac{1}{2}(|0\rangle_A|1\rangle_B - |1\rangle_A|0\rangle_B - |2\rangle_A|3\rangle_B + |3\rangle_A|2\rangle_B), \tag{5.32a}$$

$$|\Phi^+\rangle|\psi^+\rangle = \frac{1}{2}(|0\rangle_A|2\rangle_B + |1\rangle_A|3\rangle_B + |2\rangle_A|0\rangle_B + |3\rangle_A|1\rangle_B). \tag{5.32b}$$

Let us note that our classification of Bell states is different from that obtained in [45]. This is due to the change of variables and the reordering of modes. Moreover, there are $\binom{16}{7} = 11490$ ways to group the 16 Bell states, therefore, it is possible to have different classifications for a 4×4 BSA.

5.3 Applications in Quantum Communication

In this chapter, we will discuss the performance of our fiber-based HDBSA in different protocols for quantum communication, but first, it will be useful to define the projectors from the previously identified classes. Note that each projective measure will be written as a sum of two orthogonal projectors of rank one in a 4×4 subspace, except for class 1 which is a sum of four orthogonal projectors of rank one. Let's begin with class 2 in (5.27), such as

$$\begin{aligned} P_2 &= \left|\Phi^+\right\rangle\left|\phi^+\right\rangle\left\langle\Phi^+\right|\left\langle\phi^+\right| + \left|\Phi^-\right\rangle\left|\phi^-\right\rangle\left\langle\Phi^-\right|\left\langle\phi^-\right| \\ &= \left|\Phi^+\right\rangle_{03}\left\langle\Phi^+\right|_{03} + \left|\Phi^+\right\rangle_{12}\left\langle\Phi^+\right|_{12}, \end{aligned} \tag{5.33}$$

where the subscripts indicate the modes that are involved for photons A and B, respectively. For example, the first term in (5.33) is the projector of the following 2×2 Bell state

$$\left|\Phi^+\right\rangle_{03} = \frac{1}{\sqrt{2}}(|0\rangle_A|0\rangle_B + |3\rangle_A|3\rangle_B). \tag{5.34}$$

For class 3, we obtain something similar, such that

$$\begin{aligned} P_3 &= \left|\Psi^+\right\rangle\left|\psi^+\right\rangle\left\langle\Psi^+\right|\left\langle\psi^+\right| + \left|\Psi^-\right\rangle\left|\psi^-\right\rangle\left\langle\Psi^-\right|\left\langle\psi^-\right| \\ &= \left|\Psi^+\right\rangle_{03}\left\langle\Psi^+\right|_{03} + \left|\Psi^+\right\rangle_{12}\left\langle\Psi^+\right|_{12}. \end{aligned} \tag{5.35}$$

As we can see from (5.33) and (5.35), the measurement operators can be reduced to a sum of two orthogonal projectors of rank one in a 2×2 subspace, so P_2 and P_3 remain as projectors of rank two. Similarly, we have that the projector of the states in class 1 is reduced, in turn, to a sum of four orthogonal projectors of rank one

$$P_1 = (\left|\Phi^-\right\rangle\left\langle\Phi^-\right| + \left|\Psi^-\right\rangle\left\langle\Psi^-\right|)_{03} + (\left|\Phi^-\right\rangle\left\langle\Phi^-\right| + \left|\Psi^-\right\rangle\left\langle\Psi^-\right|)_{12}, \tag{5.36}$$

so P_1 remains as a projector of rank four. We cannot completely simplify the measurement operators for all the other classes as 2×2 Bell-states projectors. For example, in the case of the

class 5 we have

$$
\begin{aligned}
P_5 &= \left|\Psi^-\right\rangle\left|\phi^+\right\rangle\left\langle\Psi^-\right|\left\langle\phi^+\right| + \left|\Phi^-\right\rangle\left|\psi^+\right\rangle\left\langle\Phi^-\right|\left\langle\psi^+\right| \\
&= \frac{1}{2}\Big[\left|\Psi^-\right\rangle_{01}\left\langle\Psi^-\right|_{01} + \left|\Psi^-\right\rangle_{23}\left\langle\Psi^-\right|_{23} + \left|\Psi^+\right\rangle_{02}\left\langle\Psi^+\right|_{02} + \left|\Psi^+\right\rangle_{13}\left\langle\Psi^+\right|_{13} \\
&+ \frac{1}{2}(|01\rangle\langle 23| - |01\rangle\langle 32| - |10\rangle\langle 23| + |10\rangle\langle 32| + |23\rangle\langle 01| - |23\rangle\langle 10| - |32\rangle\langle 01| \\
&+ |32\rangle\langle 10| - |02\rangle\langle 13| - |02\rangle\langle 31| - |13\rangle\langle 02| - |13\rangle\langle 20| - |20\rangle\langle 13| - |20\rangle\langle 31| \\
&- |31\rangle\langle 02| - |31\rangle\langle 20|)\Big].
\end{aligned} \tag{5.37}
$$

Thus, the projective measurements of the states from classes 5 to 7 are kept as a rank two projector in a 4×4 subspace.

5.3.1 Teleportation

Quantum teleportation is one of the most essential protocols in quantum information, and it is fundamental for developing many quantum technologies [104]. In this protocol, an unknown state is transferred from one system to another at a distance [92]. A general scheme is shown in Fig. 5.4 to illustrate how the protocol is implemented. We have two spatially separated parties, Alice and Bob, who share a two-photon Bell state. In principle, as long as both parties share this entangled state, the distance between them can be arbitrarily large. A third party, say Charlie, provides Alice with the arbitrary unknown state which will be teleported to Bob. Then, she performs a BSM on her two photons and classically communicates the measurement result to Bob. Depending on the classical information that Bob receives, he applies a local unitary operator on his photon. This allows Bob to reconstruct the state provided by Charlie but now encoded on his photon.

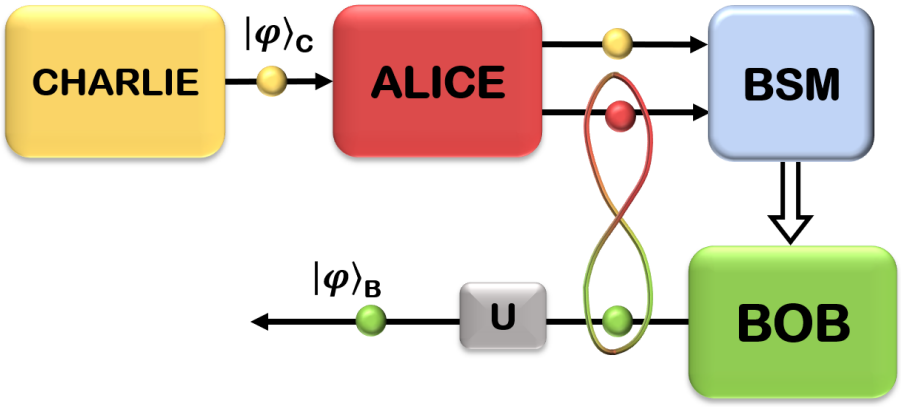

Figure 5.4: General scheme to illustrate quantum teleportation protocol. Alice and Bob share a two-photon Bell state. Charlie provides Alice with an arbitrary unknown state $|\varphi\rangle$, which will be teleported to Bob. She performs a Bell state measurement on her two photons and classically communicates the outcome to Bob. Depending on the classical information that Bob receives, he applies a local unitary on his photon. This allows Bob to reconstruct the state $|\varphi\rangle$, but now encoded on his photon. Source: Made by the author.

In our teleportation scheme, Alice has the state $|\varphi\rangle_C = \alpha|0\rangle + \beta|1\rangle + \gamma|2\rangle + \delta|3\rangle$ that will be teleported to Bob. The density matrix for this state is

$$\rho_C = \begin{pmatrix} |\alpha|^2 & \alpha\beta^* & \alpha\gamma^* & \alpha\delta^* \\ \beta\alpha^* & |\beta|^2 & \beta\gamma^* & \beta\delta^* \\ \gamma\alpha^* & \gamma\beta^* & |\gamma|^2 & \gamma\delta^* \\ \delta\alpha^* & \delta\beta^* & \delta\gamma^* & |\delta|^2 \end{pmatrix}, \tag{5.38}$$

where $\alpha, \beta, \gamma, \delta \in \mathbb{C}$. We will assume the quantum state above and the states below are normalized. We will consider normalization in the programs in Appendix A.

In our version of the protocol, we will use the projective measurements given by our optimal fiber-based HDBSA on Alice's subsystem and the state $|\varphi\rangle_C$ that we want to teleport. To study the efficiency of the measurements, we implemented the protocol with Alice and Bob sharing different types of entangled states. We compare each case by the amount of information Bob receives at the end of the teleportation. So considering that Bob does not need to apply any unitary on his photon, the state of Bob at the end of the protocol is

$$\rho_B = \mathrm{tr}_{AC}\{\Pi\,|\mathcal{AB}\rangle\,|\varphi\rangle\,\langle\mathcal{AB}|\,\langle\varphi|\}, \tag{5.39}$$

where the ket $|\mathcal{AB}\rangle$ is the state shared by Alice and Bob, and Π is a projective measurement made by our HDBSA

One way to measure how much information Bob has is through the fidelity (see section 2.5) between the state $|\varphi\rangle_C$ and ρ_B. Since the state in the C partition is pure, we can write the fidelity using the expressión in eq. (2.29), i.e, $F(\rho_B) = \langle\varphi|\,\rho_B\,|\varphi\rangle$. Note that in the ideal case, the fidelity should be one.

i) 4×4 Identity Matrix

This is the simplest case and corresponds to when Alice does nothing. Therefore, Bob's state is the 4×4 identity matrix $I_4 = (|0\rangle\langle 0| + |1\rangle\langle 1| + |2\rangle\langle 2| + |3\rangle\langle 3|)/4$, since nothing have been done over his subsystem. Then, we have

$$F(I_4, |\varphi\rangle) = \langle\varphi|\,I_4\,|\varphi\rangle = 0.25 \tag{5.40}$$

The motivation for writing this case is merely to use it as a reference.

ii) Classical Correlation

Let us continue by considering that Alice and Bob share a classically correlated state of the form

$$\rho_{AB} = \frac{1}{4}(|00\rangle\,\langle 00| + |11\rangle\,\langle 11| + |22\rangle\,\langle 22| + |33\rangle\,\langle 33|) \tag{5.41}$$

The state of the whole system is of the form

$$\rho_{ABC} = \rho_{AB} \otimes |\varphi\rangle\,\langle\varphi|\,. \tag{5.42}$$

We will use an ideal projective measurement $\Pi_{AC} = |\Phi^+\rangle\,\langle\Phi^+|$ in a four-dimensional

subspace for Alice's photons. Then the reduced density matrix of Bob is equal to

$$\rho_B^{(2)} = \mathrm{tr}_{AC}\{P_2(\rho_{AB} \otimes |\varphi\rangle \langle\varphi|)\}. \tag{5.43}$$

We evaluate this state in the definition of fidelity for pure states (see eq. (2.29)) to calculate the distance between (5.38). Then, the general expression for fidelity is written as

$$F(\rho_B^{(2)}, |\varphi\rangle) = (|\alpha|^4 + |\beta|^4 + |\gamma|^4 + |\delta|^4). \tag{5.44}$$

Since the state to teleport has to be arbitrary, we need to evaluate the performance of our HDBSA for all possible state superpositions in the general form of $|\varphi\rangle_C$. For this purpose, we use the MUBS for $d = 4$ presented in section 2.3.2, given that we can reconstruct any density matrix with these bases [46].
Once the general expression for fidelity has been found, we use all the vectors defining the MUBS to evaluate the fidelity. This calculation is done with a PYTHON program (see Appendix A5) where we replace the vector $(\alpha, \beta, \gamma, \delta)$, that characterizes the state $|\varphi\rangle_C$, by the vectors that define the MUBS (see eq. (2.19)). Finally, we average between all possible outcomes, obtaining the total fidelity.

In the case of (5.44), we have that the mean fidelity is

$$F_{\mathrm{cl}}^{(2)} = \frac{1}{20}(1 \times 4 + 0.25 \times 16) = 0.4 \tag{5.45}$$

This result agrees with Ref. [105], where the optimal single-copy state estimation for a ququart is predicted to be 0.4, implying that evaluating the state with the MUBS is a good approach to compute the overall fidelity.

iii) Qubit case

Here we consider that Alice and Bob share a 2-dimensional Bell state of the form

$$\left|\Phi^+\right\rangle_A \left|\Phi^+\right\rangle_B = \frac{1}{\sqrt{2}}(|00\rangle + |33\rangle). \tag{5.46}$$

Then the state describing the whole system is

$$\left|\Phi^+\right\rangle \left|\Phi^+\right\rangle |\varphi\rangle = \frac{1}{\sqrt{2}}\big[\,(\alpha|000\rangle + \beta|001\rangle + \gamma|002\rangle + \delta|003\rangle) \tag{5.47}$$

$$+ (\alpha|330\rangle + \beta|331\rangle + \gamma|332\rangle + \delta|333\rangle)\,\big]. \tag{5.48}$$

Recalling eq. (5.39) and using an ideal projective measurement $\Pi_{AC} = |\Phi^+\rangle \langle\Phi^+|$ in a 2-dimensional subspace, we have

$$\rho_{\mathrm{qubit}}^{(2)} = |\alpha|^2|0\rangle\langle 0| + \alpha^*\delta|3\rangle\langle 0| + \alpha\delta^*|0\rangle\langle 3| + |\delta|^2|3\rangle\langle 3|, \tag{5.49}$$

To calculate the fidelity between $|\varphi\rangle_C$ and $\rho_B^{(2)}$ we use the definition (2.29), such as

$$F(\rho_B^{(2)}, |\varphi\rangle) = |\alpha|^2 + |\delta|^2. \tag{5.50}$$

This state has been already normalized. For the same argument as in the classical case, we calculate the average fidelity with the MUBS for $d = 4$, such as

$$F_{\text{qubit}}^{(2)} = \frac{1}{20}(1 \times 2 + 0.5 \times 16 + 0 \times 2) = 0.5. \tag{5.51}$$

Assuming a perfect 2×2 BSM, we expect an average fidelity of 0.5 when a maximally entangled pair of qubits is used as the quantum resource.

iv) Ququart

Finally, to fully exploit our HDBSA, we consider the case when Alice and Bob share an entangled ququart of the form

$$\left|\Phi^+\right\rangle \left|\Phi^+\right\rangle_{AB} = \frac{1}{2}(|00\rangle + |11\rangle + |22\rangle + |33\rangle). \tag{5.52}$$

Therefore, the state that describes the whole system is given by

$$\begin{aligned}\left|\Phi^+\right\rangle_A \left|\Phi^+\right\rangle_B |\varphi\rangle_C =& \frac{1}{2}[(\alpha|000\rangle + \beta|001\rangle + \gamma|002\rangle + \delta|003\rangle) \\ &+ (\alpha|110\rangle + \beta|111\rangle + \gamma|112\rangle + \delta|113\rangle) \\ &+ (\alpha|220\rangle + \beta|221\rangle + \gamma|222\rangle + \delta|223\rangle) \\ &+ (\alpha|330\rangle + \beta|331\rangle + \gamma|332\rangle + \delta|333\rangle)].\end{aligned} \tag{5.53}$$

Then, replacing the state (5.53) in (5.39) and using the projector P_2, we have that Bob's state after the teleportation is

$$\begin{aligned}\rho_B^{(2)} =& (|\alpha|^2|0\rangle\langle 0| + |\beta|^2|1\rangle\langle 1| + |\gamma|^2|2\rangle\langle 2| + |\delta|^2|3\rangle\langle 3| \\ &+ \beta\gamma^*|1\rangle\langle 2| + \beta^*\gamma|2\rangle\langle 1| + \alpha^*\delta|3\rangle\langle 0| + \alpha\delta^*|0\rangle\langle 3|) \qquad (5.54) \\ =& (\alpha|0\rangle + \delta|3\rangle)(\alpha^*\langle 0| + \delta^*\langle 3|) + (\beta|1\rangle + \gamma|2\rangle)(\beta^*\langle 1| + \gamma^*\langle 2|). \qquad (5.55)\end{aligned}$$

The fidelity can be calculated analytically, resulting in

$$F(\rho_B^{(2)}, |\varphi\rangle) = (|\alpha|^4 + |\beta|^4 + |\gamma|^4 + |\delta|^4 + 2|\beta|^2|\gamma|^2 + 2|\delta|^2|\alpha|^2). \tag{5.56}$$

Using the MUBs for $d = 4$ as in the previous cases, we have

$$F_{\text{ququart}}^{(2)} = \frac{1}{20}(0.5 \times 16 + 1 \times 4) = 0.6. \tag{5.57}$$

Our optimal HDBSA could also project Alice's states with the measurement operator P_3. When Bob receives the classic information resulting from this measurement, he needs to apply a unitary over his state to obtain the same fidelity as using the measurement

Bell state Measurement	Local Unitary
P_1	$\mathbb{I}$
P_2	$\mathbb{I}$
P_3	$X_{12}X_{03}$
P_4	$Z_2Z_3X_{01}X_{23}$
P_5	$X_{01}X_{23}Z_3Z_1$
P_6	$X_{01}X_{23}$
P_7	$X_{02}X_{13}$

Table 5.3: Correspondence between the Bell state measurement made on Alice's state and the unitary that Bob will need to apply on his system. The operator X_{mn} is the Pauli matrix that takes the state $|m\rangle$ to $|n\rangle$ with $m, n = 0, 1, 2, 3$ and Z_m is the Pauli matrix that add a π phase on the state $|m\rangle$.

operator P_2. Such as

$$\begin{aligned}\rho_B^{(3)} =& U_3(|\delta|^2|0\rangle\langle 0| + |\gamma|^2|1\rangle\langle 1| + |\beta|^2|2\rangle\langle 2| + +|\alpha|^2|3\rangle\langle 3| \\ &+ \beta^*\gamma|1\rangle\langle 2| + \beta\gamma^*|2\rangle\langle 1| + \alpha\delta^*|3\rangle\langle 0| + \alpha^*\delta|0\rangle\langle 3|)U_3^\dagger \end{aligned} \tag{5.58}$$

If we compare this density matrix with (5.54), it is clear that we must apply the unitary $U_3 = X_{12}X_{03}$, where the operator X_{mn} is the Pauli matrix that takes the state $|m\rangle$ to $|n\rangle$ with $m, n = 0, 1, 2, 3$. By calculating the fidelity for the state (5.58), we obtain exactly the expression (5.56) and therefore a value of 0.6 as average fidelity.

The correspondence between the Bell state measurement made on Alice's state and the unitary that Bob must apply to his system is summarized in table 5.3. For all the projectors the average fidelity is 0.6, except for projector P_1 where the fidelity gives a value of 0.3, with no possibility of improvement. When we look at the operators that compose the unitary in table 5.3 applied on the states of classes 2 to 7, these local operators always try to bring at least one state to the form

$$\left|\Phi^+\right\rangle \left|\Phi^+\right\rangle = \frac{1}{2}(|0\rangle_A|0\rangle_B + |1\rangle_A|1\rangle_B + |2\rangle_A|2\rangle_B + |3\rangle_A|3\rangle_B) \tag{5.59}$$

However, class 1 has already two states of this form and even if we try to change the phases so that one of the states is only positive, the fidelity will not be improved. Therefore, the overall fidelity of the scheme is

$$F_{\text{ququart}} = \frac{1}{16}(0.6 \times 12 + 0.3 \times 4) = 0.525 \tag{5.60}$$

Interestingly, the average fidelity with this imperfect 4×4 BSA is slightly larger than a perfect BSA in conjunction with 2×2 Bell states.

5.3.2 Entanglement Swapping

As briefly presented in subsection 2.4.2, entanglement swapping allows the transfer (teleportation) of entanglement between two photons belonging to two different quantum systems that have never interacted before. According to Fig. 2.1, one of the systems, called Alice, has two photons $\{A, C\}$ and the other system, called Bob, has two more $\{B, D\}$. Alice's (Bob's) photons are entangled and are described by the Bell state $|\Phi^+\rangle\,|\phi^+\rangle$. Then the whole system is

$$|\Phi^+\rangle\,\big|\phi^+\big\rangle_{AC}\,|\Phi^+\rangle\,\big|\phi^+\big\rangle_{BD} = \frac{1}{4}(|00\rangle + |11\rangle + |22\rangle + |33\rangle)_{AC}(|00\rangle + |11\rangle + |22\rangle + |33\rangle)_{BD}. \tag{5.61}$$

In addition, Alice (Bob) sends the photon C (D) to a BSM, which performs a projective measurement Π. After performing the measurement, the state is given by the following density matrix

$$\rho_{AB} = \mathrm{tr}\{\Pi(\big|\Phi^+\big\rangle\,\big|\phi^+\big\rangle_{AC}\,\big|\Phi^+\big\rangle\,\big|\phi^+\big\rangle_{BD}\,\big\langle\Phi^+\big|\,\big\langle\phi^+\big|_{AC}\,\big\langle\Phi^+\big|\,\big\langle\phi^+\big|_{BD})\}. \tag{5.62}$$

In the ideal case, the BSM makes the following projective measurement

$$\Pi_{\mathrm{id}}^{CD} = \big|\Phi^+\big\rangle\,\big|\phi^+\big\rangle_{CD}\,\big\langle\Phi^+\big|\,\big\langle\phi^+\big|_{CD}\,. \tag{5.63}$$

The resulting density matrix by performing this measurement is $\rho_{AB}^{\mathrm{id}} = |\Phi^+\rangle\,|\phi^+\rangle_{AB}\,\langle\Phi^+|\,\langle\phi^+|_{AB}$. To quantify the amount of entanglement that subsystems A and B possess after the entanglement swapping, we calculate the logarithmic negativity $LN(\rho)$ introduced in the subsection 2.6.1. Using a program in PYTHON (see Appendix A6) is easy to obtain the logarithmic negativity of the state ρ_{AB}^{id} such as $LN(\rho_{AB}^{id}) = 2$. Note that for the 2-dimensional ideal case that was previously presented in the subsection 2.4.2, the logarithmic negativity for the 2×2 Bell state $|\Phi^+\rangle$ in eq. (2.27) is equal to $LN(\rho_{AB}) = 1$. These results will be useful as a reference for what we should obtain.

We would like to know how much entanglement is shared between Alice and Bob when we perform the projective measurements presented at the beginning of this section. Let us first try with the projector P_2 in eq. (5.33). Recalling eq. (5.62), and using P_2 as a projective measurement, the density operator is equal to $\rho_{AB}^{(2)} = (|\Phi^+\rangle_{03}\,\langle\Phi^+|_{03} + |\Phi^+\rangle_{12}\,\langle\Phi^+|_{12})/\sqrt{2}$, where the super index (2) is to indicate that we are projecting with eq. (5.33). Then the logarithmic negativity is $LN(\rho^{(2)})_{AB} = 1$.

Due to the similarity between classes 2 through 7, we see that, despite the high-dimensional nature of the BSA, the best we can do in these cases is to produce entanglement that is equivalent to a maximally entangled 2×2 Bell pair.

5.3.3 Superdense Coding

Superdense coding [35] allows the transmission of $\log_2(d^2)$ bits of information by just sending one qudit. The protocol involves two parties, Alice (sender) and Bob (receiver), who share a two-photon entangled state. Since our HDBSA can only distinguish seven classes, Alice will

only be able to send $\log_2(7) \approx 2.7$ bits of information per ququart to Bob. Depending on the bits that Alice wants to send, she performs one of seven local operations on her photon to transform the state to itself or to six others. For example, if Alice and Bob share the entangled state $|\Phi^+\rangle|\phi^+\rangle$, she can apply a local operator (see subsection 2.3.1) to transform this state to $\{|\Psi^+\rangle|\psi^-\rangle, |\Psi^+\rangle|\psi^+\rangle, |\Phi^+\rangle|\psi^-\rangle, |\Psi^-\rangle|\phi^+\rangle, |\Phi^-\rangle|\psi^-\rangle, |\Phi^+\rangle|\psi^+\rangle\}$.

This case is better than when Alice and Bob share an entangled qubit. As we saw in section 2.3.1, an optical BSA can only distinguish three groups of Bell state. Therefore, Alice can only send $\log_2(3) \approx 1.58$ bits. We could try using two entangled pairs of qubits as a resource to send $2\log_2 3 \approx 3.17$ bits, which is greater than $\log_2 7 \approx 2.8$ bits. However, four-photon detection has an efficiency of η^4 in contrast to the two-photon case where the efficiency is η^2. Then we can compare the average amount of information sent:

$$\eta^4 \times 3.17 = \eta^2 \times 2.8 \Rightarrow \eta_{\text{crit}} \approx 0.94. \tag{5.64}$$

Therefore, as long as the detection efficiency is less than 94%, the single ququart pair is superior. Although our HDBSA cannot unequivocally separate the 16 Bell states, we achieved a better result for superdense coding compared with the one and two-qubit cases.

5.4 Four-dimensional Bell State Analyzer with Ancillary Photons

In the previous section, we saw that with our HDBSA we achieve an advantage in superdense coding protocol using ququarts. However, quantum teleportation and entanglement swapping, which are protocols that carry more interest in the scientific community, are very limited in terms of dimensionality. We obtain practically the same results as using qubits ($d = 2$).

At the beginning of the chapter, we mentioned some works whereby the performance of the 2×2 BSA can be improved by increasing the Hilbert space. Is it possible that by adding ancillary photons to our HDBSA, we can at least distinguish one of the 16 Bell states in a probabilistic way? While the probability of success would be low, once it works, the fidelity would be equal to one for quantum teleportation, or the quality of the entanglement we produce in the entanglement swapping protocol would be equal to the ideal case.

In this way, our goal is to probabilistic (yet unequivocally) identify a single Bell state. Therefore, to improve our HDBSA scheme we introduce two entangled ancillary photons with momentum degree of freedom: $\{e_0^\dagger, e_1^\dagger, e_2^\dagger, e_3^\dagger, f_0^\dagger, f_1^\dagger, f_2^\dagger, f_3^\dagger\}$. We want these ancillary photons to interfere with the outcomes of the original HDBSA scheme so through eight 2×2 BS as shown in Figure 5.5.

Considering that we aim to separate the states of a specific class, the strategy consists in writing the state of the ancillary photons analogously to the output state in the original HDBSA scheme, so that interference can occur. The main difference between the ancilla and the undetected photons is that we exchange $a_j^\dagger \to e_j^\dagger$ and $b_j^\dagger \to f_j^\dagger$. Therefore, we can look at the detection signatures in Table 5.2 and get an idea about the state prior to the detection. For

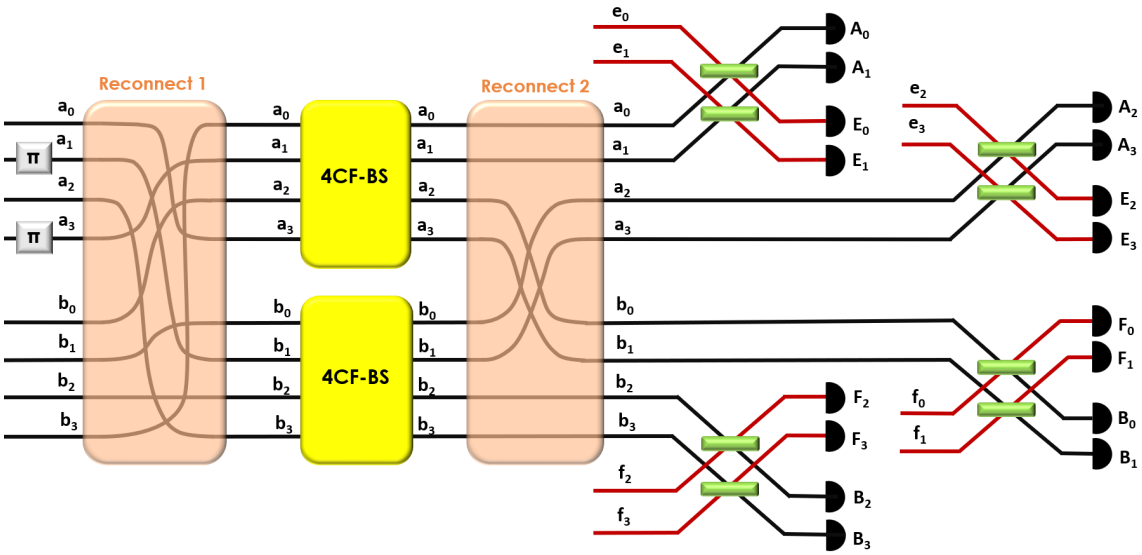

Figure 5.5: Scheme for 4×4 Bell-state measurement with ancillae. To the previous HDBSA scheme shown in Fig. 5.3, we add eight 2×2 beamsplitters represented in green rectangles, which interfere with the original outcomes. Source: Made by the author.

example, the states being detected in class 2 are of the form

$$(|\Phi^+\rangle|\phi^+\rangle)_{\text{out}} = \frac{1}{2}(-a_0^\dagger a_1^\dagger - a_2^\dagger a_3^\dagger + b_0^\dagger b_1^\dagger + b_2^\dagger b_3^\dagger)\,|vac\rangle\,, \tag{5.65}$$

$$(|\Phi^-\rangle|\phi^-\rangle)_{\text{out}} = \frac{1}{2}(-a_0^\dagger a_1^\dagger + a_2^\dagger a_3^\dagger + b_0^\dagger b_1^\dagger - b_2^\dagger b_3^\dagger)\,|vac\rangle\,. \tag{5.66}$$

Thus, the ancilla states are written as

$$|\Upsilon_2\rangle = \frac{1}{2}(e_0^\dagger e_1^\dagger + e_2^\dagger e_3^\dagger + f_0^\dagger f_1^\dagger + f_2^\dagger f_3^\dagger)\,|vac\rangle \tag{5.67}$$

Introducing this state to the new scheme in Fig. 5.5, for the first output state in class 2 we have

$$\begin{aligned}
|\Phi^+\rangle\,|\phi^+\rangle\,|\Upsilon_2\rangle \rightarrow \frac{1}{16}\Big[&\hat{a}_0^{\dagger 2}\hat{a}_1^{\dagger 2} - \hat{a}_0^{\dagger 2}\hat{e}_1^{\dagger 2} - \hat{a}_1^{\dagger 2}\hat{e}_0^{\dagger 2} + \hat{a}_2^{\dagger 2}\hat{a}_3^{\dagger 2} - \hat{a}_2^{\dagger 2}\hat{e}_3^{\dagger 2} - \hat{a}_3^{\dagger 2}\hat{e}_2^{\dagger 2} - \hat{b}_0^{\dagger 2}\hat{b}_1^{\dagger 2} + \hat{b}_0^{\dagger 2}\hat{f}_1^{\dagger 2} + \hat{b}_1^{\dagger 2}\hat{f}_0^{\dagger 2} \\
&-\hat{b}_2^{\dagger 2}\hat{b}_3^{\dagger 2} + \hat{b}_2^{\dagger 2}\hat{f}_3^{\dagger 2} + \hat{b}_3^{\dagger 2}\hat{f}_2^{\dagger 2} + \hat{e}_0^{\dagger 2}\hat{e}_1^{\dagger 2} + \hat{e}_2^{\dagger 2}\hat{e}_3^{\dagger 2} - \hat{f}_0^{\dagger 2}\hat{f}_1^{\dagger 2} - \hat{f}_2^{\dagger 2}\hat{f}_3^{\dagger 2} + 2(a_0^\dagger a_1^\dagger a_2^\dagger a_3^\dagger \\
&-a_0^\dagger a_1^\dagger b_0^\dagger f_1^\dagger + a_0^\dagger a_1^\dagger b_1^\dagger f_0^\dagger - a_0^\dagger a_1^\dagger b_2^\dagger f_3^\dagger + a_0^\dagger a_1^\dagger b_3^\dagger f_2^\dagger - a_0^\dagger a_1^\dagger e_2^\dagger e_3^\dagger - a_0^\dagger a_2^\dagger e_1^\dagger e_3^\dagger + a_0^\dagger a_3^\dagger e_1^\dagger e_2^\dagger \\
&+a_0^\dagger b_0^\dagger b_1^\dagger e_1^\dagger + a_0^\dagger b_2^\dagger b_3^\dagger e_1^\dagger - a_0^\dagger e_1^\dagger f_0^\dagger f_1^\dagger - a_0^\dagger e_1^\dagger f_2^\dagger f_3^\dagger + a_1^\dagger a_2^\dagger e_0^\dagger e_3^\dagger - a_1^\dagger a_3^\dagger e_0^\dagger e_2^\dagger - a_1^\dagger b_0^\dagger b_1^\dagger e_0^\dagger \\
&- a_1^\dagger b_2^\dagger b_3^\dagger e_0^\dagger + a_1^\dagger e_0^\dagger f_0^\dagger f_1^\dagger + a_1^\dagger e_0^\dagger f_2^\dagger f_3^\dagger - a_2^\dagger a_3^\dagger b_0^\dagger f_1^\dagger + a_2^\dagger a_3^\dagger b_1^\dagger f_0^\dagger - a_2^\dagger a_3^\dagger b_2^\dagger f_3^\dagger + a_2^\dagger a_3^\dagger b_3^\dagger f_2^\dagger \\
&- a_2^\dagger a_3^\dagger e_0^\dagger e_1^\dagger + a_2^\dagger b_0^\dagger b_1^\dagger e_3^\dagger + a_2^\dagger b_2^\dagger b_3^\dagger e_3^\dagger - a_2^\dagger e_3^\dagger f_0^\dagger f_1^\dagger - a_2^\dagger e_3^\dagger f_2^\dagger f_3^\dagger - a_3^\dagger b_0^\dagger b_1^\dagger e_2^\dagger - a_3^\dagger b_2^\dagger b_3^\dagger e_2^\dagger \\
&+ a_3^\dagger e_2^\dagger f_0^\dagger f_1^\dagger + a_3^\dagger e_2^\dagger f_2^\dagger f_3^\dagger - b_0^\dagger b_1^\dagger b_2^\dagger b_3^\dagger + b_0^\dagger b_1^\dagger f_2^\dagger f_3^\dagger + b_0^\dagger b_2^\dagger f_1^\dagger f_3^\dagger - b_0^\dagger b_3^\dagger f_1^\dagger f_2^\dagger \\
&+b_0^\dagger e_0^\dagger e_1^\dagger f_1^\dagger + b_0^\dagger e_2^\dagger e_3^\dagger f_1^\dagger - b_1^\dagger b_2^\dagger f_0^\dagger f_3^\dagger + b_1^\dagger b_3^\dagger f_0^\dagger f_2^\dagger - b_1^\dagger e_0^\dagger e_1^\dagger f_0^\dagger - b_1^\dagger e_2^\dagger e_3^\dagger f_0^\dagger + b_2^\dagger b_3^\dagger f_0^\dagger f_1^\dagger \\
&+ b_2^\dagger e_0^\dagger e_1^\dagger f_3^\dagger + b_2^\dagger e_2^\dagger e_3^\dagger f_3^\dagger - b_3^\dagger e_0^\dagger e_1^\dagger f_2^\dagger - b_3^\dagger e_2^\dagger e_3^\dagger f_2^\dagger + e_0^\dagger e_1^\dagger e_2^\dagger e_3^\dagger - f_0^\dagger f_1^\dagger f_2^\dagger f_3^\dagger)\Big]\,|0\rangle\,,
\end{aligned} \tag{5.68}$$

and for the second output state, we obtain

$$
\begin{aligned}
\left|\Phi^{-}\right\rangle\left|\phi^{-}\right\rangle\left|\Upsilon_2\right\rangle \rightarrow \frac{1}{16}[&\hat{a}_0^{\dagger 2}\hat{a}_1^{\dagger 2} - \hat{a}_0^{\dagger 2}\hat{e}_1^{\dagger 2} - \hat{a}_1^{\dagger 2}\hat{e}_0^{\dagger 2} - \hat{a}_2^{\dagger 2}\hat{a}_3^{\dagger 2} + \hat{a}_2^{\dagger 2}\hat{e}_3^{\dagger 2} + \hat{a}_3^{\dagger 2}\hat{e}_2^{\dagger 2} - \hat{b}_0^{\dagger 2}\hat{b}_1^{\dagger 2} + \hat{b}_0^{\dagger 2}\hat{f}_1^{\dagger 2} + \hat{b}_1^{\dagger 2}\hat{f}_0^{\dagger 2} \\
&+\hat{b}_2^{\dagger 2}\hat{b}_3^{\dagger 2} - \hat{b}_2^{\dagger 2}\hat{f}_3^{\dagger 2} - \hat{b}_3^{\dagger 2}\hat{f}_2^{\dagger 2} + \hat{e}_0^{\dagger 2}\hat{e}_1^{\dagger 2} - \hat{e}_2^{\dagger 2}\hat{e}_3^{\dagger 2} - \hat{f}_0^{\dagger 2}\hat{f}_1^{\dagger 2} + \hat{f}_2^{\dagger 2}\hat{f}_3^{\dagger 2} - 2(a_0^\dagger a_1^\dagger a_2^\dagger e_3^\dagger \\
&+ a_0^\dagger a_1^\dagger a_3^\dagger e_2^\dagger - a_0^\dagger a_1^\dagger b_0^\dagger f_1^\dagger + a_0^\dagger a_1^\dagger b_1^\dagger f_0^\dagger + a_0^\dagger a_1^\dagger b_2^{\dagger 2} b_3^\dagger - a_0^\dagger a_1^\dagger f_2^\dagger f_3^\dagger + a_0^\dagger a_2^\dagger a_3^\dagger e_1^\dagger + a_0^\dagger b_0^\dagger b_1^\dagger e_1^\dagger \\
&- a_0^\dagger b_2^\dagger e_1^\dagger f_3^\dagger + a_0^\dagger b_3^\dagger e_1^\dagger f_2^\dagger - a_0^\dagger e_1^\dagger e_2^\dagger e_3^\dagger - a_0^\dagger e_1^\dagger f_0^\dagger f_1^\dagger - a_1^\dagger a_2^\dagger a_3^\dagger e_0^\dagger - a_1^\dagger b_0^\dagger b_1^\dagger e_0^\dagger + a_1^\dagger b_2^\dagger e_0^\dagger f_3^\dagger \\
&- a_1^\dagger b_3^\dagger e_0^\dagger f_2^\dagger + a_1^\dagger e_0^\dagger e_2^\dagger e_3^\dagger + a_1^\dagger e_0^\dagger f_0^\dagger f_1^\dagger - a_2^\dagger a_3^\dagger b_0^\dagger b_1^\dagger + a_2^\dagger a_3^\dagger b_2^\dagger f_3^\dagger - a_2^\dagger a_3^\dagger b_3^\dagger f_2^\dagger + a_2^\dagger a_3^\dagger f_0^\dagger f_1^\dagger \\
&+ a_2^\dagger b_0^\dagger e_3^\dagger f_1^\dagger - a_2^\dagger b_1^\dagger e_3^\dagger f_0^\dagger - a_2^\dagger b_2^\dagger b_3^\dagger e_3^\dagger + a_2^\dagger e_0^\dagger e_1^\dagger e_3^\dagger + a_2^\dagger e_3^\dagger f_2^\dagger f_3^\dagger - a_3^\dagger b_0^\dagger e_2^\dagger f_1^\dagger + a_3^\dagger b_1^\dagger e_2^\dagger f_0^\dagger \\
&+ a_3^\dagger b_2^\dagger b_3^\dagger e_2^\dagger - a_3^\dagger e_0^\dagger e_1^\dagger e_2^\dagger - a_3^\dagger e_2^\dagger f_2^\dagger f_3^\dagger + b_0^\dagger b_1^\dagger b_2^\dagger f_3^\dagger - b_0^\dagger b_1^\dagger b_3^\dagger f_2^\dagger + b_0^\dagger b_1^\dagger e_2^\dagger e_3^\dagger - b_0^\dagger b_2^\dagger b_3^\dagger f_1^\dagger \\
&+ b_0^\dagger e_0^\dagger e_1^\dagger f_1^\dagger + b_0^\dagger f_1^\dagger f_2^\dagger f_3^\dagger + b_1^\dagger b_2^\dagger b_3^\dagger f_0^\dagger - b_1^\dagger e_0^\dagger e_1^\dagger f_0^\dagger - b_1^\dagger f_0^\dagger f_2^\dagger f_3^\dagger - b_2^\dagger b_3^\dagger e_0^\dagger e_1^\dagger - b_2^\dagger e_2^\dagger e_3^\dagger f_3^\dagger \\
&- b_2^\dagger f_0^\dagger f_1^\dagger f_3^\dagger + b_3^\dagger e_2^\dagger e_3^\dagger f_2^\dagger + b_3^\dagger f_0^\dagger f_1^\dagger f_2^\dagger + e_0^\dagger e_1^\dagger f_2^\dagger f_3^\dagger - e_2^\dagger e_3^\dagger f_0^\dagger f_1^\dagger)]\left|0\right\rangle, \qquad (5.69)
\end{aligned}
$$

where the terms in red are repeated for both outcomes. We observe that the output states share half of the events, but the other half are unique for each state, which implies that we can now distinguish between these outcomes 50% of the time. However, we must also check that by introducing the ancillary photons whether the seven classes are still indistinguishable from each other and whether we can now discriminate between states of the same class, other than 2. We wrote a program in PYTHON (see Appendix A7) to settle these doubts. The heart of the code is illustrated in Fig. 5.6, where the sets represent the states and the elements represent the events before being detected. Fig. 5.6a shows the case of two states that belong to different classes. We note that the intersection of both sets is equal to vacuum since they do not have any term in common (and which makes the classes distinguishable). These cases are discarded by the program. Instead, Fig. 5.6b shows that for states belonging to the same class (excluding class 1), the intersection corresponds to half of the elements of both sets, as long as we use the correct ancilla. Then, we are able to discriminate between two states, contained in the same class, 50% of the time. In addition, with the program, we checked that the sign of the ancilla states does not alter these results.

The above translates into the overall success probability of the scheme, resulting in

$$P_{\text{succ}} = (0.5\xi_1 + 0.5\xi_2), \qquad (5.70)$$

where the variables ξ_1 and ξ_2 are the probabilities that an entangled photon source generates the Bell states that we are trying to distinguish. In the best case, the source only generates the two Bell states we are discriminating, then the success probability is $P_{\text{succ}} = 1/2$. If the source generates the 16 Bell states with equal probability, we have that $\xi_1 = \xi_2 = 1/16$, so $P_{\text{succ}} = 1/16$. Finally, in the worst case, the source does not generate the states we are discriminating against. Nevertheless, we can always avoid this case by changing the ancilla state to distinguish a Bell state that is generated by the source.

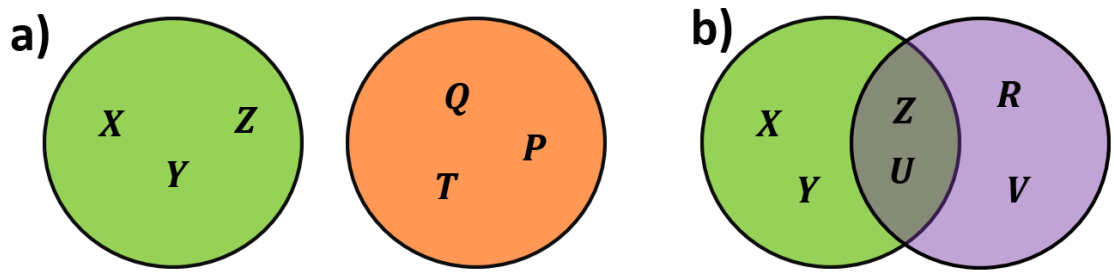

Figure 5.6: Venn diagram representing the idea of the program with which we check the distinguishability between states. Sets represent the classes, and the elements of the sets represent the events before being detected. a) For states belonging to different classes, the intersection of both sets is equal to vacuum since they do not have any term in common. These case is discarded by the program b) For states of the same class, half of the elements are repeated, but the other half are not. This result implies that we will be able to discriminate between both states 50% of the time. Source: Made by the author.

5.4.1 Aplication: Target Detection

A direct and useful application for our improved HDBSA is in quantum target detection (QTD), also known as quantum illumination. The QTD scenario has demonstrated an enhancement over its classical counterpart even when noise and loss are so great that no entanglement survives at the detector [106].

The protocol is illustrated in Fig. 5.7, where we have a source that produces a pair of photons, A and B, in some Bell state. The signal photon B is sent to an object immersed in a noisy background described by a fully mixed state $\rho_n = \mathbb{I}/d$. If the target is there, the photon will be reflected and go to the BSM. If the object is not there, the photon will be lost. On the other hand, idler photon A is isolated and sent directly to the BSM.

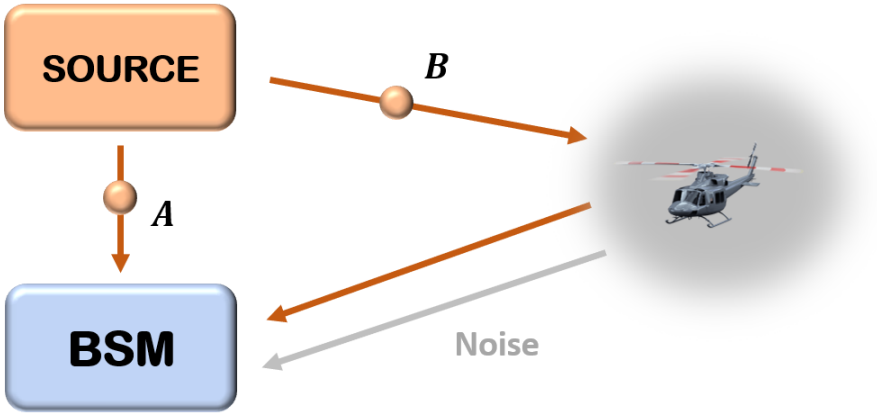

Figure 5.7: Quantum target detection scheme. Only the case in which the object reflects photon B and reaches the BSM is illustrated. Source: Made by the author.

The quantum gain of QDT is strongly related to the dimension of the Hilbert space we are working with. Using entangled quantum states the effective signal-to-noise ratio is $\sim d^2$. While using unentangled states the same ratio is $\sim d$ [106]. Therefore, entanglement reduces

the signal-to-noise ratio by a factor d in comparison with the unentangled case [106]. Note that QDT has already been implemented only using linear optics devices, but for $d = 2$ [52].

However, with linear optics for d=4, the effective signal-to-noise ratio is $\sim d^2/2 = 8$, because the minimum number of Bell states we can discriminate is two. We can overcome this limit by using our improved HDBSA. As we saw in section 5.4, we can always choose the ancillary photons depending on the Bell state generated by the source. This allows us to measure the Bell pair 50% of the time successfully and hence, have an ideal signal-to-noise ratio ($\sim d^2 = 16$). Then, the average effective signal-to-noise ratio is equal to

$$SN = 0.5 \times 8 + 0.5 \times 16 = 12, \tag{5.71}$$

which is an improvement of the protocol of quantum target detection with linear optics.

5.5 Conclusion

We designed a four-dimensional Bell state analyzer based entirely on fiber optical devices and using only path modes without involving non-linear processes. From two-photon interference in a pair of 4CF-BS, we separate the 16 Bell states into 7 groups, which has been shown to be optimal when we try to discriminate Bell states in a 4-dimensional Hilbert space [45]. We studied quantum teleportation, entanglement swapping, and superdense coding protocols as an application. In the latter, using the HDBSA we encoded more information for ququarts than for qubits or even for two qubits, exploiting the high dimensionality of the measurement. However, in the two remaining protocols that are more interesting than superdense coding, we obtain results equal to or slightly better than using qubits.

Motivated to improve the performance of our HDBSA for quantum teleportation and entanglement swapping, we increase the size of the Hilbert space by introducing two ancillary photons that interfere with the outputs of the original HDBSA. With this new scheme, we can distinguish a single Bell state 50% of the time from the same classes containing two states. Even though this HDBSA with auxiliary photons gives a low success probability when the states are equiprobable ($p_{\text{succ}} = 1/16$), once it works, we can achieve a maximum fidelity for quantum teleportation or a high-quality entanglement between the non-interacting parties in the entanglement swapping protocol. A direct and handy application is for quantum target detection where the quantum advantage scales with the dimension [52, 106]. Here only one Bell state is generated, leading to a success probability of $p_{\text{succ}} = 0.5$ of measuring and detecting the target that is in a noisy background. The HDBSA also allows us to improve the average signal-to-noise ratio from 8 to 12 in the $d = 4$ case.

Chapter 6

Conclusion

In this thesis, we studied two main applications for a 4×4 optical fiber beamsplitter using two-photon interference. The first one is the manipulation of quantum discord, and the second one is the design of a high-dimensional Bell state analyzer. These works do not involve nonlinear processes and are fully based on fiber devices, so we exploit the momentum degree of freedom of photons.

Our first result is presented in chapter 4. Using two weak coherent pulses as inputs, we first achieve a good quality two-photon interference in a 4×4 optical fiber beamsplitter. The photons after this device present correlations (different from entanglement since the input state is separable), so we post-select the output state and use a geometric measure of quantum discord to study this correlation. We found that the geometric discord can be maximized by adjusting the intensity mismatch ratio between the input weak coherent pulses.

The experimental group of quantum optics and information of the University of Concepción is involved in a project that connects the Faculty of Physical and Mathematical Sciences with the Faculty of Engineering through a 1 km multicore optical fiber. One of the first protocols we could implement with this link is remote state preparation using the experimental setup presented in chapter 4. It has been shown that states with quantum discord can outperform entangled states in this scenario [41]. In addition, the remote state preparation protocol is easier to achieve than quantum teleportation using entangled states.

One of the main problems in implementing linear optics quantum teleportation is the limitation in the Bell measurement. Even though full measurement has been achieved [45, 102, 103], they are based on hyperentanglement, which limits quantum teleportation since a third party cannot independently supply the input state. A solution to this measurement problem also allows other quantum protocols, such as entanglement swapping, which is a key ingredient for quantum nodes in quantum networks [9].

In chapter 5, we first design a high-dimensional Bell state analyzer for $d = 4$ that discriminate the 16 Bell states into 7 groups, which has been shown to be optimal for a 4-dimensional Hilbert space [45]. We discussed the performance of the HDBSA for quantum teleportation, entanglement swapping, and superdense coding. However, in the last two protocols, which are

the most interesting, we obtain results equal to or slightly better than using qubits. We then show that a pair of entangled ancilla photons can be used to probabilistic and unequivocally identify two Bell states.

Note that Wang *et. al.* [101] made quantum teleportation using a hyperentangled Bell detection with a success probability of 1/32. On the other hand, Xiao-Min *et. al.* [107] implemented high-dimensional quantum teleportation of a qutrit using only path mode, achieving a success probability of 1/54 and introducing ancillary photons they obtain a probability of 1/18. Compared with these two experiments, we obtain a higher success probability of 1/16 with our HDBSA when the Bell states are equiprobable. Nevertheless, Zang *et. al.* [108] in the four-dimensional case they have a success probability of 5/32 which is greater than 1/16. However, they need eight photons while we just need four, so following the calculations in subsection 5.3.3, our HDBSA is better as long as the detection efficiency is less than $\sim 80\%$.

Looking ahead, we could explore other ancilla states, such as entangled qubits or non-entangled ququarts, and study if there is any advantage over the HDBSA proposed. Further on, we could implement the HDBSA in the laboratories of the quantum optics and information group of the University of Concepción to do long distances quantum experiments, as those presented in chapter 5, using the after mentioning 1 km multicore link, with and without ancillary photons.

This thesis should contribute to the exploitation of quantum correlations and the implementation of Bell measurements in quantum communication protocols in future telecommunication networks, particularly those that exploit spatially structured fibers.

Bibliography

[1] Bennett, C. H. *et al.* Teleporting an unknown quantum state via dual classical and einstein-podolsky-rosen channels. *Phys. Rev. Lett.* **70**, 1895–1899 (1993). URL https://link.aps.org/doi/10.1103/PhysRevLett.70.1895.

[2] Gisin, N., Ribordy, G., Tittel, W. & Zbinden, H. Quantum cryptography. *Rev. Mod. Phys.* **74**, 145–195 (2002). URL https://link.aps.org/doi/10.1103/RevModPhys.74.145.

[3] O'Brien, J. L. Optical quantum computing. *Science* **318**, 1567–1570 (2007). URL https://www.science.org/doi/abs/10.1126/science.1142892. https://www.science.org/doi/pdf/10.1126/science.1142892.

[4] Preskill, J. Quantum computing in the NISQ era and beyond. *Quantum* **2**, 79 (2018). URL https://doi.org/10.22331/q-2018-08-06-79.

[5] Żukowski, M., Zeilinger, A., Horne, M. A. & Ekert, A. K. "event-ready-detectors" bell experiment via entanglement swapping. *Phys. Rev. Lett.* **71**, 4287 (1993). URL https://link.aps.org/doi/10.1103/PhysRevLett.71.4287.

[6] Nielsen, M. A. & Chuang, I. L. *Quantum Computation and Quantum Information: 10th Anniversary Edition* (Cambridge University Press, 2010).

[7] P., D. J. & J., M. G. Quantum technology: the second quantum revolution. *Trans. R. Soc. A.* **361**, 1655–1674 (2003). URL https://doi.org/10.1098/rsta.2003.1227.

[8] Ladd, T. D. *et al.* Quantum computers. *Nature* **464**, 45–53 (2010). URL https://doi.org/10.1038/nature08812.

[9] Flamini, F., Spagnolo, N. & Sciarrino, F. Photonic quantum information processing: a review. *Reports on Progress in Physics* **82**, 016001 (2018). URL https://doi.org/10.1088/1361-6633/aad5b2.

[10] Richardson, D. Filling the light pipe. *Science* **330**, 327 (2010). URL https://doi.org/10.1126/science.1191708.

[11] Essiambre, R.-J., Foschini, G. J., Kramer, G. & Winzer, P. J. Capacity limits of information transport in fiber-optic networks. *Phys. Rev. Lett.* **101**, 163901 (2008). URL https://link.aps.org/doi/10.1103/PhysRevLett.101.163901.

[12] Richardson, D. J., Fini, J. M. & Nelson, L. E. Space-division multiplexing in optical fibres. *Nature Photonics* **7**, 354 (2013). URL https://doi.org/10.1038/nphoton.2013.94.

[13] Da Lio, B. *et al.* Path-encoded high-dimensional quantum communication over a 2-km multicore fiber. *npj Quantum Information* **7**, 63 (2021). URL https://doi.org/10.1038/s41534-021-00398-y.

[14] Da Lio, B. *et al.* Stable transmission of high-dimensional quantum states over a 2-km multicore fiber. *IEEE Journal of Selected Topics in Quantum Electronics* **26**, 1–8 (2020).

[15] Bacco, D. *et al.* Characterization and stability measurement of deployed multicore fibers for quantum applications. *Photon. Res.* **9**, 1992–1997 (2021).

[16] Xavier, G. B. & Lima, G. Quantum information processing with space-division multiplexing optical fibres. *Communications Physics* **3**, 9 (2020). URL https://doi.org/10.1038/s42005-019-0269-7.

[17] Cozzolino, D., Da Lio, B., Bacco, D. & Oxenløwe, L. K. High-dimensional quantum communication: Benefits, progress, and future challenges. *Advanced Quantum Technologies* **2**, 1900038 (2019). URL https://doi.org/10.1002/qute.201900038.

[18] Dada, A. C., Leach, J., Buller, G. S., Padgett, M. J. & Andersson, E. Experimental high-dimensional two-photon entanglement and violations of generalized bell inequalities. *Nature Physics* **7**, 677–680 (2011). URL https://doi.org/10.1038/nphys1996.

[19] Neeley, M. *et al.* Emulation of a quantum spin with a superconducting phase qudit. *Science* **325**, 722–725 (2009). URL https://www.science.org/doi/abs/10.1126/science.1173440. https://www.science.org/doi/pdf/10.1126/science.1173440.

[20] Lanyon, B. P. *et al.* Simplifying quantum logic using higher-dimensional hilbert spaces. *Nature Physics* **5**, 134–140 (2009). URL https://doi.org/10.1038/nphys1150.

[21] Bechmann-Pasquinucci, H. & Tittel, W. Quantum cryptography using larger alphabets. *Phys. Rev. A* **61**, 062308 (2000). URL https://link.aps.org/doi/10.1103/PhysRevA.61.062308.

[22] Cerf, N. J., Bourennane, M., Karlsson, A. & Gisin, N. Security of quantum key distribution using d-level systems. *Phys. Rev. Lett.* **88**, 127902 (2002). URL https://link.aps.org/doi/10.1103/PhysRevLett.88.127902.

[23] Taddei, M. M. *et al.* Computational advantage from the quantum superposition of multiple temporal orders of photonic gates. *PRX Quantum* **2**, 010320 (2021).

[24] Ortega, E. A. *et al.* Experimental space-division multiplexed polarization-entanglement distribution through 12 paths of a multicore fiber. *PRX Quantum* **2**, 040356 (2021). URL https://link.aps.org/doi/10.1103/PRXQuantum.2.040356.

[25] Farkas, M., Guerrero, N., Cariñe, J., Cañas, G. & Lima, G. Self-testing mutually unbiased bases in higher dimensions with space-division multiplexing optical fiber technology. *Phys. Rev. Applied* **15**, 014028 (2021).

[26] Gómez, E. *et al.* Multidimensional entanglement generation with multicore optical fibers. *Phys. Rev. Applied* **15**, 034024 (2021).

[27] Ding, Y. *et al.* High-dimensional quantum key distribution based on multicore fiber using silicon photonic integrated circuits. *npj Quantum Information* **3**, 25 (2017). URL https://doi.org/10.1038/s41534-017-0026-2.

[28] Cariñe, J. *et al.* Multi-core fiber integrated multi-port beam splitters for quantum information processing. *Optica* **7**, 542 (2020). URL https://opg.optica.org/optica/abstract.cfm?URI=optica-7-5-542.

[29] Saygin, M. Y. *et al.* Robust architecture for programmable universal unitaries. *Phys. Rev. Lett.* **124**, 010501 (2020). URL https://link.aps.org/doi/10.1103/PhysRevLett.124.010501.

[30] Spagnolo, N. *et al.* Quantum interferometry with three-dimensional geometry. *Scientific Reports* **2**, 862 (2012). URL https://doi.org/10.1038/srep00862.

[31] Humphreys, P. C., Barbieri, M., Datta, A. & Walmsley, I. A. Quantum enhanced multiple phase estimation. *Phys. Rev. Lett.* **111**, 070403 (2013). URL https://link.aps.org/doi/10.1103/PhysRevLett.111.070403.

[32] Bouchard, F. *et al.* Two-photon interference: the hong–ou–mandel effect. *Reports on Progress in Physics* **84**, 012402 (2020). URL https://dx.doi.org/10.1088/1361-6633/abcd7a.

[33] Ou, Z. Y. & Mandel, L. Violation of bell's inequality and classical probability in a two-photon correlation experiment. *Phys. Rev. Lett.* **61**, 50–53 (1988). URL https://link.aps.org/doi/10.1103/PhysRevLett.61.50.

[34] Shih, Y. H. & Alley, C. O. New type of einstein-podolsky-rosen-bohm experiment using pairs of light quanta produced by optical parametric down conversion. *Phys. Rev. Lett.* **61**, 2921–2924 (1988). URL https://link.aps.org/doi/10.1103/PhysRevLett.61.2921.

[35] Mattle, K., Weinfurter, H., Kwiat, P. G. & Zeilinger, A. Dense coding in experimental quantum communication. *Phys. Rev. Lett.* **76**, 4656–4659 (1996). URL https://link.aps.org/doi/10.1103/PhysRevLett.76.4656.

[36] Walborn, S. P., Nogueira, W. A. T., Pádua, S. & Monken, C. H. Optical bell-state analysis in the coincidence basis. *Europhysics Letters (EPL)* **62**, 161–167 (2003). URL https://doi.org/10.1209/epl/i2003-00339-6.

[37] Grice, W. P. Arbitrarily complete bell-state measurement using only linear optical elements. *Phys. Rev. A* **84**, 042331 (2011). URL https://link.aps.org/doi/10.1103/PhysRevA.84.042331.

[38] Choi, Y. *et al.* Generation of a non-zero discord bipartite state with classical second-order interference. *Opt. Express* **25**, 2540 (2017). URL https://opg.optica.org/oe/abstract.cfm?URI=oe-25-3-2540.

[39] Ollivier, H. & Zurek, W. H. Quantum discord: A measure of the quantumness of correlations. *Phys. Rev. Lett.* **88**, 017901 (2001).

[40] Datta, A., Shaji, A. & Caves, C. M. Quantum discord and the power of one qubit. *Phys. Rev. Lett.* **100**, 050502 (2008). URL https://link.aps.org/doi/10.1103/PhysRevLett.100.050502.

[41] Dakić, B. *et al.* Quantum discord as resource for remote state preparation. *Nature Physics* **8**, 666–670 (2012). URL https://doi.org/10.1038/nphys2377.

[42] Pirandola, S. Quantum discord as a resource for quantum cryptography. *Scientific Reports* **4**, 6956 (2014). URL https://doi.org/10.1038/srep06956.

[43] Girolami, D. *et al.* Quantum discord determines the interferometric power of quantum states. *Phys. Rev. Lett.* **112**, 210401 (2014). URL https://link.aps.org/doi/10.1103/PhysRevLett.112.210401.

[44] Weedbrook, C., Pirandola, S., Thompson, J., Vedral, V. & Gu, M. How discord underlies the noise resilience of quantum illumination. *New Journal of Physics* **18**, 043027 (2016). URL https://dx.doi.org/10.1088/1367-2630/18/4/043027.

[45] Wei, T.-C., Barreiro, J. T. & Kwiat, P. G. Hyperentangled bell-state analysis. *Phys. Rev. A* **75**, 060305 (2007). URL https://doi.org/10.1103/PhysRevA.75.060305.

[46] Wootters, W. K. & Fields, B. D. Optimal state-determination by mutually unbiased measurements. *Annals of Physics* **191**, 363 (1989).

[47] Bouwmeester, D. *et al.* Experimental quantum teleportation. *Nature* **390**, 575–579 (1997). URL https://doi.org/10.1038/37539.

[48] Boschi, D., Branca, S., De Martini, F., Hardy, L. & Popescu, S. Experimental realization of teleporting an unknown pure quantum state via dual classical and einstein-podolsky-rosen channels. *Phys. Rev. Lett.* **80**, 1121–1125 (1998). URL https://link.aps.org/doi/10.1103/PhysRevLett.80.1121.

[49] Hu, X.-M. *et al.* Beating the channel capacity limit for superdense coding with entangled ququarts. *Science Advances* **4**, eaat9304 (2018). URL https://www.science.org/doi/abs/10.1126/sciadv.aat9304. https://www.science.org/doi/pdf/10.1126/sciadv.aat9304.

[50] Sangouard, N., Simon, C., de Riedmatten, H. & Gisin, N. Quantum repeaters based on atomic ensembles and linear optics. *Rev. Mod. Phys.* **83**, 33–80 (2011). URL https://link.aps.org/doi/10.1103/RevModPhys.83.33.

[51] Azuma, K., Tamaki, K. & Lo, H.-K. All-photonic quantum repeaters. *Nature Communications* **6**, 6787 (2015). URL https://doi.org/10.1038/ncomms7787.

[52] Aguilar, G. H. *et al.* Experimental investigation of linear-optics-based quantum target detection. *Phys. Rev. A* **99**, 053813 (2019). URL https://link.aps.org/doi/10.1103/PhysRevA.99.053813.

[53] Pan, J.-W., Bouwmeester, D., Weinfurter, H. & Zeilinger, A. Experimental entanglement swapping: Entangling photons that never interacted. *Phys. Rev. Lett.* **80**, 3891–3894 (1998). URL https://link.aps.org/doi/10.1103/PhysRevLett.80.3891.

[54] Knill, E., Laflamme, R. & Milburn, G. J. A scheme for efficient quantum computation with linear optics. *Nature* **409**, 46–52 (2001). URL https://doi.org/10.1038/35051009.

[55] Życzkowski, K., Horodecki, P., Sanpera, A. & Lewenstein, M. Volume of the set of separable states. *Phys. Rev. A* **58**, 883 (1998). URL https://link.aps.org/doi/10.1103/PhysRevA.58.883.

[56] Vidal, G. & Werner, R. F. Computable measure of entanglement. *Phys. Rev. A* **65**, 032314 (2002). URL https://link.aps.org/doi/10.1103/PhysRevA.65.032314.

[57] Plenio, M. B. Logarithmic negativity: A full entanglement monotone that is not convex. *Phys. Rev. Lett.* **95**, 090503 (2005). URL https://link.aps.org/doi/10.1103/PhysRevLett.95.090503.

[58] Ollivier, H. & Zurek, W. H. Quantum discord: A measure of the quantumness of correlations. *Phys. Rev. Lett.* **88**, 017901 (2001). URL https://link.aps.org/doi/10.1103/PhysRevLett.88.017901.

[59] Modi, K., Brodutch, A., Cable, H., Paterek, T. & Vedral, V. The classical-quantum boundary for correlations: Discord and related measures. *Rev. Mod. Phys.* **84**, 1655 (2012). URL https://link.aps.org/doi/10.1103/RevModPhys.84.1655.

[60] Piani, M., Horodecki, P. & Horodecki, R. No-local-broadcasting theorem for multipartite quantum correlations. *Phys. Rev. Lett.* **100**, 090502 (2008). URL https://link.aps.org/doi/10.1103/PhysRevLett.100.090502.

[61] Dakić, B., Vedral, V. & Brukner, i. c. v. Necessary and sufficient condition for nonzero quantum discord. *Phys. Rev. Lett.* **105**, 190502 (2010).

[62] De Vicente, J. I. Separability criteria based on the bloch representation of density matrices. *Quantum Info. Comput.* **7**, 624–638 (2007). URL https://doi.org/10.48550/arXiv.quant-ph/0607195.

[63] Wu, X. *et al.* A concise review of rydberg atom based quantum computation and quantum simulation. *Chinese Physics B* **30**, 020305 (2021). URL https://doi.org/10.1088/1674-1056/abd76f.

[64] Xin, T. *et al.* Nuclear magnetic resonance for quantum computing: Techniques and recent achievements. *Chinese Physics B* **27**, 020308 (2018). URL https://doi.org/10.1088/1674-1056/27/2/020308.

[65] Vandersypen, L. M. K. *et al.* Interfacing spin qubits in quantum dots and donors–hot, dense, and coherent. *npj Quantum Information* **3**, 34 (2017). URL https://doi.org/10.1038/s41534-017-0038-y.

[66] Kjaergaard, M. *et al.* Superconducting qubits: Current state of play. *Annual Review of Condensed Matter Physics* **11**, 369–395 (2020). URL https://doi.org/10.1146/annurev-conmatphys-031119-050605.

[67] James, D. F. V., Kwiat, P. G., Munro, W. J. & White, A. G. Measurement of qubits. *Phys. Rev. A* **64**, 052312 (2001). URL https://link.aps.org/doi/10.1103/PhysRevA.64.052312.

[68] Mair, A., Vaziri, A., Weihs, G. & Zeilinger, A. Entanglement of the orbital angular momentum states of photons. *Nature* **412**, 313–316 (2001). URL https://doi.org/10.1038/35085529.

[69] Erhard, M., Malik, M., Krenn, M. & Zeilinger, A. Experimental greenberger–horne–zeilinger entanglement beyond qubits. *Nature Photonics* **12**, 759–764 (2018). URL https://doi.org/10.1038/s41566-018-0257-6.

[70] Saleh, B. E. A. & Malvin, C. T. *Fundamentals of Photonics* (Wiley, 1991).

[71] Cariñe, J., Asan-Srain, M. N., Lima, G. & Walborn, S. P. Maximizing quantum discord from interference in multi-port fiber beamsplitters. *npj Quantum Information* **7**, 172 (2021). URL https://www.nature.com/articles/s41534-021-00502-2.

[72] Gan, L. *et al.* Spatial-division multiplexed mach–zehnder interferometers in heterogeneous multicore fiber for multiparameter measurement. *IEEE Photonics Journal* **8**, 1–8 (2016).

[73] Brod, D. J. Bosons vs. fermions – a computational complexity perspective. *Rev. Bras. Ensino Fís* **43**, (Supp. 1) (2021).

[74] Hu, M.-L. *et al.* Quantum coherence and geometric quantum discord. *Physics Reports* **762-764**, 1–100 (2018). Quantum coherence and geometric quantum discord.

[75] Bera, A. *et al.* Quantum discord and its allies: a review of recent progress. *Reports on Progress in Physics* **81**, 024001 (2017). URL https://doi.org/10.1088/1361-6633/aa872f.

[76] Walborn, S. P., Terra Cunha, M. O., Pádua, S. & Monken, C. H. Double-slit quantum eraser. *Phys. Rev. A* **65**, 033818 (2002). URL https://link.aps.org/doi/10.1103/PhysRevA.65.033818.

[77] Torres-Ruiz, F. A., Lima, G., Delgado, A., Pádua, S. & Saavedra, C. Decoherence in a double-slit quantum eraser. *Phys. Rev. A* **81**, 042104 (2010).

[78] Hong, C. K., Ou, Z. Y. & Mandel, L. Measurement of subpicosecond time intervals between two photons by interference. *Phys. Rev. Lett.* **59**, 2044–2046 (1987). URL https://link.aps.org/doi/10.1103/PhysRevLett.59.2044.

[79] Scully, M. O. & Zubairy, M. S. *Quantum Optics* (Cambridge University Press, 1997).

[80] Ali, M., Rau, A. R. P. & Alber, G. Quantum discord for two-qubit x states. *Phys. Rev. A* **81**, 042105 (2010).

[81] Quesada, N., Al-Qasimi, A. & James, D. F. Quantum properties and dynamics of x states. *Journal of Modern Optics* **59**, 1322 (2012). URL https://doi.org/10.1080/09500340.2012.713130.

[82] Young, J. D. & Auyuanet, A. Entanglement-coherence and discord-coherence analytical relations for x states. *Quantum Information Processing* **19**, 398 (2020). URL https://doi.org/10.1007/s11128-020-02907-y.

[83] Girolami, D. & Adesso, G. Interplay between computable measures of entanglement and other quantum correlations. *Phys. Rev. A* **84**, 052110 (2011). URL https://link.aps.org/doi/10.1103/PhysRevA.84.052110.

[84] Maziero, J., Céleri, L. C., Serra, R. M. & Vedral, V. Classical and quantum correlations under decoherence. *Phys. Rev. A* **80**, 044102 (2009). URL https://link.aps.org/doi/10.1103/PhysRevA.80.044102.

[85] Fanchini, F. F., Werlang, T., Brasil, C. A., Arruda, L. G. E. & Caldeira, A. O. Non-markovian dynamics of quantum discord. *Phys. Rev. A* **81**, 052107 (2010). URL https://link.aps.org/doi/10.1103/PhysRevA.81.052107.

[86] Xu, J.-S. *et al.* Experimental investigation of classical and quantum correlations under decoherence. *Nature Communications* **1**, 7 (2010). URL https://doi.org/10.1038/ncomms1005.

[87] Auccaise, R. *et al.* Environment-induced sudden transition in quantum discord dynamics. *Phys. Rev. Lett.* **107**, 140403 (2011). URL https://link.aps.org/doi/10.1103/PhysRevLett.107.140403.

[88] Werlang, T., Trippe, C., Ribeiro, G. A. P. & Rigolin, G. Quantum correlations in spin chains at finite temperatures and quantum phase transitions. *Phys. Rev. Lett.* **105**, 095702 (2010). URL https://link.aps.org/doi/10.1103/PhysRevLett.105.095702.

[89] Maziero, J., Guzman, H. C., Céleri, L. C., Sarandy, M. S. & Serra, R. M. Quantum and classical thermal correlations in the XY spin-$\frac{1}{2}$ chain. *Phys. Rev. A* **82**, 012106 (2010). URL https://link.aps.org/doi/10.1103/PhysRevA.82.012106.

[90] Mazzola, L., Piilo, J. & Maniscalco, S. Sudden transition between classical and quantum decoherence. *Phys. Rev. Lett.* **104**, 200401 (2010). URL https://link.aps.org/doi/10.1103/PhysRevLett.104.200401.

[91] Cornelio, M. F. *et al.* Emergence of the pointer basis through the dynamics of correlations. *Phys. Rev. Lett.* **109**, 190402 (2012). URL https://link.aps.org/doi/10.1103/PhysRevLett.109.190402.

[92] Bennett, C. H. *et al.* Remote state preparation. *Phys. Rev. Lett.* **87**, 077902 (2001). URL https://link.aps.org/doi/10.1103/PhysRevLett.87.077902.

[93] Salles, A. *et al.* Experimental investigation of the dynamics of entanglement: Sudden death, complementarity, and continuous monitoring of the environment. *Phys. Rev. A* **78**, 022322 (2008). URL https://link.aps.org/doi/10.1103/PhysRevA.78.022322.

[94] Weinfurter, H. Experimental bell-state analysis. *Europhysics Letters* **25**, 559 (1994). URL https://dx.doi.org/10.1209/0295-5075/25/8/001.

[95] Calsamiglia, J. & Lütkenhaus, N. Maximum efficiency of a linear-optical bell-state analyzer. *Applied Physics B* **72**, 67–71 (2001). URL https://doi.org/10.1007/s003400000484.

[96] Kim, Y.-H., Kulik, S. P. & Shih, Y. Quantum teleportation of a polarization state with a complete bell state measurement. *Phys. Rev. Lett.* **86**, 1370–1373 (2001). URL https://link.aps.org/doi/10.1103/PhysRevLett.86.1370.

[97] Kwiat, P. G. & Weinfurter, H. Embedded bell-state analysis. *Phys. Rev. A* **58**, R2623 (1998). URL https://doi.org/10.1103/PhysRevA.58.R2623.

[98] Ewert, F. & van Loock, P. 3/4-efficient bell measurement with passive linear optics and unentangled ancillae. *Phys. Rev. Lett.* **113**, 140403 (2014). URL https://link.aps.org/doi/10.1103/PhysRevLett.113.140403.

[99] Olivo, A. & Grosshans, F. Ancilla-assisted linear optical bell measurements and their optimality. *Phys. Rev. A* **98**, 042323 (2018). URL https://link.aps.org/doi/10.1103/PhysRevA.98.042323.

[100] Bayerbach, M. J., D'Aurelio, S. E., van Loock, P. & Barz, S. Bell-state measurement exceeding 50% success probability with linear optics (2022). URL https://arxiv.org/abs/2208.02271.

[101] Wang, X.-L. *et al.* Quantum teleportation of multiple degrees of freedom of a single photon. *Nature* **518**, 516–519 (2015). URL https://doi.org/10.1038/nature14246.

[102] Zhang, H. *et al.* Arbitrary two-particle high-dimensional bell-state measurement by auxiliary entanglement. *Phys. Rev. A* **99**, 052301 (2019). URL https://link.aps.org/doi/10.1103/PhysRevA.99.052301.

[103] Gao, C.-Y., Ren, B.-C., Zhang, Y.-X., Ai, Q. & Deng, F.-G. Universal linear-optical hyperentangled bell-state measurement. *Applied Physics Express* **13**, 027004 (2020). URL https://dx.doi.org/10.35848/1882-0786/ab67d2.

[104] Pirandola, S., Eisert, J., Weedbrook, C., Furusawa, A. & Braunstein, S. L. Advances in quantum teleportation. *Nature Photonics* **9**, 641–652 (2015). URL https://doi.org/10.1038/nphoton.2015.154.

[105] BruB, D. & Macchiavello, C. Optimal state estimation for d-dimensional quantum systems. *Physics Letters A* **253**, 249–251 (1999). URL https://www.sciencedirect.com/science/article/pii/S0375960199000997.

[106] Lloyd, S. Enhanced sensitivity of photodetection via quantum illumination. *Science* **321**, 1463–1465 (2008). URL https://www.science.org/doi/abs/10.1126/science.1160627.

[107] Hu, X.-M. *et al.* Experimental high-dimensional quantum teleportation. *Phys. Rev. Lett.* **125**, 230501 (2020). URL https://link.aps.org/doi/10.1103/PhysRevLett.125.230501.

[108] Zhang, C. *et al.* Quantum teleportation of photonic qudits using linear optics. *Phys. Rev. A* **100**, 032330 (2019). URL https://link.aps.org/doi/10.1103/PhysRevA.100.032330.

Appendix A

Python Programs

A1 Evolution Creation Operators

Python program to calculate the output creation operators representing the two-photon state after the 4CF-BS corresponding to the eqs. (4.4), (4.5) and (4.6).

```
#%%
import sympy as sp

# Matrix for the 4CF-BS. Note that we didnt consider the factor 1/2
BS4 = sp.Matrix([[1,1,1,1],
                 [1,1,-1,-1],
                 [1,-1,1,-1],
                 [1,-1,-1,1]])

# Creation operators.
a0 = sp.Matrix([[1],[0],[0],[0]])
a1 = sp.Matrix([[0],[1],[0],[0]])
a2 = sp.Matrix([[0],[0],[1],[0]])
a3 = sp.Matrix([[0],[0],[0],[1]])

# How interact the different modes od the 4CF-BS
BS4*a0,BS4*a1,BS4*a2,BS4*a3
#%%
# is direct to get the evolution of the operators a1^2 and a3^2, but for we need
    to define the variables
A0,A1,A2,A3= sp.symbols("a_0:4", real=True)

# Then the evoluted operator a1a3 is
sp.expand((A0+A1-A2-A3)*(A0-A1-A2+A3))
```

A2 Output Density Matrix

Python program to calculate the 10×10 output matrices in eqs. (4.7) and (4.8).

```
import sympy as sp

```

```
g= sp.Symbol("gamma")

A2000 = sp.Matrix([[1],[0],[0],[0],[0],[0],[0],[0],[0],[0]])
A0200 = sp.Matrix([[0],[1],[0],[0],[0],[0],[0],[0],[0],[0]])
A0020 = sp.Matrix([[0],[0],[1],[0],[0],[0],[0],[0],[0],[0]])
A0002 = sp.Matrix([[0],[0],[0],[1],[0],[0],[0],[0],[0],[0]])
A1100 = sp.Matrix([[0],[0],[0],[0],[1],[0],[0],[0],[0],[0]])
A1010 = sp.Matrix([[0],[0],[0],[0],[0],[1],[0],[0],[0],[0]])
A1001 = sp.Matrix([[0],[0],[0],[0],[0],[0],[1],[0],[0],[0]])
A0110 = sp.Matrix([[0],[0],[0],[0],[0],[0],[0],[1],[0],[0]])
A0101 = sp.Matrix([[0],[0],[0],[0],[0],[0],[0],[0],[1],[0]])
A0011 = sp.Matrix([[0],[0],[0],[0],[0],[0],[0],[0],[0],[1]])

BS4a1= (sp.sqrt(2)*(A2000 +A0200 +A0020 +A0002) + 2*(A1100 -A1001 -A0110 -A0101
    +A0011 -A1010))/4
BS4a3 = (sp.sqrt(2)*(A2000 +A0200 +A0020 +A0002) + 2*(A1001 -A1100 -A1010 +A0110
     -A0101 -A0011))/4
BS4a1a3 = (sp.sqrt(2)*(A2000 -A0200 +A0020 -A0002) + 2*(A0101 -A1010))/4

rho_output = ((BS4a1*BS4a1.T+ (g**2)*BS4a3*BS4a3.T)/2 + 2*g*BS4a1a3*BS4a1a3.T)
    *16

rho_output_g1= rho_output.subs(g,1)/4

```

A3 Max Term

With this python program we obtain the plot shown in Fig. 4.4, which helps us to find the maximum eigenvalue of the matrix K (see eq. (4.16)).

```
import numpy as np
import matplotlib.pyplot as mlp

g= np.arange(0,1,0.01)

t = (1+4*g+g**2)/(1+g)**2
v = (1-4*g+g**2)/(1+g)**2
u = (1-g)/(1+g)
w = (1+g**2)/(1+g)**2

Cxx = (w+v)/2
Cyy = (w-v)/2
Czz = (t-w)/2

k1= Cxx + Cxx**2
k2 = Cyy**2

def D(k):
    D= (Cxx+Cxx**2+Cyy**2+Czz**2-k)/2
    return D

mlp.plot(g, k2/6, label=r"$k_1$",color="red")
```

```
mlp.plot(g,k1/6, label=r"$k_1$", color="orange")
mlp.scatter(0.435, 0.03, label=r"$\gamma\approx 0.435$", color="black")
mlp.xlabel(r"$\gamma$", size=15)

mlp.legend()
mlp.savefig("maxterm_comparison.pdf")

# mlp.plot(g, D(k1))
# mlp.plot(g, D(k2))
# mlp.grid()
# mlp.ylim(0,0.2)


```

A4 Classes Clasification

Python program to classify the classes shown in eqs. (5.26) to (5.32).

```
import sympy as sp
from IPython.display import display, Math

A0, A1,A2,A3 = sp.symbols("A_0:4", real=True)
B0, B1,B2,B3 = sp.symbols("B_0:4", real=True)

UMCF=sp.Matrix([[1,1,0,0,1,1,0,0],
                [1,1,0,0,-1,-1,0,0],
                [0,0,1,1,0,0,1,1],
                [0,0,1,1,0,0,-1,-1],
                [1,-1,0,0,1,-1,0,0],
                [1,-1,0,0,-1,1,0,0],
                [0,0,1,-1,0,0,1,-1],
                [0,0,1,-1,0,0,-1,1]])

phase=sp.Matrix([[1,0,0,0,0,0,0,0],
                [0,-1,0,0,0,0,0,0],
                [0,0,1,0,0,0,0,0],
                [0,0,0,1,0,0,0,0],
                [0,0,0,0,1,0,0,0],
                [0,0,0,0,0,-1,0,0],
                [0,0,0,0,0,0,1,0],
                [0,0,0,0,0,0,0,1]])

Re1=sp.Matrix([[0,0,0,0,0,0,0,1],
                [0,0,0,0,0,1,0,0],
                [0,0,0,1,0,0,0,0],
                [0,1,0,0,0,0,0,0],
                [0,0,1,0,0,0,0,0],
                [1,0,0,0,0,0,0,0],
                [0,0,0,0,0,0,1,0],
                [0,0,0,0,1,0,0,0]])

Re2=sp.Matrix([[1,0,0,0,0,0,0,0],
```

```
                [0,1,0,0,0,0,0,0],
                [0,0,0,0,1,0,0,0],
                [0,0,0,0,0,1,0,0],
                [0,0,1,0,0,0,0,0],
                [0,0,0,1,0,0,0,0],
                [0,0,0,0,0,0,1,0],
                [0,0,0,0,0,0,0,1]])

U= Re2*UMCF*Re1/2

a = [A0,A1,B0, B1,A2,A3,B2,B3]
def a_in(j):
    """Given the input creation operators and the matrix that gives me the
    evolution of the system, I can have the output creation operators that will
    act on the empty state. output creation operators that will act on the
    vacuum state. This function is in the form of eq. (3.12) of the thesis.
    j (str): mode in which my state is

    output: output operators
    """
    aj = 0
    for i in range(0,8):
        aj += U1[i, j]*a[i]
    return aj

# CLASS 1
display(Math(r"|\Phi^{-} \rangle |\phi^{+} \rangle"));
sp.expand(a_in(0)*a_in(2)-a_in(1)*a_in(3)+a_in(4)*a_in(6)-a_in(5)*a_in(7))/2

display(Math(r"|\Phi^{+} \rangle |\phi^{-} \rangle"));
sp.expand(a_in(0)*a_in(2)+a_in(1)*a_in(3)-a_in(4)*a_in(6)-a_in(5)*a_in(7))/2

display(Math(r"|\Psi^{+} \rangle |\psi^{-} \rangle"));
sp.expand(a_in(0)*a_in(7)+a_in(1)*a_in(6)-a_in(4)*a_in(3) - a_in(5)*a_in(2))/2

display(Math(r"|\Psi^{-} \rangle |\psi^{+} \rangle"));
sp.expand(a_in(0)*a_in(7)-a_in(1)*a_in(6)+a_in(4)*a_in(3) - a_in(5)*a_in(2))/2

#CLASS 2

display(Math(r"|\Phi^{+} \rangle |\phi^{+} \rangle"));
sp.expand(a_in(0)*a_in(2)+a_in(1)*a_in(3)+a_in(4)*a_in(6)+a_in(5)*a_in(7))/2

display(Math(r"|\Phi^{-} \rangle |\phi^{-} \rangle"));
sp.expand(a_in(0)*a_in(2)-a_in(1)*a_in(3)-a_in(4)*a_in(6)+a_in(5)*a_in(7))/2

#CLASS 3
display(Math(r"|\Psi^{-} \rangle |\psi^{-} \rangle"));
sp.expand(a_in(0)*a_in(7)-a_in(1)*a_in(6)- a_in(4)*a_in(3)+ a_in(5)*a_in(2))/2

display(Math(r"|\Psi^{+} \rangle |\psi^{+} \rangle"));
sp.expand(a_in(0)*a_in(7)+a_in(1)*a_in(6)+ a_in(4)*a_in(3)+a_in(5)*a_in(2))/2

```

```
#CLASS 4
display(Math(r"|\Psi^{+} \rangle |\phi^{-} \rangle"));
sp.expand(a_in(0)*a_in(3)+a_in(1)*a_in(2)-a_in(4)*a_in(7)-a_in(5)*a_in(6))/2

display(Math(r"|\Phi^{+} \rangle |\psi^{-} \rangle"));
sp.expand(a_in(0)*a_in(6)+a_in(1)*a_in(7)-a_in(4)*a_in(2)-a_in(5)*a_in(3))/2

#CLASS 5
display(Math(r"|\Psi^{-} \rangle |\phi^{+} \rangle"));
sp.expand(a_in(0)*a_in(3)-a_in(1)*a_in(2)+a_in(4)*a_in(7)-a_in(5)*a_in(6))/2

display(Math(r"|\Phi^{-} \rangle |\psi^{+} \rangle"));
sp.expand(a_in(0)*a_in(6)-a_in(1)*a_in(7)+a_in(4)*a_in(2)-a_in(5)*a_in(3))/2

#CLASS 6
display(Math(r"|\Psi^{+} \rangle |\phi^{+} \rangle"));
sp.expand(a_in(0)*a_in(3)+a_in(1)*a_in(2)+a_in(4)*a_in(7)+a_in(5)*a_in(6))/2

display(Math(r"|\Phi^{-} \rangle |\psi^{-} \rangle"));
sp.expand(a_in(0)*a_in(6)-a_in(1)*a_in(7)-a_in(4)*a_in(2)+a_in(5)*a_in(3))/2

#CLASS 7
display(Math(r"|\Psi^{-} \rangle |\phi^{-} \rangle"));
sp.expand(a_in(0)*a_in(3)-a_in(1)*a_in(2)-a_in(4)*a_in(7)+a_in(5)*a_in(6))/2

display(Math(r"|\Phi^{+} \rangle |\psi^{+} \rangle"));
sp.expand(a_in(0)*a_in(6)+a_in(1)*a_in(7)+a_in(4)*a_in(2)+a_in(5)*a_in(3))/2

```

A5 Teleportation Fidelities

Python program to calculate the fidelities in the teleportation protocol between the state teleported and the state received for the cases shown in subsection 5.3.1.

```
import numpy as np
# %%
def MUBS(f):
    """M0"""
    print(f(1,0,0,0),f(0,1,0,0),f(0,0,1,0),f(0,0,0,1))
    """M1"""
    print(f(0.5,0.5,0.5,0.5), f(0.5,0.5,-0.5,-0.5), f(0.5,-0.5,-0.5,0.5), f
    (0.5,-0.5,0.5,-0.5))
    """M2"""
    print(f(0.5,-0.5,-0.5j,-0.5j), f(0.5,-0.5,0.5j,0.5j), f(0.5,0.5,0.5j,-0.5j),
    f(0.5,0.5,-0.5j,0.5j))
    """M3"""
    print(f(0.5,-0.5j,-0.5j,-0.5), f(0.5,-0.5j,0.5j,0.5), f(0.5,0.5j,0.5j,-0.5),
     f(0.5,0.5j,-0.5j,0.5))
    """M4"""
    print(f(0.5,-0.5j,-0.5,-0.5j), f(0.5,-0.5j,0.5,0.5j), f(0.5,0.5j,-0.5,0.5j),
     f(0.5,0.5j,0.5,-0.5j))

```

```
def F_classical(a, b, c, d):
    norm = (abs(a)**2 +abs(b)**2 +abs(c)**2 +abs(d)**2)
    ff = (abs(a)**4+abs(d)**4+abs(c)**4+abs(b)**4)/norm
    return ff

def F_qubit(a, b, c, d):
    # This expression it is already normalized
    ff = (abs(a)**2+abs(d)**2)
    return ff

def F1_ququart(a, b, c, d):
    norm = 2*(abs(a)**2 +abs(b)**2 +abs(c)**2 +abs(d)**2)
    ff= ((abs(a)**4 + abs(b)**4 + abs(d)**4 + abs(c)**4
    -(a*np.conjugate(d))**2 -(np.conjugate(a)*d)**2
    -(b*np.conjugate(c))**2- (c*np.conjugate(b))**2)/norm)
    return ff

def F2_ququart(a, b, g, d):
    norm = (abs(a)**2 +abs(b)**2 +abs(g)**2 +abs(d)**2)
    ff = (abs(a)**4 +abs(b)**4 +abs(g)**4 +abs(d)**4 +2*abs(b)**2*abs(g)**2
            +2*abs(d)**2*abs(a)**2)/norm
    return ff

# We do not write the fidelity for class 3 since it is exactly the same than for
     class 2.

def F4_Uququart(a, b, c, d):
    norm =(2*(abs(a)**2 +abs(b)**2 +abs(c)**2 +abs(d)**2))
    ff= (((abs(a)**2 +abs(b)**2 +abs(c)**2 +abs(d)**2)**2
        +(np.conjugate(b)*c+np.conjugate(c)*b +np.conjugate(a)*d
        +np.conjugate(d)*a)**2)/norm)
    return ff

def F5_Uququart(a, b, c, d):
    norm =(2*(abs(a)**2 +abs(b)**2 +abs(c)**2 +abs(d)**2))
    ff= ((abs(a)**2 +abs(b)**2 +abs(c)**2 +abs(d)**2)**2
        +(np.conjugate(b)*c+np.conjugate(c)*b +np.conjugate(a)*d
        +np.conjugate(d)*a)**2)/norm
    return ff

def F6_Uququart(a, b, c, d):
    norm =(2*(abs(a)**2 +abs(b)**2 +abs(c)**2 +abs(d)**2))
    ff= (((abs(a)**2 +abs(b)**2 +abs(c)**2 +abs(d)**2)**2
        +(np.conjugate(b)*c-np.conjugate(a)*d -np.conjugate(d)*a
        +np.conjugate(c)*b)**2)/norm)
    return ff

def F7_Uququart(a, b, c, d):
    norm =(2*(abs(a)**2 +abs(b)**2 +abs(c)**2 +abs(d)**2))
    ff= (((abs(a)**2 +abs(b)**2 +abs(c)**2 +abs(d)**2)**2
        +(np.conjugate(c)*b-np.conjugate(a)*d -np.conjugate(d)*a
        +np.conjugate(b)*c)**2)/norm)
    return ff
```

A6 Logarithmic Negativity

Python program to calculate the logarithmic negativity as a measure of entanglement between the states swapped in subsection 5.3.2.

```
import numpy as np

def negativity(rho_transpuesto):
    norm_rho = np.linalg.norm(rho_transpuesto, ord="nuc")
    return (norm_rho-1)/2

def log_negativity(rho_transpuesto):
    norm_rho = np.linalg.norm(rho_transpuesto, ord="nuc")
    return np.log2(norm_rho)

def trace_one(rho):
    return np.trace(rho)

# partial transpose matrix of the eq. (2.27)
rhoTP_qubit=  1/2*np.array([[1, 0, 0,0],
                            [0, 0, 1,0],
                            [0, 1, 0,0],
                            [0, 0, 0,1]
                            ])

# partial transpose matrix of rho^{id}_{AB}
rhoTP_id =   1/4*np.array([[1, 0, 0,0,0, 0, 0,0,0, 0, 0,0,0, 0, 0,0],
                            [0, 0, 0,0,1, 0, 0,0,0, 0, 0,0,0, 0, 0,0],
                            [0, 0, 0,0,0, 0, 0,0,1, 0, 0,0,0, 0, 0,0],
                            [0, 0, 0,0,0, 0, 0,0,0, 0, 0,0,1, 0, 0,0],
                            [0, 1, 0,0,0, 0, 0,0,0, 0, 0,0,0, 0, 0,0],
                            [0, 0, 0,0,0, 1, 0,0,0, 0, 0,0,0, 0, 0,0],
                            [0, 0, 0,0,0, 0, 0,0,0, 1, 0,0,0, 0, 0,0],
                            [0, 0, 0,0,0, 0, 0,0,0, 0, 0,0,0, 1, 0,0],
                            [0, 0, 1,0,0, 0, 0,0,0, 0, 0,0,0, 0, 0,0],
                            [0, 0, 0,0,0, 0, 1,0,0, 0, 0,0,0, 0, 0,0],
                            [0, 0, 0,0,0, 0, 0,0,0, 0, 1,0,0, 0, 0,0],
                            [0, 0, 0,0,0, 0, 0,0,0, 0, 0,0,0, 0, 1,0],
                            [0, 0, 0,1,0, 0, 0,0,0, 0, 0,0,0, 0, 0,0],
                            [0, 0, 0,0,0, 0, 0,1,0, 0, 0,0,0, 0, 0,0],
                            [0, 0, 0,0,0, 0, 0,0,0, 0, 0,1,0, 0, 0,0],
                            [0, 0, 0,0,0, 0, 0,0,0, 0, 0,0,0, 0, 0,1]
                            ])

# partial transpose matrix of rho^{(2)}_{AB}
rho2TP=  1/4* np.array([[1, 0, 0,0,0, 0, 0,0,0, 0, 0,0,0, 0, 0,0],#00
                        [0, 0, 0,0,0, 0, 0,0,0, 0, 0,0,0, 0, 0,0],#01
                        [0, 0, 0,0,0, 0, 0,0,0, 0, 0,0,0, 0, 0,0],#02
                        [0, 0, 0,0,0, 0, 0,0,0, 0, 0,0,1, 0, 0,0],#03
                        [0, 0, 0,0,0, 0, 0,0,0, 0, 0,0,0, 0, 0,0],#10
                        [0, 0, 0,0,0, 1, 0,0,0, 0, 0,0,0, 0, 0,0],#11
                        [0, 0, 0,0,0, 0, 0,0,0, 1, 0,0,0, 0, 0,0],
                        [0, 0, 0,0,0, 0, 0,0,0, 0, 0,0,0, 0, 0,0],
```

```
                          [0, 0, 0,0,0, 0, 0,0,0, 0, 0,0,0, 0, 0,0],
                          [0, 0, 0,0,0, 0, 1,0,0, 0, 0,0,0, 0, 0,0],
                          [0, 0, 0,0,0, 0, 0,0,0, 0, 1,0,0, 0, 0,0],#22
                          [0, 0, 0,0,0, 0, 0,0,0, 0, 0,0,0, 0, 0,0],
                          [0, 0, 0,1,0, 0, 0,0,0, 0, 0,0,0, 0, 0,0],
                          [0, 0, 0,0,0, 0, 0,0,0, 0, 0,0,0, 0, 0,0],
                          [0, 0, 0,0,0, 0, 0,0,0, 0, 0,0,0, 0, 0,0],
                          [0, 0, 0,0,0, 0, 0,0,0, 0, 0,0,0, 0, 0,1]
                          ])
```

A7 Discrimination Criteria

Python program where we introduce the ancillary photons to the original HDBSA. With the funcion *criteria* we are able to discriminate when two classes have different outcomes, and hence, we can discriminate them.

```
import sympy as sp
from IPython.display import display, Math
 sp.init_printing()

A0, A1,A2,A3  = sp.symbols("A_0:4", real=True, positive= True)
B0, B1,B2,B3 = sp.symbols("B_0:4", real=True, positive= True)
E0, E1,E2,E3  = sp.symbols("E_0:4", real=True, positive= True)
F0, F1,F2,F3 = sp.symbols("F_0:4", real=True, positive= True)

def anc_in(j):
    """Given the input creation operators and the matrix that gives me the
    evolution of the system, I can have the output creation operators that will
    act on the empty state. output creation operators that will act on the empty
     state. This function has the form a_in = SUM U_wei a_out
    input
    j (str): mode
    output: output creation operator
    """
    anc = [A0,A1,B0, B1,A2,A3,B2,B3,E0,E1,F0,F1,E2,E3,F2,F3]
    aj = 0
    for i in range(0,16):
        aj += AncillaUnitary[i, j]*anc[i]
    return aj

def terms_abs(a, ancilla):
    # Considering the classes have interacted with the ancillas already,
    #  this function take the absolute value of every term and store each
    # term in a list
    list = []
    for i in sp.expand((a*ancilla)).args:
        list.append(abs(i))
    return list

def inter(lst1, lst2):
    # Function that takes the two list and return the intersection of the
    # elements of both lists.
```

```
    temp = set(lst2)
    lst3 = [value for value in lst1 if value in temp]
    return lst3

def criteria2(ancilla):
# For the indicated ancilla, the function analyze the different classes
# and return the sets that this ancilla allows to distinguish
    for i in range(len(list_classes)):
        for j in range(len(list_classes)):
            term_i = terms_abs(list_classes[i],ancilla)
            term_j = terms_abs(list_classes[j],ancilla)
            xx = inter(term_i,term_j)
            if xx != [] and len(xx) < len(term_i) :
            # If the intersection of both classes are different from the
            # empty set and if the set of the intersection is smaller than
            # the set of any of the classes, print the following
                print("the sets "+ list_names[i]+" and "+list_names[j]
                +" are distinguishable, with "+ str(len(xx))
                +" terms in common. Each class has "
                +str(len(term_i))+", " + str(len(term_j))+" elements" )

def terms_diff(list1,list2,anc):
    # Given the return of "criteria2", with this function we can know
    # the amplitude of the elements that makes two states distinguishable
    diff = set(terms_abs(list1, anc))-set(terms_abs(list2, anc))
    return diff

# Unitary matrix of the BS where the original outcomes will interefere with the
    ancillary photons
BS2=sp.Matrix([[1 ,0 ,0 ,0,0 ,0 ,0,0,1,0,0,0,0,0,0,0],
               [0 ,1 ,0 ,0,0 ,0 ,0,0,0,-1,0,0,0,0,0,0],
               [0 ,0 ,1 ,0,0 ,0 ,0,0,0,0,1,0,0,0,0,0],
               [0 ,0 ,0 ,1,0 ,0 ,0,0,0,0,0,-1,0,0,0,0],
               [0 ,0 ,0 ,0,1 ,0 ,0,0,0,0,0,0,1,0,0,0],
               [0 ,0 ,0 ,0,0 ,1 ,0,0,0,0,0,0,0,-1,0,0],
               [0 ,0 ,0 ,0,0,0 ,1,0,0,0,0,0,0,0,1,0],
               [0 ,0 ,0 ,0,0 ,0,0,1,0,0,0,0,0,0,0,-1],
               [-1,0 ,0 ,0,0 ,0 ,0,0,1,0,0,0,0,0,0,0],
               [0 ,1 ,0 ,0,0 ,0 ,0,0,0,1,0,0,0,0,0,0],
               [0 ,0 ,-1,0,0 ,0 ,0,0,0,0,1,0,0,0,0,0],
               [0 ,0 ,0 ,1,0 ,0 ,0,0,0,0,0,1,0,0,0,0],
               [0 ,0 ,0 ,0,-1 ,0 ,0,0,0,0,0,0,1,0,0,0],
               [0 ,0 ,0 ,0,0 ,1 ,0,0,0,0,0,0,0,1,0,0],
               [0 ,0 ,0 , 0,0 ,0 ,-1,0,0,0,0,0,0,0,1,0],
               [0 ,0 ,0 ,0 ,0 ,0 ,0 ,1,0,0,0,0,0,0,0,1],
               ])
AncillaUnitary = BS2/sp.sqrt(2)



# We reewrite the classes found in Apendix A4
class10=((anc_in(0)*anc_in(0)-anc_in(1)*anc_in(1)+ anc_in(4)*anc_in(4) - anc_in
    (5)*anc_in(5)
```

```
85          -anc_in(2)*anc_in(2)+anc_in(3)*anc_in(3)- anc_in(6)*anc_in(6)+anc_in(7)*
    anc_in(7))/4
86          )
87 class11=(anc_in(0)*anc_in(0)-anc_in(1)*anc_in(1)-anc_in(4)*anc_in(4) + anc_in(5)
    *anc_in(5)
88          -anc_in(2)*anc_in(2)+anc_in(3)*anc_in(3)+ anc_in(6)*anc_in(6)-anc_in(7)*
    anc_in(7))/4
89 class12=(anc_in(0)*anc_in(0)+anc_in(1)*anc_in(1)-anc_in(4)*anc_in(4) -anc_in(5)*
    anc_in(5)
90     -anc_in(2)*anc_in(2)-anc_in(3)*anc_in(3)+ anc_in(6)*anc_in(6)+anc_in(7)*
    anc_in(7))/4
91 class13=(anc_in(0)*anc_in(0)+anc_in(1)*anc_in(1)+anc_in(4)*anc_in(4) +anc_in(5)*
    anc_in(5)
92     -anc_in(2)*anc_in(2)-anc_in(3)*anc_in(3)- anc_in(6)*anc_in(6)-anc_in(7)*
    anc_in(7))/4
93 #-----------------------------------------------------------------
94 class20 = (-anc_in(0)*anc_in(1)+anc_in(4)*anc_in(5)+anc_in(2)*anc_in(3)
95         - anc_in(6)*anc_in(7))/2
96 class21 = (-anc_in(0)*anc_in(1)-anc_in(4)*anc_in(5)+anc_in(2)*anc_in(3)
97         +anc_in(6)*anc_in(7))/2
98 #-----------------------------------------------------------------
99 class30 = (anc_in(0)*anc_in(3)-anc_in(1)*anc_in(2)+anc_in(4)*anc_in(7)
100            - anc_in(5)*anc_in(6))/2
101 class31 = (anc_in(0)*anc_in(3)-anc_in(1)*anc_in(2)-anc_in(4)*anc_in(7)
102            + anc_in(5)*anc_in(6))/2
103 #-----------------------------------------------------------------
104 class40 = (anc_in(0)*anc_in(6)-anc_in(1)*anc_in(7)-anc_in(4)*anc_in(2)
105            +anc_in(5)*anc_in(3))/2
106 class41 = (anc_in(0)*anc_in(6)+anc_in(1)*anc_in(7)-anc_in(4)*anc_in(2)
107            - anc_in(5)*anc_in(3))/2
108 #-----------------------------------------------------------------
109 class50 = (anc_in(0)*anc_in(4)-anc_in(1)*anc_in(5)-anc_in(2)*anc_in(6)+ anc_in
    (3)*anc_in(7))/2
110 class51 = (anc_in(0)*anc_in(4)+anc_in(1)*anc_in(5)-anc_in(2)*anc_in(6)- anc_in
    (3)*anc_in(7))/2
111 #-----------------------------------------------------------------
112 class60 = (anc_in(0)*anc_in(7)-anc_in(1)*anc_in(6)+anc_in(4)*anc_in(3)- anc_in
    (5)*anc_in(2))/2
113 class61 =(-anc_in(0)*anc_in(7)-anc_in(1)*anc_in(6)+anc_in(4)*anc_in(3)+anc_in(5)
    *anc_in(2))/2
114
115 #-----------------------------------------------------------------
116 class70 =(anc_in(0)*anc_in(5)-anc_in(1)*anc_in(4)+anc_in(2)*anc_in(7)- anc_in(3)
    *anc_in(6))/2
117 class71 =(-anc_in(0)*anc_in(5)-anc_in(1)*anc_in(4)+anc_in(2)*anc_in(7)+ anc_in
    (3)*anc_in(6))/2
118
119 # DIFFERENT TYPES OF ANCILLA STATES THAT WE TRIED
120
121 anc2Plus= (anc_in(8)*anc_in(9)+anc_in(12)*anc_in(13)+anc_in(10)*anc_in(11)
122     + anc_in(14)*anc_in(15))/2
123 anc20= (-anc_in(8)*anc_in(9)+anc_in(12)*anc_in(13)+anc_in(10)*anc_in(11)
124     - anc_in(14)*anc_in(15))/2
```

```
anc21= (-anc_in(8)*anc_in(9)-anc_in(12)*anc_in(13)+anc_in(10)*anc_in(11)
    +anc_in(14)*anc_in(15))/2
anc21minus= (-anc_in(8)*anc_in(9)+anc_in(12)*anc_in(13)-anc_in(10)*anc_in(11)
    +anc_in(14)*anc_in(15))/2

anc1Plus= (anc_in(8)*anc_in(8)+anc_in(9)*anc_in(9)+anc_in(10)*anc_in(10)
    + anc_in(11)*anc_in(11))/2
anc3Plus=(anc_in(8)*anc_in(11)+anc_in(9)*anc_in(10)+anc_in(12)*anc_in(15)
            +anc_in(13)*anc_in(14))/2
anc4Plus=(anc_in(8)*anc_in(14)-anc_in(9)*anc_in(15)-anc_in(12)*anc_in(10)
            +anc_in(13)*anc_in(11))/10
anc5Plus=(anc_in(8)*anc_in(12)-anc_in(9)*anc_in(13)-anc_in(10)*anc_in(14)+
    anc_in(11)*anc_in(15))/2
anc6Plus=(anc_in(8)*anc_in(15)-anc_in(9)*anc_in(14)+anc_in(12)*anc_in(11)-
    anc_in(13)*anc_in(10))/2
anc7Plus=(anc_in(8)*anc_in(13)-anc_in(9)*anc_in(12)+anc_in(10)*anc_in(15)-
    anc_in(11)*anc_in(14))/2
```